

AARS JOURNAL

A PUBLICATION OF THE AMERICAN ROCKET SOCIETY

VOLUME 30 NUMBER 1

JANUARY 1960

LOS ANGELES PUBLIC LIBRARY

FEB 2 - 1960

BIND

SURVEY ARTICLE

- Review of Design Information on Buckling of Unstiffened Thin Walled Circular Cylindrical Shells Bertram Klein 7

INVITED ARTICLES

- Orbits of Cosmic Rockets Toward the Moon L. I. Sedov 14
- Some Problems of Providing for Scientific Research on Rockets A. A. Blagomravov 22
- Results of Scientific Investigations Made by Soviet Sputniks and Cosmic Rockets V. I. Krasovskii 27

CONTRIBUTED ARTICLES

- Structural Considerations of Manned Space Vehicles Anthony P. Coppa 34
- Midcourse Guidance Problem in Satellite Interception—I Angelo J. Skafuris and Donald H. Schiller 41
- Missile Orientation Errors in Command Guidance Systems Kenneth C. Mathews 46
- An Approximation to the Re-Entry Trajectory Mildred M. Moe 50
- Use of Energy Storage in Low Thrust Spaceflight Morton Carnac 54

TECHNICAL NOTES

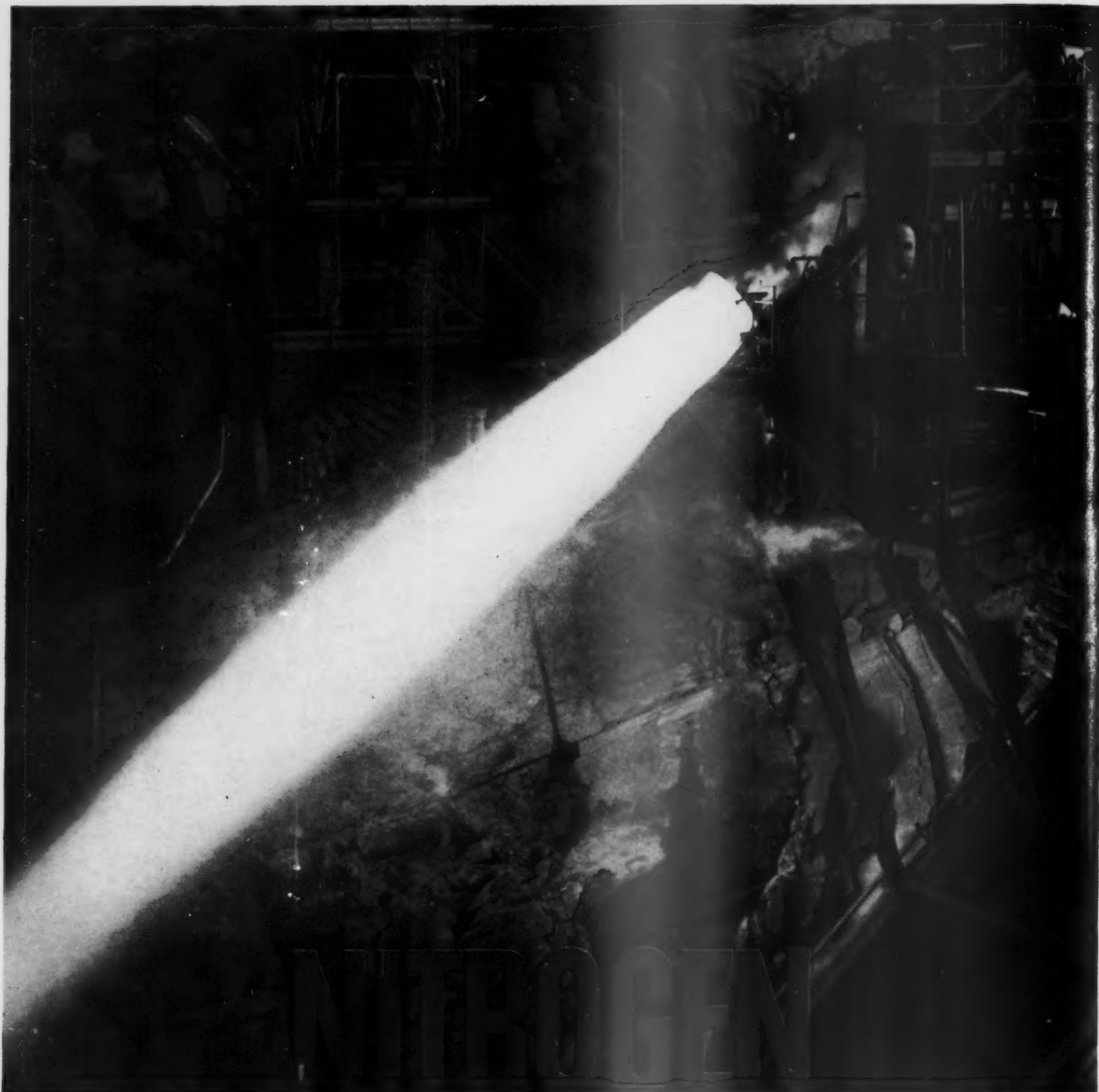
- Composition of Reaction Mixtures Flowing Through Rocket Nozzles B. P. Sengupta and T. F. Phadya 63
- Effects of Diffusion and Chemical Reaction on Convective Heat Transfer Daniel E. Roemer 114
- Uncertainty in a Calculated Specific Impulse Due to an Uncertainty in the Heat of Formation of the Propellant L. J. Gordon 118
- Transient and Steady-State Behavior of an Idealized Solar Powered Heat Exchanger J. W. Tatum 119
- Steady-State Behavior of Extended Surfaces in Space J. W. Tatum 125
- Analytical Estimates for Optimum Transfer Paths H. Munck and R. McGinn 130
- Projected Orbits of 24-hr Earth Satellites Louis B. Wedel 123
- Satellite Librations of Large Amplitude W. B. Klemperer 123
- Librations on a Slightly Eccentric Orbit Robert M. L. Baker Jr. 124
- Planar Libration of a Prolate Spheroidal Shell Robert M. L. Baker Jr. 125
- Effect of Thrust Misalignment on Opto-Stabilized Vehicles Russell P. Nagasaki 125

DEPARTMENTS

- Technical Comments 130
- New Patents 134
- Book Reviews 135
- Technical Literature Digest 136

RUSSIAN SUPPLEMENT 65-112

MAR 20 1961



NITROGEN TETROXIDE

Tests at Allied Chemical show Nitrogen Tetroxide ready for instant use even after 9 years of storage. Combustion tests with important liquid fuels and Nitrogen Tetroxide indicated up to 99% theoretical combustion efficiency. Additional advantages offered by N_2O_4 are listed at right.

We'll gladly supply technical literature which includes a 59-page Product Bulletin, a brochure entitled "Large Scale Handling of Nitrogen Tetroxide", and "Nitrogen Tetroxide as an Oxidizer in Rocket Propulsion". And, of course, Allied Chemical technical service is always available to users of N_2O_4 .

**instantly ready oxidizer
develops up to 99% theoretical Isp!**

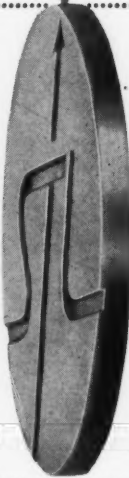
BASIC TO
AMERICA'S
PROGRESS



NITROGEN DIVISION
Dept. NT7-12-1, 40 Rector Street, New York 6, N. Y.

- Requires no super-refrigeration — can be stored indefinitely in missile at launching site.
- Hypergolic with amine-type fuels — ignition is simple and reliable.
- Can be used with most fuels — including those containing carbon.
- Eliminates rough starts—which are due to accumulation of unreacted propellants in thrust chamber.
- Motors are throttleable—when N_2O_4 is used as the oxidizer.
- Immediate availability—Allied Chemical Nitrogen Tetroxide is shipped in 125- and 150-lb. steel cylinders, 1-ton containers, 30- and 50-ton tank cars.

SCIENTISTS AND ENGINEERS: There are two sides to the STL coin...



What STL does:

Space Technology Laboratories is making significant contributions in theoretical analysis, research, development and technical management of advanced ballistic missile and space systems. STL conducts advanced space flight experiments under the executive management of the Air Force on behalf of such agencies as ARPA and NASA. In addition STL's leadership in military applications of space technology is illustrated by its successful accomplishments as the contractor responsible for over-all systems engineering and technical direction of the Atlas, Titan, Thor, and Minuteman portions of the Air Force Ballistic Missile Program.



What STL offers:

For scientists and engineers with outstanding capabilities, STL offers unusual growth opportunities in many areas of technical activity, including:

- Electronic and Electromechanical Systems
- Vehicle Engineering and Development
- Propulsion and Guidance Systems
- Computer Technology
- Systems Engineering and Technical Direction
- Telecommunications
- Airborne Systems
- Ground Support Equipment

The Technical Staff of STL is the largest professional group in the nation devoted exclusively to research, development, and systems engineering in the field of ballistic missiles, space projects, and related advanced technology. If you want to apply your skills and talents, in these advanced areas working with leaders in your field, investigate positions at STL now. Please send your resume today to Mr. Richard A. Holliday.

*Space Technology Laboratories, Inc., P. O. Box 95004
Los Angeles 45, California*



SPACE TECHNOLOGY LABORATORIES, INC.

ARS JOURNAL

A PUBLICATION OF THE AMERICAN ROCKET SOCIETY

EDITOR Martin Summerfield
ASSOCIATE TECHNICAL EDITOR Irvin Glassman
MANAGING EDITOR Barbara Nowak
ASSISTANT EDITOR Julie Hight
ART EDITOR John Culin

ASSOCIATE EDITORS

J. George Adashko, *Russian Supplement*; Ali Bulent Cambel, *Northwestern University, Book Reviews*; Charles J. Mundo Jr., *American Bosch Arma Corporation, Guidance*; M. H. Smith, *Princeton University, Technical Literature Digest*

CONTRIBUTOR

George F. McLaughlin

ADVERTISING AND PROMOTION MANAGER

William Chenoweth

ADVERTISING PRODUCTION MANAGER

Walter Brunke

ADVERTISING REPRESENTATIVES

New York
D. C. Emery and Associates
400 Madison Ave., New York, N. Y.
Telephone: Plaza 9-7460

Chicago
Jim Summers and Associates
35 E. Wacker Dr., Chicago, Ill.
Telephone: Andover 3-1154

Boston
Robert G. Melendy
17 Maugus Ave., Wellesley Hills, Mass.
Telephone: Cedar 5-6503

Los Angeles
James C. Galloway and Co.
6535 Wilshire Blvd., Los Angeles, Calif.
Telephone: Olive 3-3223

Detroit
R. F. Pickrell and Vincent Purcell
318 Stephenson Bldg., Detroit, Mich.
Telephone: Trinity 1-0790

Pittsburgh
John W. Foster
239 4th Ave., Pittsburgh, Pa.
Telephone: Atlantic 1-2977

American Rocket Society

500 Fifth Avenue, New York 36, N. Y.

Founded 1930

OFFICERS

President
Vice-President
Executive Secretary
Treasurer
Secretary and Asst. Treasurer
General Counsel
Director of Publications

Howard S. Seifert
Harold W. Ritchey
James J. Harford
Robert M. Lawrence
A. C. Slade
Andrew G. Haley
Irwin Hersey

BOARD OF DIRECTORS

Terms expiring on dates indicated

Ali B. Cambel 1962
Richard B. Canright 1962
James R. Dempsey 1961
Herbert Friedman 1962
Robert A. Gross 1962
Samuel K. Hoffman 1960
A. K. Oppenheim 1961

William H. Pickering 1961
Simon Ramo 1960
William L. Rogers 1960
David G. Simons 1961
John L. Sloop 1961
Martin Summerfield 1962
Wernher von Braun 1960

Maurice J. Zucrow 1960

TECHNICAL COMMITTEE CHAIRMEN

Lawrence S. Brown, Guidance and Navigation
Milton U. Clauser, Magnetohydrodynamics
William H. Dorrance, Hypersonics
Herbert Friedman, Instrumentation
George Gerard, Structures and Materials
Milton Greenberg, Physics of the Atmosphere and Space
Stanley V. Gunn, Nuclear Propulsion
Andrew G. Haley, Space Law and Sociology
Samuel Herrick, Astrodynamics
Maxwell W. Hunter, Missiles and Space Vehicles
Herbert L. Karsch, Logistics and Operations

David B. Langmuir, Ion and Plasma Propulsion
Y. C. Lee, Liquid Rockets
Max Lowy, Communications
Paul E. Sandorff, Education
Richard A. Schmidt, Test Facilities and Support Equipment
William B. Shippen, Ramjets
John L. Sloop, Propellants and Combustion
Ivan E. Tuhy, Solid Rockets
Stanley C. White, Human Factors and Bio-Astronautics
George F. Wislicenus, Underwater Propulsion
Abe M. Zarem, Power Systems

Scope of ARS JOURNAL

This Journal is devoted to the advancement of astronautics through the dissemination of original papers disclosing new scientific knowledge and basic applications of such knowledge. The sciences of astronautics are understood here to embrace selected aspects of jet and rocket propulsion, spaceflight mechanics, high speed aerodynamics, flight guidance, space communications, atmospheric and outer space physics, materials and structures, human engineering, overall system analysis, and possibly certain other scientific areas. The selection of papers to be printed will be governed by the pertinence of the topic to the field of astronautics, by the current or probable future significance of the research, and by the importance of distributing the information to the members of the Society and to the profession at large.

Information for Authors

Manuscripts must be as brief as the proper presentation of the ideas will allow. Exclusion of dispensable material and conciseness of expression will influence the Editors' acceptance of a manuscript. In terms of standard-size double-spaced typed pages, a typical maximum length is 22 pages of text (including equations), 1 page of references, 1 page of abstract and 12 illustrations. Fewer illustrations permit more text, and vice versa. Greater length will be acceptable only in exceptional cases.

Short manuscripts, not more than one quarter of the maximum length stated for full articles, may qualify for publication as Technical Notes or Technical Comments. They may be devoted to new developments requiring prompt disclosure or to comments on previously published papers. Such manuscripts are published within a few months of the date of receipt.

Sponsored manuscripts are published occasionally as an ARS service to the industry. A manuscript that does not qualify for publication, according to the above-stated requirements as to subject, scope or length, but which nevertheless deserves widespread distribution among jet propulsion engineers, may be printed as an extra part of the Journal or as a special supplement, if the author or his sponsor will reimburse the Society for actual publication costs. Estimates are available on request. Acknowledgment of such financial sponsorship appears as a footnote on the first page of the article. Publication is prompt since such papers are not in the ordinary backlog.

Manuscripts must be double spaced on one side of paper only with wide margins to allow for instructions to printer. Include a 100 to 200 word abstract. State the authors' positions and affiliations in a footnote on the first page. Equations and symbols may be handwritten or typewritten; clarity for the printer is essential. Greek letters and unusual symbols should be identified in the margin. If handwritten, distinguish between capital and lower case letters, and indicate subscripts and superscripts. References are to be grouped at the end of the manuscript and are to be given as follows. For journal articles: Authors first, then title, journal, volume, year, page numbers; for books: Authors first, then title, publisher, city, edition and page or chapter numbers. Line drawings must be clear and sharp to make clear engravings. Use black ink on white paper or tracing cloth. Lettering should be large enough to be legible after reduction. Photographs should be glossy prints, not matte or semi-matte. Each illustration must have a legend; legends should be listed in order on a separate sheet.

Manuscripts must be accompanied by written assurance as to security clearance in the event the subject matter lies in a classified area or if the paper originates under government sponsorship. Full responsibility rests with the author.

Preprints of papers presented at ARS meetings are automatically considered for publication.

Submit manuscripts in duplicate (original plus first carbon, with two sets of illustrations) to the Managing Editor, ARS JOURNAL, 500 Fifth Avenue, New York 36, N.Y.

ARS JOURNAL is published monthly by the American Rocket Society, Inc. and the American Interplanetary Society at 20th & Northampton Sts., Easton, Pa., U. S. A. Editorial offices: 500 Fifth Ave., New York 36, N. Y. Price: \$12.50 per year, \$2.00 per single copy. Second-class mail privileges authorized at Easton, Pa. This publication is authorized to be mailed at the special rates of postage prescribed by Section 132.122. Notice of change of address should be sent to the Secretary, ARS, at least 30 days prior to publication. Opinions expressed herein are the authors and do not necessarily reflect the views of the Editors or of the Society. © Copyright 1960 by the American Rocket Society, Inc.

Announces the Publication of

The Dynamics of Conducting Gases

PROCEEDINGS OF THE THIRD BIENNIAL GAS DYNAMICS SYMPOSIUM

Edited by Ali Bulent Cambel, Northwestern University, and John B. Fenn, ONR Project Squid and Co-sponsored by Northwestern University and the American Rocket Society

IN THE FIELD of power production, propulsion and flight, the use of conducting gases, namely plasmas, has become an important central problem. Among the various aspects of interest to engineers and scientists are the properties and the dynamics of plasmas as well as the interaction between the fluid dynamic and the electromagnetic fields.

In the Proceedings of the Third Biennial Gas Dynamics Symposium, 19 papers on the physics of plasmas, magneto gas dynamics, plasma phenomenology and the various engineering applications associated with conducting gases are presented.

THE DYNAMICS OF CONDUCTING GASES will be significant to scientists and engineers in universities, government establishments and industrial laboratories. The theories proposed, the experimental techniques outlined and the applications which are proposed should be of interest to persons in the flight sciences and the power production fields.

7" x 9³/₄", 224 pages, 190 illust., \$12.50

Contents

PART ONE: FUNDAMENTAL PROCESS AND IONIZED GAS PROPERTIES

- W. P. ALLIS and S. J. BUCHSBAUM: *The Conductivity of an Ionized Gas in a Magnetic Field*
 R. A. GROSS and C. L. EISEN: *Some Properties of a Hydrogen Plasma*
 I. PRIGOGINE: *The Statistical Mechanics of the Approach to Equilibrium in Gases*
 RADU BALESCU: *Irreversible Processes in a Plasma: Effect of Long Range Forces*
 H. F. CALCOTE: *Relaxation Processes in Plasma*

PART TWO: THEORETICAL CONSIDERATIONS ON THE INTERACTION OF MAGNETIC FIELDS AND FLOWS OF IONIZED GASES

- W. R. SEARS: *Some Solutions of the Macroscopic Equations of Magnetohydrodynamics*
 RUDOLPH X. MEYER: *Magnetohydrodynamics in the Limit of Small Inertial Forces*
 F. D. HAINS, YUSUF A. YOLER and EDWARD EHLERS: *Axially Symmetric Hydromagnetic Channel Flow*

PART THREE: LABORATORY EXPERIENCE WITH THE FLOW OF IONIZED GASES

- WINSTON H. BOSTICK, JOHN NANKIVELL, SAMUEL KOSLOV and GEORGE SCHMIDT: *Experimental Studies on Plasma Dynamics*
 JAMES A. BROWNING: *Techniques for Producing Plasma Jets*
 RICHARD W. ZIEMER: *Electromagnetic Shock Tubes*
 M. CAMAC and G. S. JANES: *Applied Magnetohydrodynamics at Avco-Everett Research Laboratory*

PART FOUR: APPLICATIONS OF MAGNETO GAS DYNAMICS EFFECTS

- JOSEPH L. NEURINGER: *Optimum Power Generation Using a Plasma as the Working Fluid*
 MARK L. GHAI: *Space Propulsion Engines—A Problem in Production of High Velocity Gases*
 ALFRED E. KUNEN and WILLIAM MCILROY: *The Electromagnetic Pinch Effect for Space Propulsion*
 ROBERT V. HESS and KARLHEINZ THOM: *Plasma Acceleration by Guided Microwaves*
 GEORGE P. WOOD and ARLEN F. CARTER: *Considerations in the Design of a Steady DC Plasma Accelerator*
 AEROTHERMOCHEMISTRY, edited by Donald K. Fleming. *Proceedings of the First Biennial Gas Dynamics Symposium. \$5.00*
 TRANSPORT PROPERTIES IN GASES, edited by Ali Bulent Cambel and John B. Fenn. *Proceedings of the Second Biennial Gas Dynamics Symposium. \$7.50*

ORDER FORM

Please send me — copy (copies) of THE DYNAMICS OF CONDUCTING GASES (\$12.50 list price)

NAME _____

ADDRESS _____

CITY _____ ZONE _____ STATE _____

Payment encl. ☐ Please bill ☐

NORTHWESTERN UNIVERSITY PRESS
 1840 Sheridan Road, Evanston, Ill.

1840 Sheridan Road

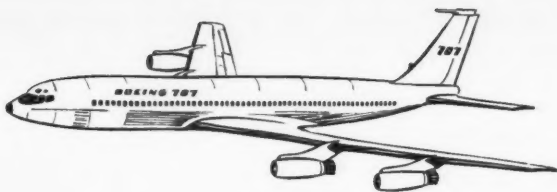
Evanston, Illinois



**Largest closed-die
forging ever made
for
commercial
aircraft**

The forging of these 657 lb. bulkheads presented unusual problems—problems of die design, of forging, and of handling. The successful solution of these problems saved a costly assembly of many smaller parts—costly both in terms of dollars and pounds.

This is a typical Wyman-Gordon accomplishment—the result of over seventy-five years of forging experience, and today supported by the greatest range of heavy forging equipment and technical know-how in the industry.



Over 1000 Wyman-Gordon forgings pace advanced jet designs

In saluting the great achievement of America's commercial jet leadership, Wyman-Gordon takes great pride in having participated so extensively in the development of the aircraft industry from its very beginning.

In World War I, the use of forgings was confined to engine parts and Wyman-Gordon made most of

them. Today, from the huge main bulkhead forging at the left to the engine parts below, Wyman-Gordon forgings are in the wings, fuselage, landing gear and engines of the four newest commercial jet aircraft. These and a great variety of other vital components are forged from many types of materials: aluminum, magnesium, titanium, steel, as well as many new uncommon alloys.



FORGED



EST. 1883

In the highly stressed parts of modern aircraft, there is no substitute for forgings and in complicated forgings of difficult alloys, there is no substitute for Wyman-Gordon quality and experience. We are prepared to serve you at the design, engineering and purchasing stages of your developments.

WYMAN - GORDON FORGINGS

of Aluminum Magnesium Steel Titanium . . . and Beryllium Molybdenum Columbium and other uncommon materials

HARVEY ILLINOIS

WORCESTER MASSACHUSETTS

DETROIT MICHIGAN

GRAFTON MASSACHUSETTS

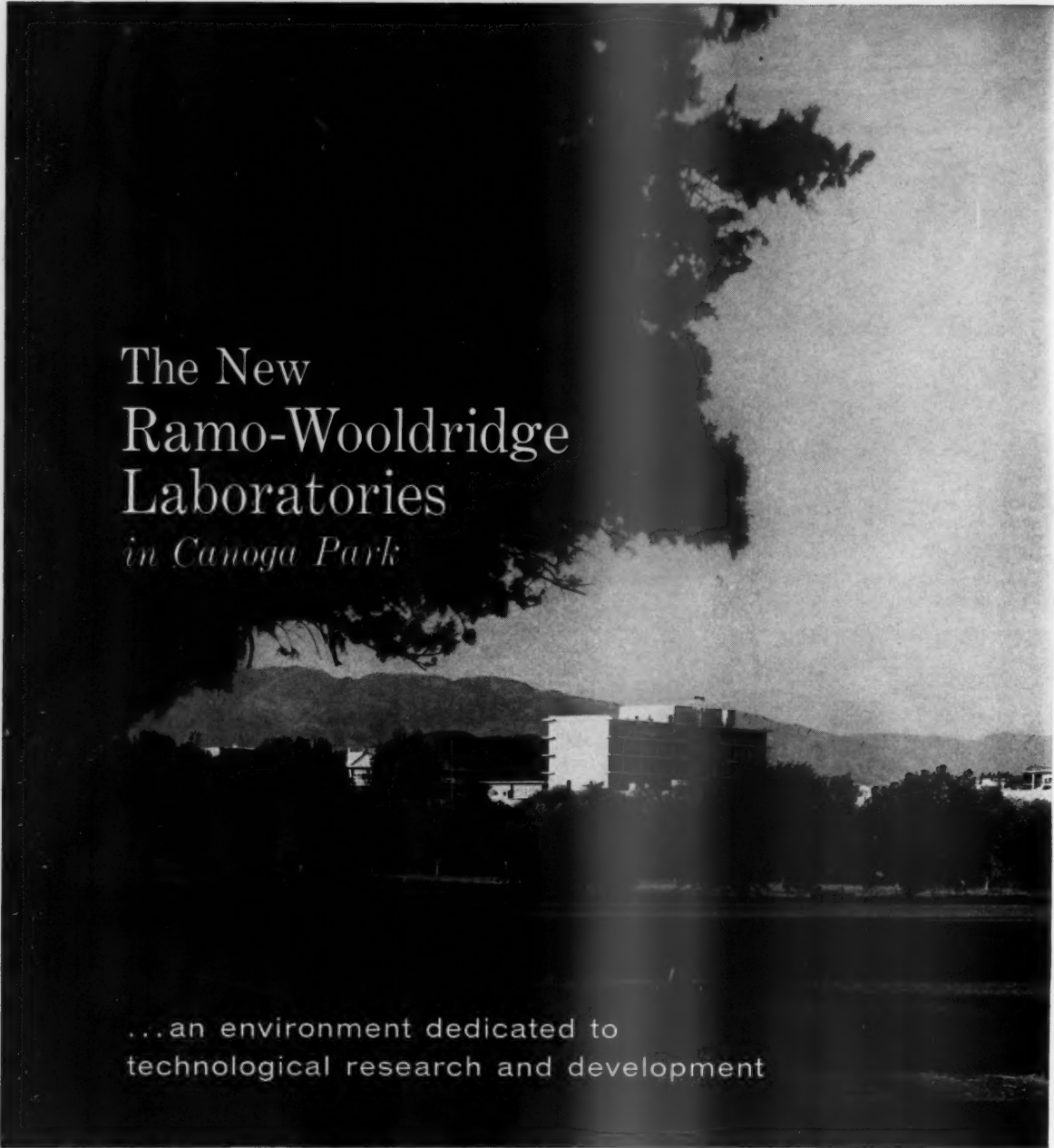
FRANKLIN PARK ILLINOIS

LOS ANGELES CALIFORNIA

FORT WORTH TEXAS

JANUARY 1960

5



The New Ramo-Wooldridge Laboratories *in Canoga Park*

...an environment dedicated to
technological research and development

The new Ramo-Wooldridge Laboratories in Canoga Park, California, will provide an excellent environment for scientists and engineers engaged in technological research and development. Because of the high degree of scientific and engineering effort involved in Ramo-Wooldridge programs, technically trained people are assigned a more dominant role in the management of the organization than is customary.

The ninety-acre landscaped site, with modern buildings grouped around a central mall, contributes to the

academic environment necessary for creative work. The new Laboratories will be the West Coast headquarters of Thompson Ramo Wooldridge Inc. as well as house the Ramo-Wooldridge division of TRW.

The Ramo-Wooldridge Laboratories are engaged in the broad fields of electronic systems technology, computers, and data processing. Outstanding opportunities exist for scientists and engineers.

For specific information on current openings write to Mr. D. L. Pyke.



THE RAMO-WOOLDRIDGE LABORATORIES

8433 FALLBROOK AVENUE, CANOGA PARK, CALIFORNIA

Review of Design Information on Buckling of Unstiffened Thin Walled Circular Cylindrical Shells

BERTRAM KLEIN

Solar Aircraft Co.
San Diego, Calif.

The author is presently Chief of Structures, Solar Aircraft Co., and is the author of more than 50 technical papers. He received the B.A.E. and B.M.E. degrees from the Polytechnic Institute of Brooklyn. From 1943 to 1947 he worked for NACA and since then has held various positions in the field of structures at Bell Aircraft Co., Douglas Aircraft Co., North American Aviation, Inc., and the National Rocket Co. In 1947-1950 he was Assistant Professor at Purdue University, and from 1950 to 1952 he taught at the graduate school, University of Buffalo. More recently, he was employed as a design specialist in structures at Convair Astronautics.

THIN skin missile tanks stiffened by internal pressure still may fail by local buckling if the loads are high enough or the pressure is not high enough. (A cylinder is considered to have failed by buckling when it is in such a state that the cylinder cannot sustain additional compressive stresses.) Unpressurized thin walled cylinders definitely may be designed by buckling. Sometimes such structures are missile structures. In the latter instance reliable data are mandatory in design. Much attention has been given in the literature to the problems of the buckling of unstiffened circular cylindrical shells under various loading conditions (1-52).¹ However, to date, reliable and simple design curves still are not available. Therefore, a careful objective review of the known theories and test data has been undertaken. The purpose of the present paper is to present the results of the investigation in forms which are considered reliable and simple. Also, areas are pointed out in which there is a need for further test data.

Pure Compression

The greatest concentration of effort has been for this loading condition. The reasons for this emphasis, paradoxically enough, are the relative simplicity of testing for this type of loading and the accompanying need for explanation of the wide variance of the test results. Actually before the development of missile structures, the primary loading on airplane monocoques was bending. The literature contains ample discussion of lack of agreement of theory and test for cylinders in compression. The problem is nonlinear with the strength of the structure strongly dependent on eccentricities of the structure. The problem therefore must be treated on an empirical and statistical basis.

The final curves recommended for design must be of a high degree of reliability, yet not overly conservative. It has been argued that certain test data should not be used to establish design curves. For example, Donnell's test specimens were manufactured from shim stock materials and were of small diameter. However, other investigators also used small gages. Yet Donnell's tubes were the smallest in diameter. Furthermore, Newmark tested large thick fabricated

cylinders. His test data fall in about the same region as Donnell's or even lower. The edge condition of Newmark's cylinders apparently was not a fixed edge condition. The conclusion that may be drawn here is that size or gage of a specimen in itself is not indicative of the reliability of the test data. One can build a bad large cylinder or perform a bad test on a large cylinder just as easily as on a small one. The question to be answered then is what tests should be considered in arriving at design curves. Since, in actual practice, conditions may not be as ideal as in the test laboratory, one should use all representative test data. Machined cylinders should not be considered because many actual cylinders are made up of spliced sheets. Cylinders tested to date had longitudinal splices. In the future it may be of advantage to test large cylinders, such as occur in missile structures.

Another matter influencing the buckling of axially compressed cylinders is the uniformity of the axial state of stress around the circumference of the cylinder. The closer this state of stress is to a uniform state of stress, the higher the buckling load. It is of interest to note that the higher values of buckling stresses were obtained by investigators who used a central means of load application, i.e., a ball and socket set-up or a central strut. On the other hand, the test data obtained by use of plate-distributed loading are the lowest values in the test scatter.

According to (22), a cylinder in axial compression may be considered long if a certain parameter Z is greater than 80. Thus for $R/t > 100$ and $L/R > 1$, the buckling stress would be independent of L/R . However, a correct interpretation of the test data reveals this conclusion is not correct. Where large deflection effects are important, eccentricities are important because the structure is more apt to jump from one state to another. The longer the cylinder is the greater the chance for out-of-roundness. Consequently, the parameter L/R must be considered throughout the entire range of values of R/t . This effect is illustrated indirectly in Fig. 1a (20). Notice that the slope of the best fit curve is less than the 45-deg slope of the theoretical lines. This fact means that the buckling stress decreases with increasing length. More test data are needed for R/t larger than 2000 to confirm this trend. Some test data taken from (22) are shown in Table 1. All cylinders are so-called long cylinders ($Z > 80$). Notice the drop in allowable stress with increasing length.

Presented at the ARS 13th Annual Meeting, New York, N. Y., Nov. 17-21, 1958.

¹ Numbers in parentheses indicate References at end of paper.

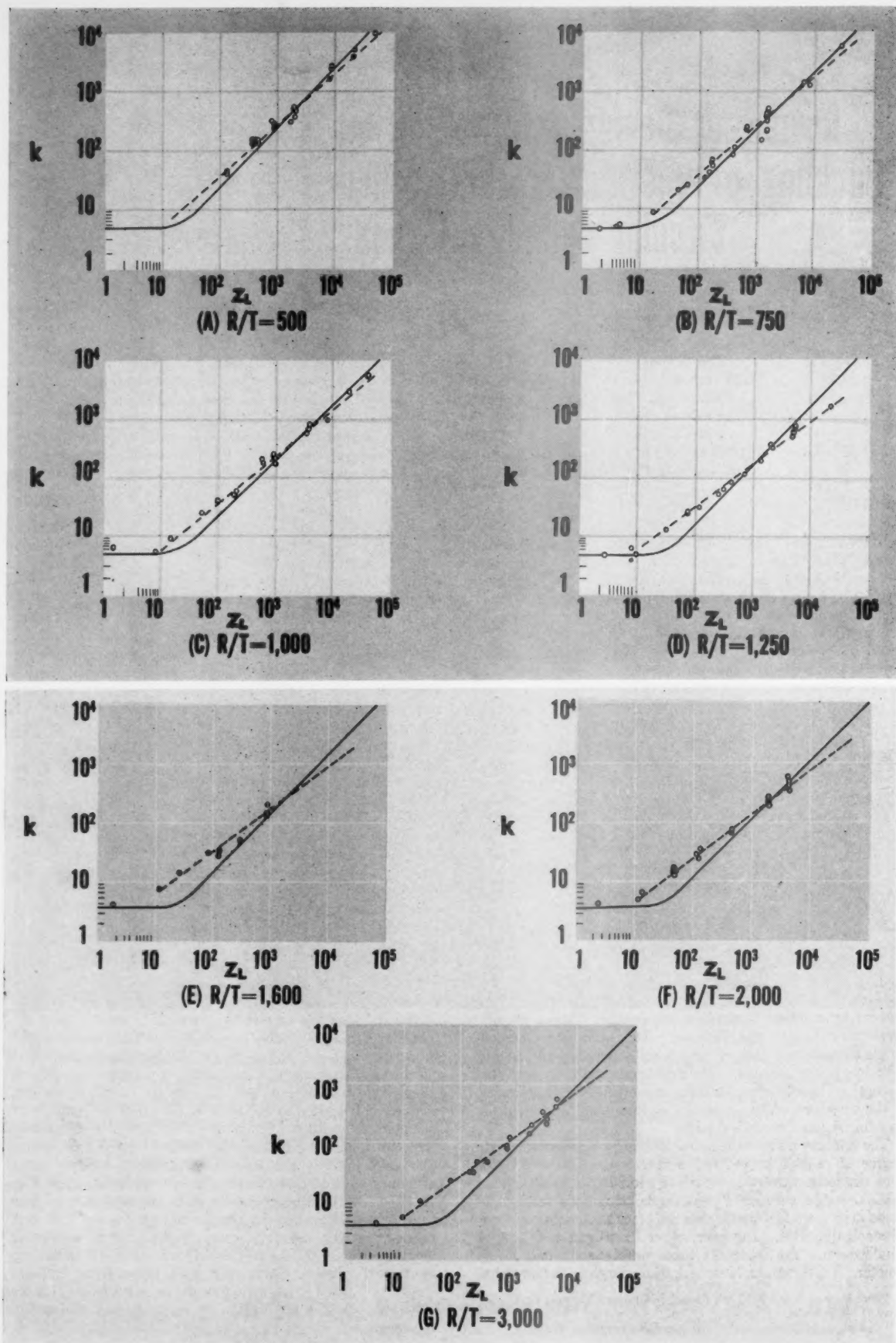


Fig. 1a Buckling test data and corresponding empirical curve for clamped axially compressed circular cylinders

Table 1 Effect of length on the buckling of cylinders in axial compression, $R = 8.75$

Specimen no.	L	R/t	σ_{cr}
25(1)	9.5	2734	1739
29(1)	9.5	2734	1648
4(1)	21.5	2734	1176
4(2)	21.5	2734	1148
7(1)	21.5	2734	1097
7(2)	21.5	2734	1119
58(1)	21.5	2734	1250
67(1)	21.5	2734	1222

Based on the previous discussions, the curves presented in Fig. 1b are recommended for design. Most of the test data are for cylinders with clamped edges. The curves should be applicable for buckling of simply supported cylinders except perhaps in the upper left-hand region. The allowable buckling stresses for long cylinders with large R/t are found to be less than those previously recommended for design. The curves shown in Fig. 1b are believed to be of high reliability—at least 90 per cent reliable. However, they are not based on a comprehensive statistical analysis because there are not enough data available to cover adequately the entire range of values of R/t and L/R .

Pure Bending

The test data for pure bending buckling of cylinders are less abundant than those for pure compression for reasons explained previously. The maximum bending buckling stress $M/\pi R^2 t$ exceeds the compressive buckling stress of a given cylinder. The theoretical reason for the increase is the fact that the compressive stress is not constant. Superimposed on this basic phenomenon is the effect of imperfections which again causes a wide variance in the test data. One might expect the test scatter to be less than in pure compression tests since the region of maximum compression is confined to a small portion of the cylinder cross section, thereby lessening the chance of imperfections precipitating buckling. However, there is another phenomenon connected with the bending of a cylinder which does not occur in compression tests. This effect is flattening or ovalation which is tantamount to eccentricity. The weakening effect of length discussed for the compression allowables also should be present for bending buckling for the reasons given previously.

A suggested overall factor of 1.3 has been given for the ratio of the pure bending buckling stress to the pure compression buckling stress. According to the results of the limited test data, this factor may be all right for certain ranges of values of R/t and L/R . However, for large R/t the factor may actually approach unity. More tests are needed in this region, as well as for long cylinders with smaller values of R/t . Some values of pure bending buckling allowables may be found from Fig. 5 by setting the pressure equal to zero.

Pure Torsion

The amount of test data for this case is plentiful. The status of this loading condition is better than that for pure compression or pure bending as far as agreement between theory and test is concerned. The buckling behavior of the structure is less nonlinear and less sensitive to imperfections, although these effects are still present. The curves proposed for design are shown in Fig. 2. Notice the similarity between the shapes of these curves and the ones for pure compression shown in Fig. 1. The curves in Fig. 2 are of a high degree of

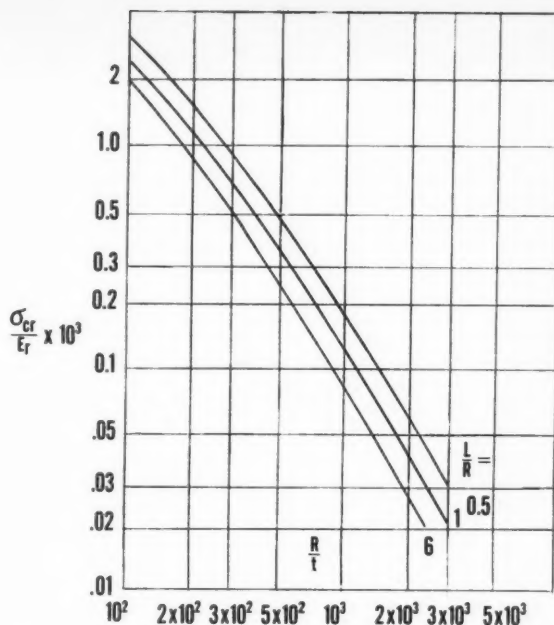


Fig. 1b Compression buckling stress for unpressurized cylinders with clamped edges

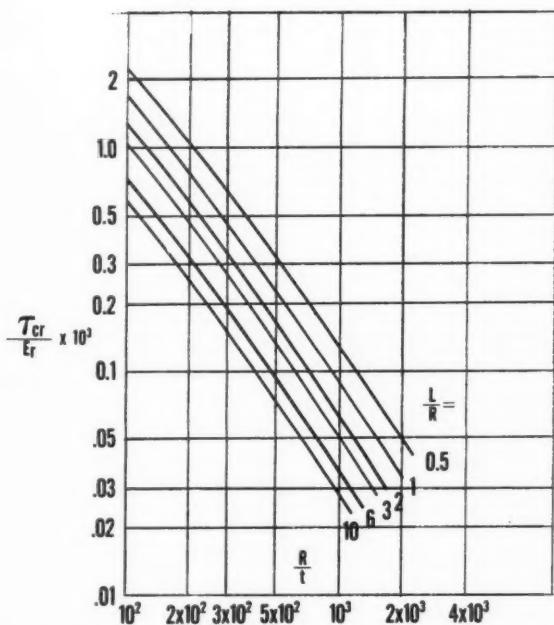


Fig. 2 Torsion buckling stress for unpressurized cylinders with simply supported edges

reliability. Strictly, these curves are supposed to be valid for cylinders with simply supported edges. However, they may be used for cylinders with clamped edges, except perhaps in their upper left-hand regions. Actually the test data are based on specimens whose ends were clamped, or close to being clamped.

External (Negative) Hydrostatic Pressure

There are enough test data for this loading condition to draw design curves. Effects of eccentricities and nonlinear action are confined to so-called short cylinders (having low values of Z). The high reliability design curves are given in Fig. 3. These curves are for simply supported cylinders. For cylinders with fully clamped edges, it is suggested that the curves be used with the effective length of the cylinder reduced to 0.83 times the actual length. The curves in Fig. 3 may also be used for cylinders subjected to radial pressure, except perhaps in their upper left-hand regions.

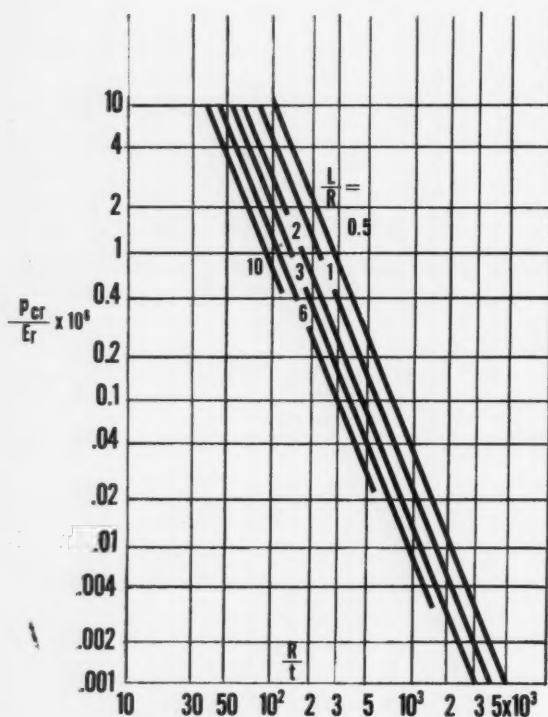


Fig. 3 Hydrostatic buckling pressure for cylinders with simply supported edges

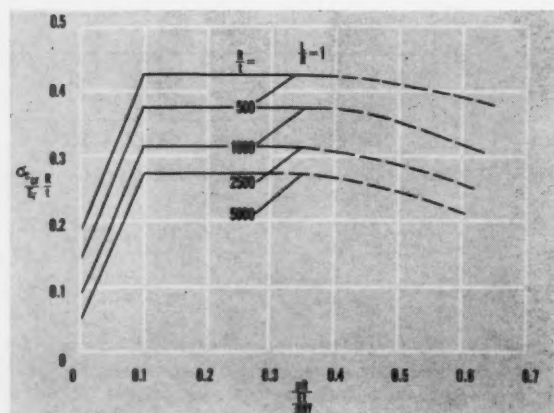


Fig. 4a Compressive buckling stress as a function of pressure hoop strain, $L/R = 1$

Inelastic Behavior

Each of Figs. 1 to 3 contains a reduced modulus E , needed to account for inelastic behavior of the material when the buckling stress exceeds the proportional limit. Apparently Bijlaard was one of the first to derive these quantities. Krivetsky (5) plotted these results in certain diagrams to facilitate their use. More recently (9, 17) Gerard has developed expressions for plasticity reduction. Lee and Ades investigated the reduced modulus for plastic torsion buckling. Needham has suggested a value of $\sqrt{E_t E}$ for the case of axially compressed cylinders (27). This factor is the so-called von Kármán reduced modulus.

Donnell and Wan have related the onset of plasticity in an axially compressed cylinder to the severity of the imperfections existing in the cylinder. For purposes of design, it is believed simpler to present the design curves as shown here—including the effects of imperfections only indirectly and using a reduced modulus to account for inelastic behavior.

Combined Compression and Internal Pressure

This loading condition is important in missile design. Theoretically, one would expect that if the pressure is made high enough the buckling stress could be made equal to the classical value of $0.605 E_t/R$, since the internal pressure smooths the surface of the cylinder, thereby canceling the effects of imperfections. However, in actual practice the test data exhibit scatter with reliable values of lower magnitude. The eccentricities which precipitate buckling of unpressurized cylinders again are present.

It is interesting to see what happens to the buckling load as we increase the value of the internal pressure. At first there is a steady sharp rise in the buckling stress. Then when some value of pressure is reached, the buckling stress no longer increases but remains approximately constant. Thereafter an actual decrease in allowable buckling stress takes place as we increase pressure. This latter behavior may be explained as follows. It is known that eccentricity is detrimental in the compressive buckling of cylinders. When pressure is high, the structure actually has a built-in eccentricity due to the bulging of the cylinder. This action is prevented at the supports. Eventually, as one approaches the yield strain of the material in the hoop direction the compressive strength of the cylinder should drop rapidly. The structure then behaves like an anisotropic shell. For these reasons it is believed that one should use the strain parameter $(pR/E_t)/\epsilon_{hy}$ in plotting the design curves. Here ϵ_{hy} is the tensile yield strain of the material in the hoop direction.

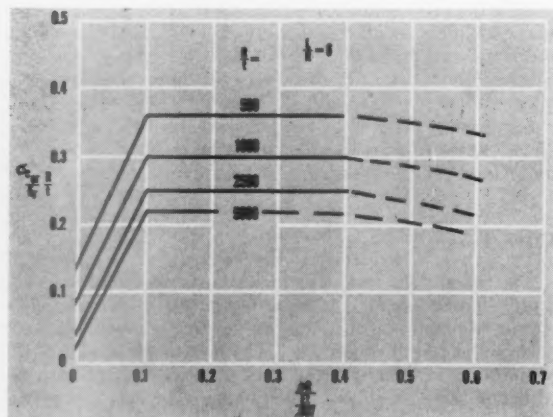


Fig. 4b Compressive buckling stress as a function of pressure hoop strain, $L/R = 6$

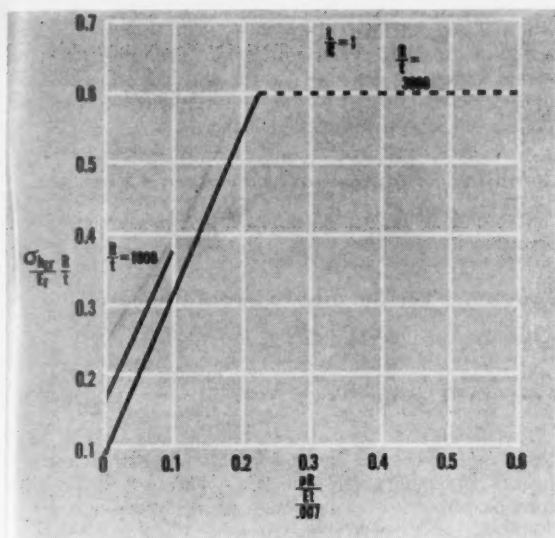


Fig. 5 Bending buckling stress as a function of pressure hoop strain, $L/R = 1$

Some investigators have used the increase in the buckling stress coefficient over the unpressurized one as the ordinate in plotting the design curves. It is not considered of advantage to plot this change in buckling coefficient as ordinate. A more realistic and direct picture is obtained if one uses the actual buckling coefficient. In this way a family of curves is obtained as shown in Figs. 4a and 4b. However, one must distinguish between values of L/R . The weakening effect of length carries over for this loading condition, since the effect of eccentricity is one of the "hidden" parameters. However, percentage-wise the effect of length is less than for the unpressurized loading. For example, from Figs. 4a and 4b, for R/t of 2500, the decrease in allowable stress in going from

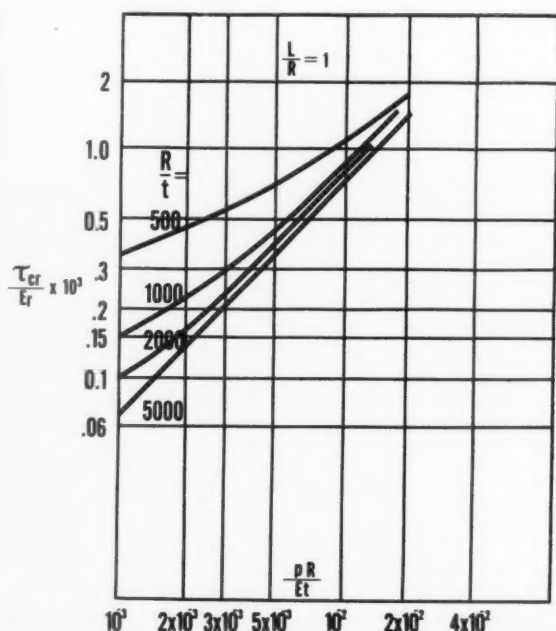


Fig. 6a Torsion buckling stress as a function of pressure hoop strain for cylinders with simply supported edges, $L/R = 1$

L/R of 1 to L/R of 6 is about 17 per cent. The corresponding decrease for the same cylinders when unpressurized is about 37 per cent according to Fig. 1b.

For conventional materials, the tensile yield strain $(\sigma_{ay}/E) + 0.002$ is about 0.007. Therefore this value has been used for σ_{ay} in preparing the curves in Fig. 4. None of the available test values of pR/Et exceeded 0.0025 $[(pR/Et)/0.007 \approx 0.35]$. More tests should be carried out for values of pR/Et greater than 0.0025 to establish the correct shapes of the curves in Figs. 4a and 4b. It is of interest to note that previous investigators suggest the use of the parameter $(p/E) \times (R/t)^2$ which stems from the theoretical considerations. The following example is given to illustrate the shortcomings of the use of that parameter. Suppose we have two cylinders of the same material, say 2024 ST aluminum, one with $R/t = 500$, the other with $R/t = 5000$. If we let $p = 100$ psi for the first cylinder and $p = 1$ psi for the second, $(p/E) (R/t)^2$ is 2.5 for both cylinders. However, the first cylinder presumably has failed, since $pR/t = 50,000$ psi. Meantime the second cylinder is working at a hoop stress of only 5000 psi.

The curves for $R/t = 5000$ in Figs. 4a and 4b have been drawn to fit the general trend of the family of curves in that figure. Test data are needed to verify this trend.

Combined Bending and Internal Pressure

This loading condition occurs when a side load is applied to a missile tank. The test data are limited (25). Again there is a large scatter. The basic behavior of the structure under pressure is similar to that of the axially compressed pressurized cylinder. There is a rapid rise in allowable stress with a relatively small amount of internal pressure, followed by a leveling off. However, the maximum allowable stress for this loading condition exceeds the one for the axially compressed pressurized cylinder. The physical reasons for the increased buckling strength are as follows. First, as already explained for the unpressurized case, the maximum stress is localized. Secondly, a cylinder in bending "flattens" or changes shape in cross section. This type of deformation is opposite in di-

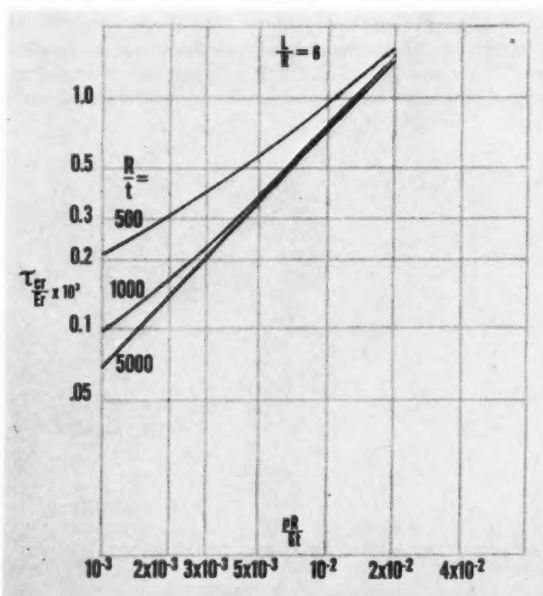


Fig. 6b Torsion buckling stress as a function of pressure hoop strain for cylinders with simply supported edges, $L/R = 6$

reaction to the bulging action due to the internal pressure, at least in the regions of maximum stress. Therefore, eccentricity due to internal pressure is lessened by this counteraction. The rise in allowable stress coefficient recommended for design is shown in Fig. 5 for $R/t = 3000$. The rise for $R/t = 1000$ is not clearly defined because of lack of test data. It appears to be at a smaller rate than for $R/t = 3000$. Additional test data are needed to confirm this trend.

Combined Torsion and Internal Pressure

There are enough test data to draw design curves as shown in Figs. 6. The increase due to internal pressure for this loading condition is very high and does not appear to approach a limit with increasing pressure as in the previous cases of compression and internal pressure and bending and internal pressure. However, the allowable stresses appear to approach a constant envelope curve independent of R/t for large internal pressure. Here again the parameter used is pR/Et . More test data are needed for $pR/Et > 0.002$ to establish the true nature of these curves. The present curves should not be extrapolated.

Combined Transverse Shear and Internal Pressure

No test data are available for this loading condition to the knowledge of the author. In light of the behavior of unpressurized cylinders under transverse shear, it might be recommended that the allowable stress be taken tentatively as 1.25 times the buckling stress for the loading of combined torsion and internal pressure discussed previously. This factor may be all right for cylinders with low internal pressure and low R/t . However, in actuality, the factor could turn out to be unity for cylinders with high internal pressure and high R/t .

Multiple Combined Loadings

Test data here are meager for cases involving internal pressure. Some data exist for combined compression, torsion and internal pressure, and combined compression, bending and internal pressure. The scatter of the test results is about the same as the scatter one obtains for unpressurized cylinders under combined loadings. Furthermore, the shapes of the interaction curves are similar to the curves representing the interaction of loading conditions for unpressurized cylinders. The curve shown in Fig. 7, which is recommended for design, is therefore valid for cylinders under combined loads

with and without internal pressure. Notice that the curve has been extended beyond both axes. The upper left-hand section represents combined tension and bending with little torsion. The lower right-hand section represents combined tension and torsion with little bending.

Combined Compression and External Pressure

According to theory (4), a linear interaction equation is suggested for this case.

Combined Torsion and External Pressure

Use the equation (51): $R_p + R_T^{1.5} = 1$.

Areas for Further Test

The design data presented in the previous sections have been based on existing known test data plus extrapolation in areas where no data were available. Therefore further tests must be performed for the following conditions in order to insure the reliability of design curves:

- 1 Unpressurized cylinders in axial compression with $R/t > 1500$ and $L/R > 3$.
- 2 Unpressurized cylinders in bending with $R/t > 1500$ and $L/R > 3$.
- 3 Pressurized cylinders in axial compression with $pR/Et > 0.0025$; also $R/t > 3000$.
- 4 Pressurized cylinders in bending with $pR/Et > 0.0025$; also $R/t > 3000$.
- 5 Pressurized cylinders in torsion with $pR/Et > 0.002$.
- 6 Pressurized cylinders in transverse shear.
- 7 Pressurized cylinders under combined loadings such as compression, bending and shear; tension, bending and shear; bending and torsion.

Any additional test information on the buckling of cylindrical shells also would be worth while. For example, all previous data are based on test specimens made up of sheets longitudinally spliced. Tests on cylinders made by circumferential splicing of sheets would be of interest.

Nomenclature

E	= Young's modulus
L	= length of cylinder
M	= applied bending moment
P	= applied axial load
p	= pressure
R	= radius of cylinder
S	= applied transverse shear force
T	= applied Torque
t	= thickness of cylinder wall
Z	= length parameter, $0.95 (L/R)^2 R/t$
ϵ	= strain
σ	= axial stress
τ	= shear stress

Subscripts

b	= bending
c	= compression
cr	= critical
hy	= hoop yield
r	= reduced
t	= tangent

References

- 1 Nash, W. A., "Bibliography on Shells and Shell-Like Structures," David W. Taylor Model Basin Rep. no. 863, Nov. 1954.
- 2 Kempner, J., "Postbuckling Behavior of Axially Compressed Circular Cylindrical Shells," *J. Aeron. Sci.*, vol. 21, no. 5, May 1954, pp. 329-335.
- 3 Loo, T. T., "Effects of Large Deflections and Imperfections on the Elastic Buckling of Cylinders Under Torsion and Axial Compression," Proc. Second U. S. National Congress of Applied Mechanics, 1954, pp. 345-357.
- 4 Mushtari, Kh. M. and Sakhnev, A., "Stability of Cylindrical and Conical Shells of Circular Cross-Section Subjected to Simultaneous Action of

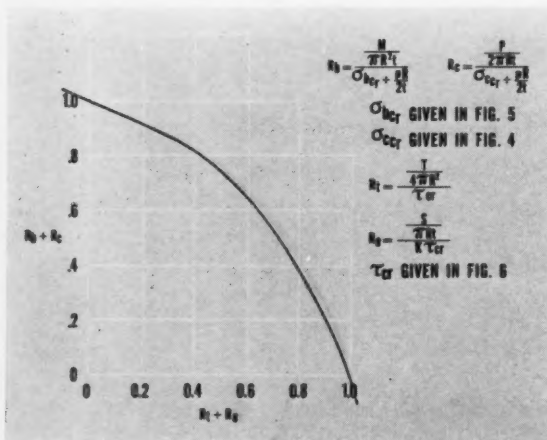


Fig. 7 Buckling for combined compression, bending, shear, torsion and internal pressure

Axial Compression and Normal External Pressure," *Prikladnaya Matematika i Mekhanika*, vol. 18, 1954, pp. 667-674.

5 Krivetsky, A., "Plasticity Coefficients for the Plastic Buckling of Plates and Shells," *J. Aeron. Sci.*, 1955.

6 Nash, W. A., "Effect of Large Deflections and Initial Imperfections on the Buckling of Cylindrical Shells Subjected to Hydrostatic Pressure," *J. Aeron. Sci.*, vol. 22, no. 4, April 1955, pp. 264-269.

7 Klein, B., "Interaction Equation for the Buckling of Unstiffened Cylinders Under Combined Bending, Torsion, and Internal Pressure," *J. Aeron. Sci.*, vol. 22, no. 8, Aug. 1955, p. 583.

8 Yoshimaru, Y., "On the Mechanism of Buckling of a Circular Cylindrical Shell Under Axial Compression," NACA TM 1390, July 1955.

9 Gerard, G., "Compressive and Torsional Buckling of Thin-Walled Cylinders in Yield Region," NACA TN 3726, 1956.

10 Thielemann, W. and Breyer, H. J., "Contribution to the Question of Buckling of Thin-Walled Compressed Circular Cylinders," *Luftfahrt*, June 1956.

11 Galletly, G. and Vart, R., "Effects of Boundary Conditions and Initial Out-of-Roundness on the Strength of Thin-Walled Cylinders Subjected to External Hydrostatic Pressure," *J. Appl. Mech.*, Sept. 1956.

12 Schmitt, A. F., "Dynamic Buckling Tests of Aluminum Shells," *Aeron. Engng. Rev.*, vol. 15, no. 9, Sept. 1956, pp. 54-58.

13 Becker, H. and Gerard, G., "Torsional Buckling of Moderate Length Cylinders," *J. Appl. Mech.*, vol. 23, no. 4, Dec. 1956, pp. 647-648.

14 Yoshimaru, Y. and Niisawa, J., "Lower Buckling Stress of Circular Cylindrical Shells Subjected to Torsion," *J. Aeron. Sci.*, vol. 23, no. 3, March 1957, pp. 211-216.

15 Shapovalov, L. A., "Influence of Internal Pressure on Critical Torsional Stress for Infinitely Long Cylindrical Cylinders" (in Russian), *Prikladnaya Matematika i Mekhanika*, vol. 20, no. 5, Sept.-Oct. 1956, pp. 669-671.

16 Kempner, J., Pandalai, K. A. V., Patel, S. and Crouzet-Pascal, J., "Postbuckling Behavior of Circular Cylindrical Shells under Hydrostatic Pressure," *J. Aeron. Sci.*, vol. 24, no. 4, April 1957, pp. 253-264.

17 Gerard, G., "Plastic Stability of Thin Shells," *J. Aeron. Sci.*, vol. 24, no. 4, April 1957, pp. 269-274.

18 Bijlaard, P. P., "Buckling Under External Pressure of Cylindrical Shells Evenly Stiffened by Rings Only," *J. Aeron. Sci.*, vol. 24, no. 6, June 1957, pp. 436-447.

19 Hoff, N. J., "Buckling of Thin Cylindrical Shell Under Hoop Stresses Varying in Axial Direction," ASME Summer Conference, Berkeley, Calif., Paper 57-Apm, 20, 8 pp. June 1957.

20 Gerard, G. and Becker, H., "Handbook of Structural Stability, Part III, Buckling of Curved Plates and Shells," NACA TN 3783, Aug. 1957.

21 Loo, T. T., "An Extension of Donnell's Equation for a Circular Cylindrical Shell," *J. Aeron. Sci.*, vol. 24, no. 5, May 1957, p. 390.

22 Harris, L. A., Suer, H. S., Skene, W. T. and Benjamin, R. J., "The Stability of Thin-Walled Unstiffened Circular Cylinders Under Axial Compression Including the Effects of Internal Pressure," *J. Aeron. Sci.*, vol. 24, no. 8, Aug. 1957, pp. 587-596.

23 Kusmiss, I., "Compressive Strength of Thin-Walled Cylinders, Bending and Torsion Strength," *Product Engng.*, July 1958.

24 Harris, L. A., Suer, H. S. and Skene, W. T., "The Effect of Internal Pressure on the Buckling Stress of Thin-Walled Circular Cylinders Under Combined Axial Compression and Torsion," *J. Aeron. Sci.*, vol. 25, no. 2, Feb. 1958, pp. 142, 143.

25 Harris, L. A., Suer, H. S., Skene, W. T. and Benjamin, R. J., "The Stability of Thin-Walled Unstiffened Circular Cylinders Under Bending Including the Effects of Internal Pressure," *J. Aeron. Sci.*, vol. 25, no. 5, May 1958, pp. 281-287.

26 Hodge, P. F., Jr. and Nardo, S. V., "Carrying Capacity of an Elastic-Plastic Cylindrical Shell with Linear Strain Hardening," *J. Appl. Mech.*, vol. 25, no. 1, March 1958, pp. 79-85.

27 Needham, R. A., "Buckling Stresses of Plates and Shells," Course notes for "Optimum Design of Structures," Univ. Calif., Los Angeles, July 1958.

28 Donnell, L. H., "Effect of Imperfections on the Buckling of Thin Cylinders under External Pressure," *J. Appl. Mech.*, vol. 23, no. 4, Dec.

1956, pp. 569-575.

29 Nash, W. A., "Buckling of Initially Imperfect Cylindrical Shells Subjected to Torsion," *J. Appl. Mech.*, vol. 24, no. 1, March 1957, pp. 125-130.

30 Peterson, J. P., "Bending Tests of Ring Stiffened Circular Cylinders," NACA TN 3735, 1956.

31 Needham, R. A., "Design of Round Tubes for Combined Bending and Torsion," *Product Engng.*, Aug. 1955, pp. 205, 207 and 209.

32 Ades, C. S., "Bending Strength of Tubing in the Plastic Range," *J. Aeron. Sci.*, vol. 24, no. 8, Aug. 1957, pp. 605-610.

33 Radhakrishnan, S., "Plastic Buckling of Circular Cylinders," *J. Aeron. Sci.*, vol. 23, no. 9, Sept. 1956, pp. 892-894.

34 Eden, J. J., "Graphical Method of Designing Thin-Wall Cylinders," *Product Engng.*, vol. 25, no. 10, Oct. 1954, pp. 180-188.

35 Wenk, E., Jr., Slankard, R. C. and Nash, W. A., "Experimental Analysis of the Buckling of Cylindrical Shells Subjected to External Hydrostatic Pressure," *Proc. Soc. Exp. Stress Analysis*, vol. 12, no. 1, 1954, pp. 163-180.

36 Slankard, R. C., "Tests of the Elastic Stability of a Ring Stiffened Cylindrical Shell, Model BR-4, Subjected to Hydrostatic Pressure," David Taylor Model Basin Rep. no. 876, Feb. 1955.

37 Almyae, N. A., "Critical Load of a Long Cylindrical Shell in Torsion" (in Russian), *Prikladnaya Matematika i Mekhanika*, vol. 18, no. 1, Jan.-Feb. 1954, pp. 27-34.

38 Kirstein, A. F. and Slankard, R. C., "An Experimental Investigation of the Shell-Instability of a Machined Ring-Stiffened Cylindrical Shell under Hydrostatic Pressure, Model BR-4A," David Taylor Model Basin Rep. no. 997, April 1956.

39 Harris, L. A., "Axial Compression Buckling of a Pressurized Cylinder with a Thermally Induced Ring Compression," *J. Aeron. Sci.*, vol. 23, no. 12, Dec. 1956, pp. 1120-1121.

40 Hai-Chang, H. and Po-Ming, S., "On the Equilibrium and Stability of Elastic Thin-Walled Cylinders," *Scientia Sinica*, vol. 5, no. 2, June 1956, pp. 185-204.

41 Wenk, E., Jr. and Kennard, E. H., "The Weakening Effect of Initial Tilt and Lateral Buckling of Ring Stiffeners on Cylindrical Pressure Vessels," David Taylor Model Basin Rep. no. 1073, Dec. 1956.

42 Kirstein, A. F. and Wenk, E., Jr., "Observations of Snap-Through Action in Thin Cylindrical Shells Under External Pressure," David Taylor Model Basin Rep. no. 1062, Nov. 1956.

43 Donnell, L. H., "Effect of Imperfections on Buckling of Thin Cylinders with Fixed Edges Under External Pressure," Third U. S. National Congress of Applied Mechanics, Brown University, June 1958.

44 Langhaar, H. L. and Borelli, A. P., "Buckling and Post-Buckling Behavior of Cylindrical Shells Subjected to External Pressure," Ninth Int. Congress of Applied Mechanics, Brussels, Belgium, Sept. 1956.

45 Vol'mir, A. S., "On the Influence of Initial Imperfections on the Stability of Cylindrical Shells Under External Pressure," *Doklady Akad. Nauk SSSR*, vol. 113, no. 2, 1957, pp. 291-293.

46 Gerard, G., "An Evaluation of Structural Sheet Materials in Missile Applications," *Jet Propulsion*, vol. 28, no. 8, Part I, Aug. 1958, pp. 511-520.

47 Brush, D. O., "A Nonlinear Analysis of the Buckling of Circular Cylinders Subjected to Axial Compression and Internal Pressure," Ph.D. Thesis, Univ. of Illinois, 1957.

48 Kempner, J., "Recent Results in the Theory of Large Deflections of Cylindrical Shells," Ninth Int. Congress of Applied Mechanics, Brussels, Belgium, Sept. 1956.

49 Kozlov, M., "An Investigation of the Stability of a Thin, Elastic and Orthotropic Envelope by the Nonlinear Theory of V. Z. Vlassov, Part I," *Stroitelstvo*, vol. 3, May 1956, pp. 31-35.

50 Finkelshtein, R. M., "Stability of Thin Walled Cylinder," *Izvestiya Akad. Nauk SSSR, Otdelenie Tekh. Nauk*, no. 7, July 1956, pp. 37-42.

51 Harris, L. A. and Suer, H. S., "Buckling of Thin Walled Cylinders Under Combined Torsion and External Pressure," *J. Appl. Mech.*, March 1959.

52 Ebel, H., "The Buckling of Cylinders Under Axial Loads According to Nonlinear Stability Theory," *Stahlbau*, vol. 27, no. 2, Feb. 1958, pp. 45-53.

Orbits of Cosmic Rockets Toward the Moon¹

L. I. SEDOV²

USSR Academy of Sciences
Moscow, USSR

THE REALIZATION and employment of space flights are based on a theoretical analysis and on numerical calculations of the equations of motion for vehicles in cosmic space. The basic requirements for the powering and guidance of the launching rocket, as well as the optimal and the acceptable conditions for the takeoff, are determined by computation.

As the initial coordinate system for describing the travel of cosmic vehicles, we may take a Cartesian coordinate system with the origin at the Earth's center, which is in translational motion relative to the stars. In many practical problems spherical coordinate systems have to be used, rigidly fastened with the Earth, with the origin at the center of the Earth and at various points on the Earth's surface. The movement of bodies relative to the moon or other planets is also to be considered.

Into the differential equations of motion of celestial ballistics describing free flight in cosmic space, we must introduce only the integration forces which are determined by Newton's universal gravitation law. In solving problems of hitting the moon and flight around the moon, we must consider the body's movement in a certain gravitational field produced by the sun, the moon and the Earth, taking into account the oblateness of the Earth.

In groping for the optimal conditions of a rocket's takeoff for the moon, approximation methods may be used, permitting us to consider the body's Keplerian motion relative to Earth when the distance from the moon is more than 66,000 km, and as Keplerian motion relative to the moon when this distance is less than 66,000 km.

For given points in the northern hemisphere, the optimal conditions for a takeoff in a first approximation when only the Earth's gravitational forces are considered may be obtained in the following way.

First, let us consider the collision case. Let A be the position of the point of cutoff of the rocket, B the position of the moon's center at the moment of collision, and O the Earth's center (see Fig. 1). Any orbit corresponding to a flight from point A to point B lies in a plane determined by the three points AOB . For a full determination of the orbit and the magnitude of the initial velocity V , it is sufficient to specify the inclination angle ϑ to the horizon of the initial velocity V .

From the solution of the two-body problem, we easily find the functional relation

$$\frac{V^2}{V_n^2} = f_1\left(\frac{r}{R}, \vartheta, \Phi\right) \quad [1]$$

where V_n is the parabolic velocity. The angle between the directions OA and OB , denoted as Φ , is called the angular distance. Point A , which is rigidly tied to the Earth, describes

a latitude line of the Earth as it rotates. The angle Φ changes within certain limits, which are seen in Fig. 1.

Since the ratio r/R is small and practically constant, according to function [1] the ratio V^2/V_n^2 depends essentially on ϑ and Φ . In Fig. 2, this dependence on ϑ , with $\Phi = \text{constant}$, is graphically represented by the continuous lines; the dotted lines represent the typical form of the rocket characteristics for various constant values of the rocket weight at the moment of cutoff.

It can be seen from Fig. 2 that the optimal starting time, at which the useful weight is the greatest, corresponds to the maximum possible value of the angular distance Φ , this condition determining the most advantageous starting time for the given point A . Evidently, in this case the plane of the orbit is normal to the plane of the Equator. The considered maximum value of the angle Φ differs for various positions of the moon in its orbit around the Earth. Evidently, for points in the northern hemisphere, the maximum value of Φ cor-

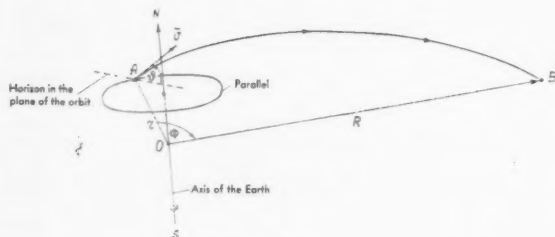


Fig. 1

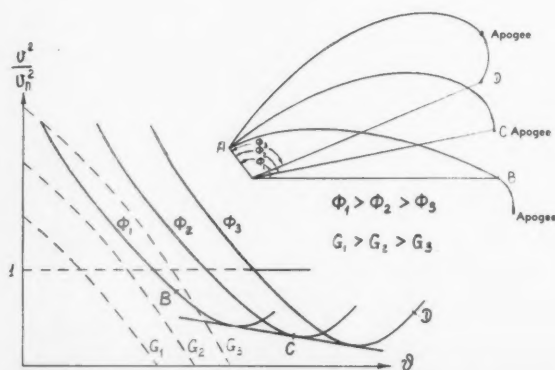


Fig. 2

¹ This paper was presented, along with the papers by Blagonravov and Krasovskii, at the ARS Annual Meeting, Nov. 17, 1959, Washington, D. C., in response to an official invitation of the Society.

² Chairman, Commission for Interplanetary Travel; President, International Astronautical Federation.

responds to the lowest position of the moon below the equatorial plane. The above conditions define the optimal time within a moon month, as well as the launching moment within a 24-hr period.

The previous conclusions were made without taking into account the rotation of the Earth and the advantage of using an additional velocity component of the rocket due to the rotation of the Earth. If the rotation of the Earth is taken into account, the inclination of the optimal orbit to the equatorial plane is reduced. Some corrections must also be made on account of the influence of the moon, the sun, the Earth's oblateness and the characteristics of the powered part of the flight.

An additional substantial increase in the payload can be secured by the choice of the launching point on the Earth's surface. These most favorable points lie near the Equator.

For the Soviet cosmic rockets, a version with an inclination of the initial part of the orbit to the equatorial plane amounting to 65 deg was decided, which is near to the most advantageous one.

The basic calculations of the equations of motion were made on high speed computers. Optimal trajectories were determined, and a set of trajectories closest to the optimum region was studied.

The choice of any one orbit may be begun by stating the total specific energy of the missile at the moment of cutoff. The value of the required total energy is determined by the mission of the flight and by a need for insuring favorable observation conditions for watching the missile from the territory of the USSR at the time of its hitting or passing near the moon. This also determines the duration of flight until the moon is reached. An analysis of the optimal conditions makes it evident that the time of flight from the Earth to the moon area must be approximately 0.5, 1.5, 2.5, 3.5 or 4.5 days.

After the required total energy has been determined, it is essential to have information about the possible payload weight and the necessary launching conditions for several days close to the most favorable day. The latter corresponds, for the northern latitudes, to the least inclination of the moon at the moment of the closest approach. This problem is answered through ballistic computations in which the rocket's characteristics are taken into consideration.

The computations show that a miss of 2 to 3 days on both sides of the optimal launching time keeps the useful weight loss within acceptable limits. Therefore only several days within each moon month appear to be the proper time for launching. A considerable deviation of the launching day from the optimal one causes major reduction of the possible payload weight.

For a detailed study of the influence of initial parameters on the trajectory characteristics, it appeared helpful to establish some essential properties of a set of trajectories, of which the central trajectory hits the center of the moon. The following properties of a set of trajectories, determined as in the foregoing, are sufficiently accurate; the use of these properties greatly facilitates the solution of many practical problems.

1 Near the moon, in a limited area around the central trajectory which may be considered as straight line, the nearby trajectories in the motion relative to the moon over distances up to 20,000 km, form a set of trajectories that have a rotational symmetry about the central axial path.

2 In the vicinity of the moon, the trajectories are approximately conic sections which lie in meridional planes.

3 The various orbits of this family may be obtained for small deviations from the principal values of the six independent parameters. The coordinates of the rocket and the components of its absolute velocity at the moment of cutoff may be considered as the six parameters.

4 A change in the increment of any individual parameter or a proportional change in any combination of the six param-

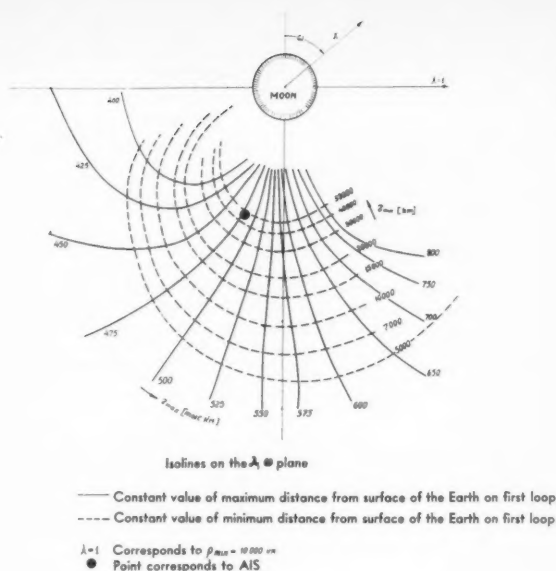


Fig. 3

eters leads to various orbits of the set, all of which lie in the same meridional plane.

5 A general nondimensional variable λ can be introduced for all meridional planes, equal to the ratio

$$\Delta\xi/\Delta\xi^* = \lambda$$

where

$\Delta\xi$ = increment of any parameter ξ at the end of launching
 $\Delta\xi^*$ = increment corresponding to the given minimal distance of the perturbed orbit from the center of the moon

Consequently, a universal relation

$$\rho_{min} = f(\lambda)$$

is valid in any meridional plane, for all various orbits. Here ρ_{min} is the minimal distance of the path from the center of the moon.

Using the properties previously indicated, the six-parameter set is converted to a two-parameter one, which may be mapped uniquely on an arbitrary plane π , in which the points are determined by the following polar coordinates: λ —the radius and ω —the polar angle. ω stands for the angle defining the meridional plane of the orbits.

This circumstance allows us to examine and describe the aggregate of perturbed movements through a certain clearly observable procedure.

It is convenient to draw in the plane π isolines of the various numerical characteristics of the trajectories. This is particularly important for examining a flight-around orbit, and for finding initial data corresponding to the orbits that have the required and the most advantageous characteristics. An example of two families of isolines is presented in Fig. 3; these were used to determine the orbit of the flight—a round trip of the Automatic Interplanetary Station (AIS).

The families of isolines of maximum and minimum distances from the object to the Earth during the first revolution after approaching the moon have been plotted on this figure. The initial energy for the chosen set of trajectories corresponds, in the absence of the moon's influence, to an apogee of 550,000 km from the Earth's center. For those trajectories of the set that lie to the left of the isoline of 550,000-km apo-

	Complete geocentric energy	Table 1			
		For the geocentric angular momentum			
		C_x	C_y	C_z	$C = \sqrt{C_x^2 + C_y^2 + C_z^2}$
Prior to passing the influence sphere of the moon	$-0.68 \text{ km}^2/\text{sec}^2$	$55 \times 10^3 \text{ km}^2/\text{sec}$	-30×10^3	21×10^3	67×10^3
After passing the in- fluence sphere of the moon	-0.74	-177×10^3	65×10^3	32×10^3	191×10^3

C_x = projection on the axis of vernal equinox x .
 C_y = projection on the axis perpendicular to the x axis in the equatorial plane.
 C_z = projection on the Earth's rotation axis.

gee, deceleration occurs and the apogee decreases; to the right of this line, acceleration takes place, the apogee increases, and the energy of the object with respect to the Earth rises after it approaches the moon. The corresponding quantitative effects can well be seen on the diagram.

The values of $\rho_{\min} = 7900$ and λ and ω , which were realized during the motion of the AIS, have been determined by computation. By plotting these data (Fig. 3), we obtain an apogee of 480,000 km, and a perigee height on the first revolution equal to 47,500 km.

The perturbing influence of the moon on the motion of the automatic station is very great; it can be characterized quantitatively by the data found in Table 1.

It is to be noted that the magnitude of the vector of angular momentum increases approximately threefold and its direction is almost reversed.

The π plane simplifies the analysis of the scattering effect of the initial parameters on the orbit characteristics. The introduction of the π plane allows us to combine the problems of hitting the moon and of flights close to the moon. The problem of determining flight-around trajectories with prescribed characteristics is reduced to that of hitting a given point in the π plane, corresponding to the required values of the orbit characteristics.

Flight around the moon can be realized along trajectories of different types.

The trajectory of a remote flight around the moon (at distances of about 40,000–100,000 km from the moon, with only slight influence of the latter) is near to an ellipse with a focus at the center of the Earth. Having this trajectory and starting from the northern hemisphere, the return path toward the Earth after passing the moon will be below the Equator. This makes it impossible to observe the object from the territory of the USSR when it is close to the Earth. Besides, for these trajectories the perigee distance from the center of the Earth is less than the radius of the Earth, and therefore the object enters the terrestrial atmosphere on the first revolution. Hence, its lifetime is short.

It was found to be of advantage to realize a trajectory of another type, with the object passing near the moon at a distance of about 5,000–20,000 km. In this case, the moon causes a big perturbation, as a result of which one can obtain a trajectory returning to the neighborhood of the Earth and subsequently have a satellite with a high perigee of about 40,000 km and an apogee of about 500,000 km, the return to Earth taking place over high latitudes of the northern hemisphere, which creates very favorable conditions for observation and reception of radio information. In addition, such trajectories are very convenient for solving the problem of object orientation and photographing at distances ranging between 40,000 and 150,000 km. Calculations have shown that within this range of distances, which is covered in about 12 hr, the direction of the object-to-moon vector in absolute space remains practically unchanged. This is an advantage for normal operation of the orientation system and for photography. This feature of the orbit allows switching on of the orientation system and the subsequent photographing operations by means of a program device operating from a preset timing mechanism.

In order to photograph the invisible side of the moon, it is necessary to launch the rocket on days near to the new moon. In that case, the invisible side of the moon is illuminated by the sun. The combination of favorable energy conditions with those of the illumination of the moon determines the months and the days which are most suitable for obtaining photographs of the back side of the moon.

The foregoing considerations served as a basis for choosing the flight-around trajectory for the third cosmic rocket, making use of the strong influence of the moon for the best solution of the problem in question.

The actual data concerning the orbits of the three Soviet cosmic rockets are given in the following and summarized in Table 2.

1 The last stage of the first cosmic rocket weighed 1472 kg without the fuel; the weight of the container, scientific apparatus and energy sources amounted to 361.3 kg. The rocket was launched toward the moon on Jan. 2, 1959; it

Table 2 Soviet cosmic rockets					
No.	Name of rocket	Launching date	Weight of last stage without fuel, kg	Weight of scientific apparatus and power supply, kg	Purpose
1	Lunik I	Jan. 2, 1959	1472	361.3	artificial planet of solar system to moon, Sept. 14, 1959 0 hr 02 min 24 sec Moscow time AIS photography of invisible side of moon
2	Lunik II	Sept. 12, 1959	1511	390.2	
3	Lunik III	Oct. 4, 1959	1553	435 (weight of AIS—278.5)	

passed north of the moon at a distance of about 5000 km from its surface. Flight time from the Earth to the proximity of the moon was 1.5 days.

It was in the launching of this rocket that parabolic speed was first exceeded, and consequently, after passing near the moon, the rocket continued to move away from the Earth, leaving the sphere of the Earth's gravitational field and becoming an artificial satellite of the sun.

Its orbit around the sun has the following characteristics:

Inclination of the orbit plane to the ecliptic plane $i = 1$ deg.

Minimum distance from the sun 146×10^6 km.

Maximum distance from the sun 197×10^6 km.

Corresponding period $T = 450$ days.

Minimum distance from the sun was reached in the middle of January 1959. The shortest distance from the orbit of the artificial planet to the orbit of Mars is 15×10^6 km.

Radio communication with the first cosmic rocket was maintained up to distances of 400,000–500,000 km.

2 The second cosmic rocket was launched with the aim of hitting the moon. The weight of the last stage without fuel was 1511 kg; the weight of the container with the scientific apparatus, 390.2 kg. The motion diagram is presented in Fig. 4.

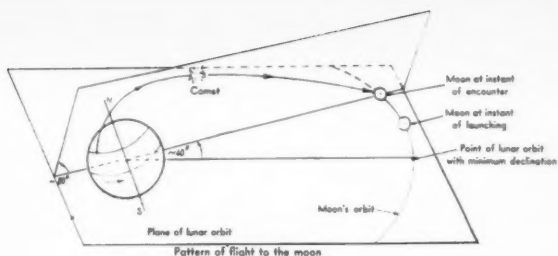


Fig. 4

The following data characterize the flight orbit of this rocket: The trajectory lies practically in one plane making an angle of 65 deg with the Equator. Flight from the Earth to the moon lasted about 1.5 days. The initial velocity in free flight exceeded the local parabolic speed.

With respect to the precision of initial data, a flight time of about 1.5 days proved to be more advantageous than schemes of hitting after longer flight times (2.5, 3.5 or 4.5 days), for which lesser initial energy is required. For a flight to the moon within about 0.5 day, too great energy consumption is required.

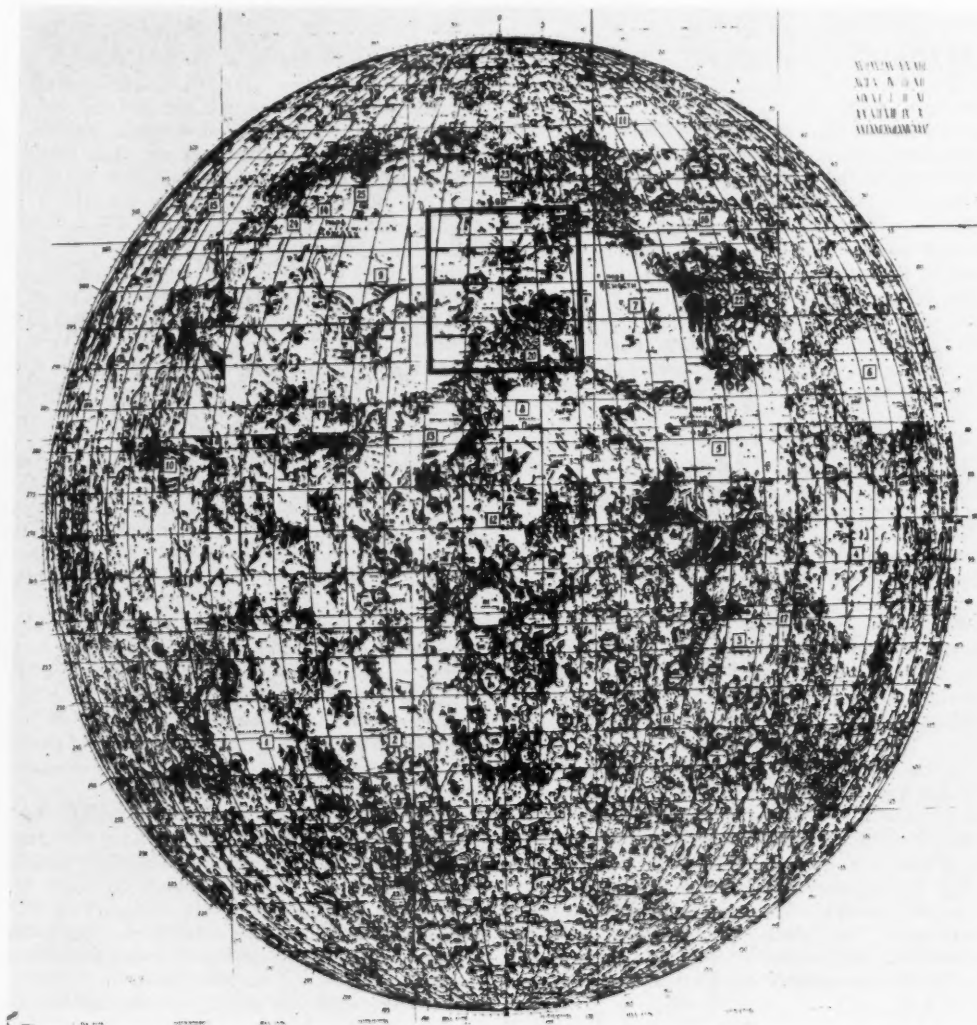


Fig. 5

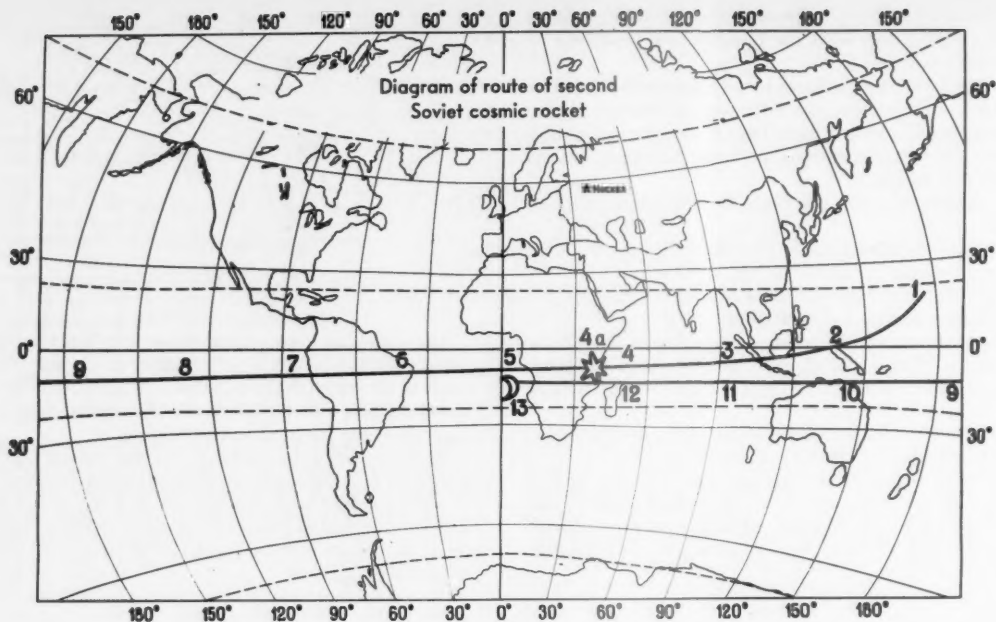


Fig. 6

The minimum geocentric speed on the orbit slightly exceeded 2 km per sec. The velocity of impact with the moon's surface was 3.3 km per sec. The velocity vector made an angle of about 60 deg with the moon's surface.

The point of impact on the moon is situated about 800 km to the north of the center of the visible lunar disk, south of the craters of Archimedes, Aristilles and Autolycus. The point of impact on the lunar map is shown on Fig. 5. The corresponding ρ_{\min} for the prolonged trajectory is 500 km.

The moment of impact was registered from an abrupt ceasing of radio signals on Sept. 14, 1959, at 0 hr 2 min 24 sec a.m. Moscow time.

This moment of impact agrees with the data of trajectory measurements which were carried out both during the flight and during the time interval directly preceding the hitting moment.

A projection of the trajectory of the container of the second cosmic rocket on the Earth's surface is given in Fig. 6.

3 The third cosmic rocket was launched on Oct. 4, 1959, for a flight around the moon. The weight of the last stage without the fuel was 1553 kg. The weight of the Automatic Interplanetary Station (AIS) with the apparatus and the energy sources, installed in the last stage of the missile, amounted to 435 kg.

During the flight of the AIS from the Earth to the moon the inclination of the orbit to the equatorial plane was equal to 55 deg. After the perturbation by the moon, further movement under the influence of the Earth's gravitation took place along a near elliptic orbit with an inclination to the Equator of about 80 deg. The calculation of further movement shows that the sun and the moon influence the AIS orbit so that the inclination of the orbit changes irregularly and decreases. On the tenth revolution, the inclination amounts to 48 deg. On the eleventh revolution, the inclination of the orbit under the influence of the moon increases again to 57 deg. It is noteworthy that the minimal distance from the Earth decreases from one revolution to another due to the influence of the sun and the moon. A calculation shows that after completing the eleventh revolution at the end of March, the AIS will enter the Earth's atmosphere in the northern hemisphere, thus ceasing to exist.

This circumstance is due to the orbit form and the character of its location relative to the Earth and the sun. This

effect, though unexpected at the first glance, depends only upon Newtonian forces. It is evident that such effects should be taken into account during theoretical analysis of problems concerning the structure of planet systems and the properties of the orbits of different planets and their satellites in the solar system. As a result of perturbation due to the sun, an evolution takes place which may lead to the collision of a satellite with its principal planet; therefore only satellites with orbits of certain types can "survive" for a long time.

Fig. 7 gives projections of the first revolution of the AIS orbit on the Equator plane and on the plane which is perpendicular to the direction from the Earth's center to the vernal equinoctial point.

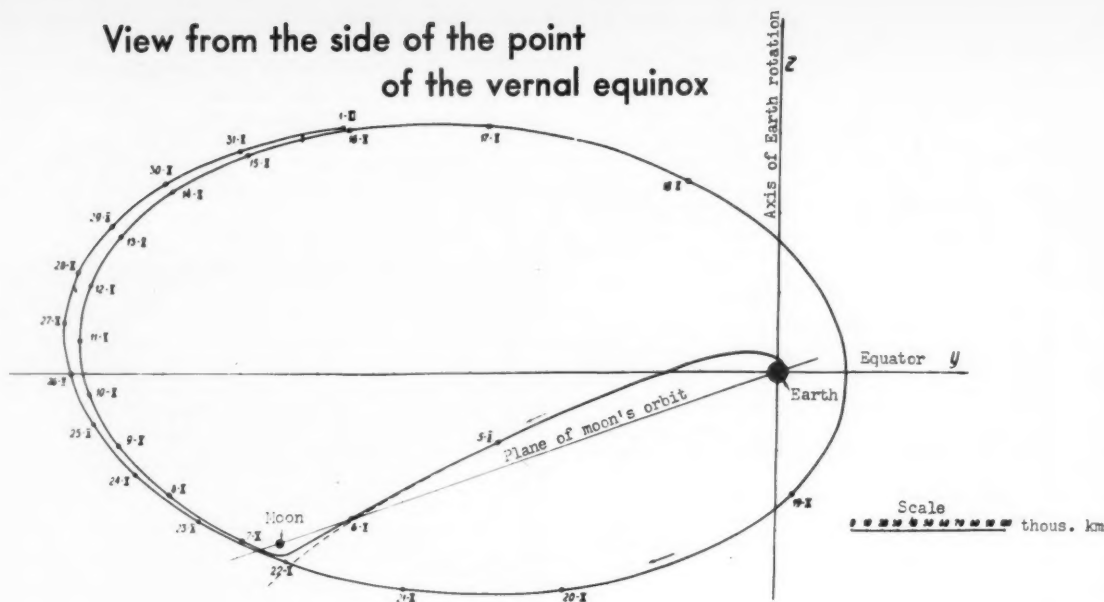
Fig. 8 gives the projection of one revolution of the AIS on the Earth's surface. The projection line shows loops when passing near the Earth's rotation axis both in approaching the Earth and in moving away from it.

Fig. 9 shows the orbit projection on the moon's surface (continuous line); points are marked signifying the minimal distance to the moon's center and the photographing time. A grid of selenographic coordinates is plotted on the moon's surface. The limits of the area which has been photographed by the AIS are marked with dotted line; the hatched part lies in shadow, the white part is sunlit.

The conditions for photographing were favorable with respect to the illumination of the invisible side of the moon, and an area comprising two thirds of the surface of the invisible side was photographed. An unfavorable factor in the process was direct illumination of the surface and, as a result, the absence of shadows from the accidents of the moon's surface. The picture was obtained only as a result of varying reflectivity of its different parts.

Before photographing, the orientation system was automatically switched on, turning one end of the axis of the AIS to the sun and the other end with the objectives of the cameras toward the moon. After stabilizing, the hatch covering the illuminator and protecting the transmitters of the moon orientation and the cameras was opened. After fixing the moon direction with a special photocell device, the light seeking devices reacting to the sunlight were automatically switched off; subsequently, the accuracy of the orientation of camera axis to the center of the moon was increased. After completing the orientation to the center of the moon, the process of

View from the side of the point of the vernal equinox



Projection on the plane of the Earth's Equator

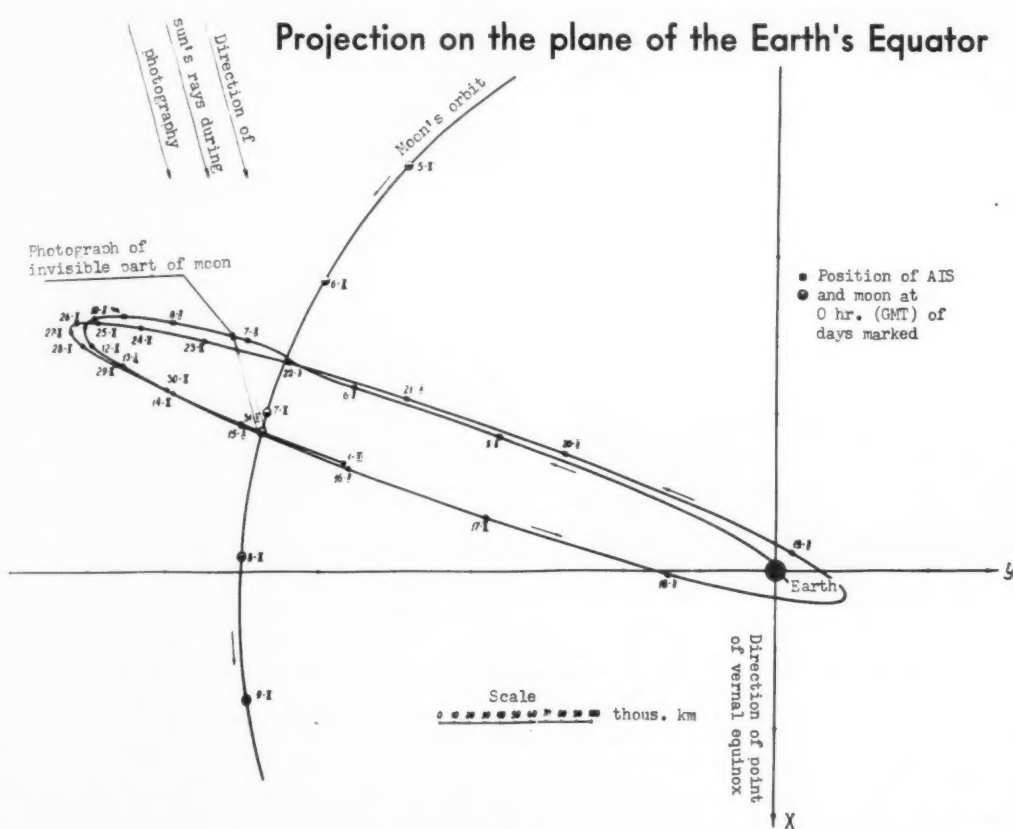


Fig. 7

photographing began at 06.30 hr, Moscow time, on Oct. 7, the AIS being then at a distance of 65,500 km from the moon's center. To insure favorable temperature conditions inside the AIS after the photographing process, the station was forced to rotate around its transverse axis with an angular velocity of 2 deg per sec. Thereupon the film was automatically de-

veloped, fixed and dried. The picture of the moon was transmitted to the Earth by means of a special television system.

Figs. 10, 11 and 12 give samples of photographs processed to date.

The pictures transmitted to the Earth from aboard the AIS show not only the side of the moon invisible from

Projection of the orbit of the AIS on the Earth

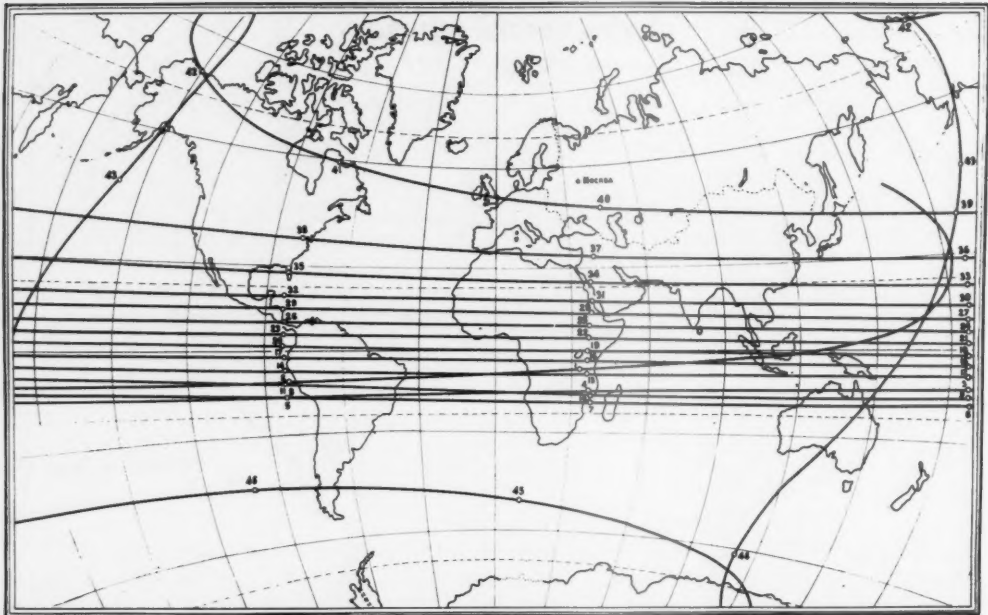


Fig. 8 Projection of the orbit of the AIS on the Earth. Numbers on the diagram correspond to the successive positions of the projection of the orbit of the AIS on the Earth's surface

1-16 hr, 8/4/59, 131 thous km from Earth;	2- 0 hr, 8/5/59, 183 thous km from Earth;	3- 6 hr, 8/5/59, 216 thous km from Earth;
4-16 hr, 8/5/59, 266 thous km from Earth;	5- 0 hr, 8/6/59, 300 thous km from Earth;	6- 6 hr, 8/6/59, 324 thous km from Earth;
7-16 hr, 8/6/59, 361 thous km from Earth;	8- 0 hr, 8/7/59, 379 thous km from Earth;	9- 6 hr, 8/7/59, 392 thous km from Earth;
10-16 hr, 8/7/59, 410 thous km from Earth;	11- 0 hr, 8/8/59, 423 thous km from Earth;	12- 6 hr, 8/8/59, 432 thous km from Earth;
13-16 hr, 8/8/59, 443 thous km from Earth;	14- 0 hr, 8/9/59, 452 thous km from Earth;	15- 6 hr, 8/9/59, 457 thous km from Earth;
16-16 hr, 8/9/59, 464 thous km from Earth;	17- 0 hr, 8/10/59, 468 thous km from Earth;	18- 6 hr, 8/10/59, 471 thous km from Earth;
19-16 hr, 8/10/59, 473 thous km from Earth;	20- 0 hr, 8/11/59, 474 thous km from Earth;	21- 6 hr, 8/11/59, 474 thous km from Earth;
22-16 hr, 8/11/59, 472 thous km from Earth;	23- 0 hr, 8/12/59, 469 thous km from Earth;	24- 6 hr, 8/12/59, 466 thous km from Earth;
25-16 hr, 8/12/59, 459 thous km from Earth;	26- 0 hr, 8/13/59, 453 thous km from Earth;	27- 6 hr, 8/13/59, 447 thous km from Earth;
28-16 hr, 8/13/59, 436 thous km from Earth;	29- 0 hr, 8/14/59, 425 thous km from Earth;	30- 6 hr, 8/14/59, 416 thous km from Earth;
31-16 hr, 8/14/59, 400 thous km from Earth;	32- 0 hr, 8/15/59, 384 thous km from Earth;	33- 6 hr, 8/15/59, 372 thous km from Earth;
34-16 hr, 8/15/59, 349 thous km from Earth;	35- 0 hr, 8/16/59, 329 thous km from Earth;	36- 6 hr, 8/16/59, 312 thous km from Earth;
37-16 hr, 8/16/59, 281 thous km from Earth;	38- 0 hr, 8/17/59, 253 thous km from Earth;	39- 6 hr, 8/17/59, 230 thous km from Earth;
40-16 hr, 8/17/59, 186 thous km from Earth;	41- 0 hr, 8/18/59, 148 thous km from Earth;	42- 6 hr, 8/18/59, 114 thous km from Earth;
43-16 hr, 8/18/59, 52 thous km from Earth;	44- 0 hr, 8/19/59, 55 thous km from Earth;	45-16 hr, 8/19/59, 150 thous km from Earth;
	46- 0 hr, 8/20/59, 189 thous km from Earth;	

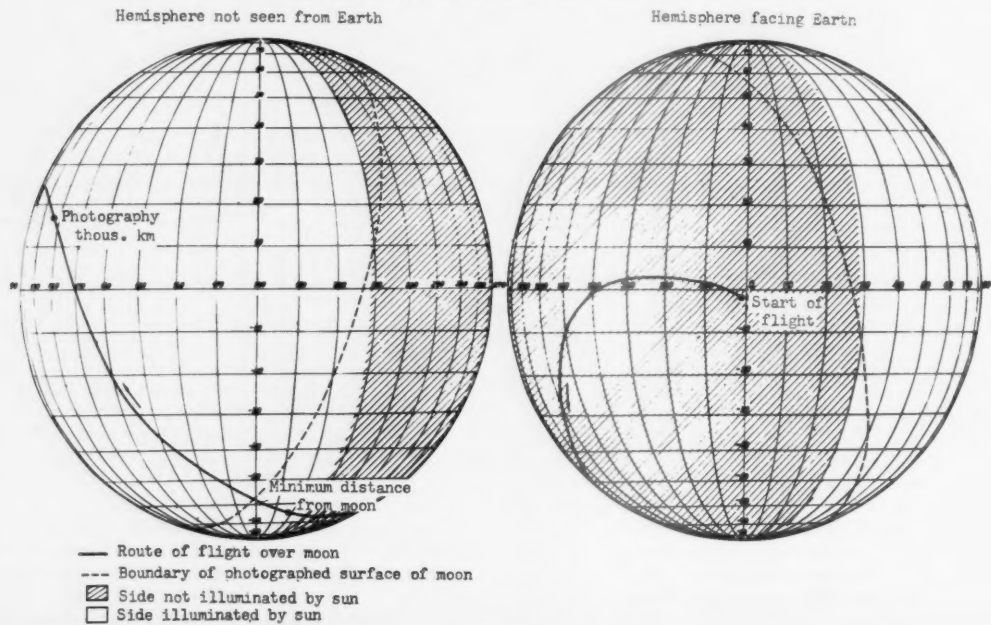


Fig. 9

the Earth, but a small portion of the moon visible from the Earth as well. This permitted connecting heretofore unknown objects on the moon's surface with those which are familiar, and to determine their coordinates on the moon.

Precise shapes have now been obtained for the objects situated at the edge of the visible disk, little known so far because of a distorted perspective. In other cases the objects were known only partially, and the pictures received allowed us to

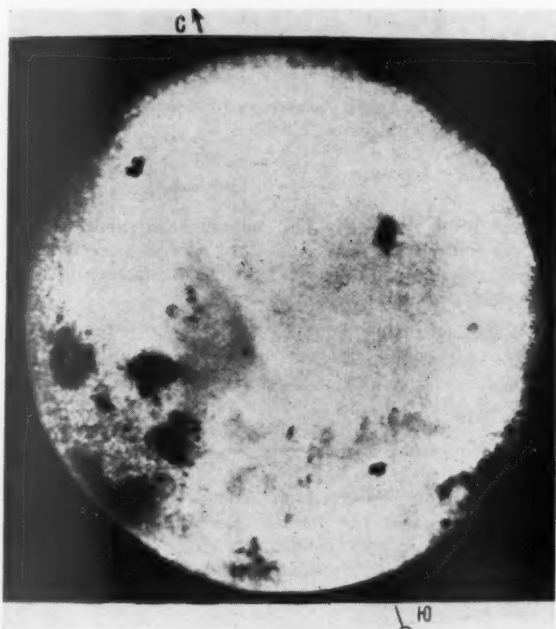


Fig. 10



Fig. 11

get more precise shapes for the parts situated on the visible side and to discover the shapes of their unknown continuations on the invisible side.

A mountain range, named the Sovietsky Mountain Range, and the presence of seas and craters, were discovered on the moon's invisible side. One of the seas has been named the Sea of Mehta, in memory of the first cosmic rocket launched on Jan. 2, 1959.

Figs. 10 and 11 show the original photographs, from which the obvious effects of radio noise have been cleared. The picture shown in Fig. 12 was obtained as a result of preliminary treatment of a number of photographs, representing a first attempt at a composite based on details revealed in several photographs. For a complete description of the invisible side of the moon, the photographing must be continued. It can be fairly expected that further pictures, with side illumination, will reveal more unknown formations on the other side of the moon.

We are of the opinion that this experiment of photographing in space and subsequently transmitting the pictures to Earth is interesting not only from the point of view of studying the nature of the back side of the moon, but is also of essential importance as a way of testing new methods in modern experimental astronomy.

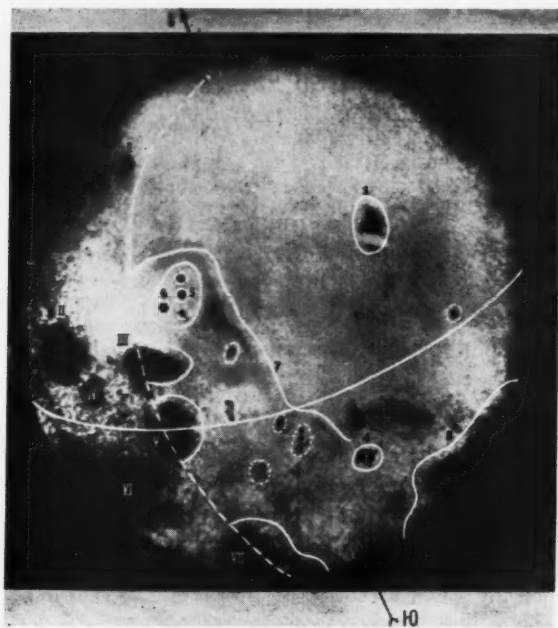


Fig. 12 Physical features of the lunar hemisphere invisible from the Earth, determined after preliminary processing of the photographs obtained from the AIS: 1 A large crater sea 300 km in diameter—the Sea of Moscow. 2 The Gulf of Astronauts of the Sea of Moscow. 3 Continuation of Mare Australe on the back side of the moon. 4 A crater with a central peak—Tsiolkovsky. 5 A crater with a central peak—Lomonosov. 6 Jolio-Curie Crater. 7 Sovietsky Mountain Range. 8 The Sea of Dream.

Physical features of the visible side of the moon: I Mare Humboldt; II Mare Crisium; III Mare Marginis; IV Mare Underum; V Mare Smythii; VI Mare Foecunditatis; VII Mare Australe.

The continuous line across the chart is the lunar equator. The broken line indicates the border between the hemispheres visible and invisible from the Earth. Features circled with a continuous line have been definitely established as a result of preliminary examination; features circled with a broken line are to be further studied with regard to their shape; features circled with a dotted line are being studied with regard to their classification; with regard to the other parts, the photographs are being studied further.

Some Problems of Providing for Scientific Research on Rockets¹

A. A. BLAGONRAVOV²

USSR Academy of Sciences
Moscow, USSR

MODERN rocketry provides the scientist with a powerful tool for probing mysteries of nature heretofore inaccessible to man. Starting with vertical rocket launching, followed by placing artificial satellites in orbit with the aid of rockets, and finally launching cosmic rockets for the investigation of cosmic space in the vicinity of the moon. Soviet scientists obtained within slightly more than a decade substantially new data on the properties of the Earth's upper atmosphere, on the phenomena that take place there, on the composition of cosmic radiation, and on the properties of interplanetary matter. As is known, the research performed to date culminated in the first photographs of the dark side of the moon.

Soviet scientists owe this success both to the vigorous development of rocketry proper, and to rapid progress in many fields of science (radio engineering, electronics, physics and chemistry of metals, etc.). Planned and systematic work was carried out in the Soviet Union to perfect the rockets themselves as well as the scientific apparatus and procedures for the scientific research, along with broadening the research programs. In addition, each successive experiment not only enriched science, but provided additional experience for further improvements to the necessary technical apparatus, and raised new technical problems in turn. At the same time, each experiment showed the way to new techniques and constructions, and helped eliminate numerous difficulties. The paper by Prof. Krasovskii discloses many scientific results obtained in the course of this research. My own task is to show several particular solutions that made possible research with the aid of rockets.

Even the very first rocket investigations of the Earth's atmosphere demonstrated an urgent need of isolating the measuring instruments from the rocket carrier, so as to get rid of disturbances and inaccuracies caused by rocket motion. It was also necessary to eliminate mutual influences of some instruments on other, i.e., to separate the devices from one another in space. Therefore, in almost all experiments, the scientific apparatus was installed in compartments isolated from the rocket itself.

Apart from isolating the payload compartment with the scientific apparatus, certain containers were ejected by special mortars, symmetrically located along the longitudinal axis of the rocket. Fig. 1 shows the placement of the mortars, which were equipped with pneumatic propulsion devices actuated in flight at an instant of time predetermined by the program. Such devices were used on certain geophysical

rockets during the IGY. The containers acquired an additional speed relative to the rocket, at a small angle with its longitudinal axis, and were thus kept at a satisfactory distance from the rocket and from each other.

Fig. 2 shows the flight trajectory of another type of instrument container, which was to be parachuted safely to the Earth (for example, carrying devices for obtaining air samples at certain altitudes). A general view of such a container is shown in Fig. 3. It consists of three parts (shown in Fig. 4). The head part is pressurized and contains electric batteries, devices for registering the readings of the manometers, a camera for photographing these readings, illumination for the scales of the gages, the program mechanism, amplifiers for the ion manometers, and cameras for taking pictures of clouds and the surface of the Earth and neighboring space. Screens

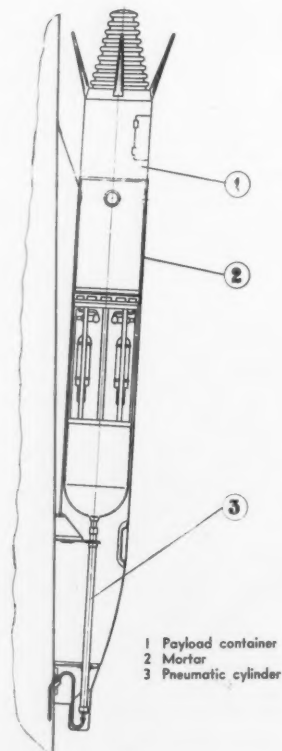


Fig. 1

¹ This paper was presented, along with the papers by Sedov and Krasovskii, at the ARS Annual Meeting, Nov. 17, 1959, Washington, D. C., in response to an official invitation of the Society.

² Member, Praesidium.

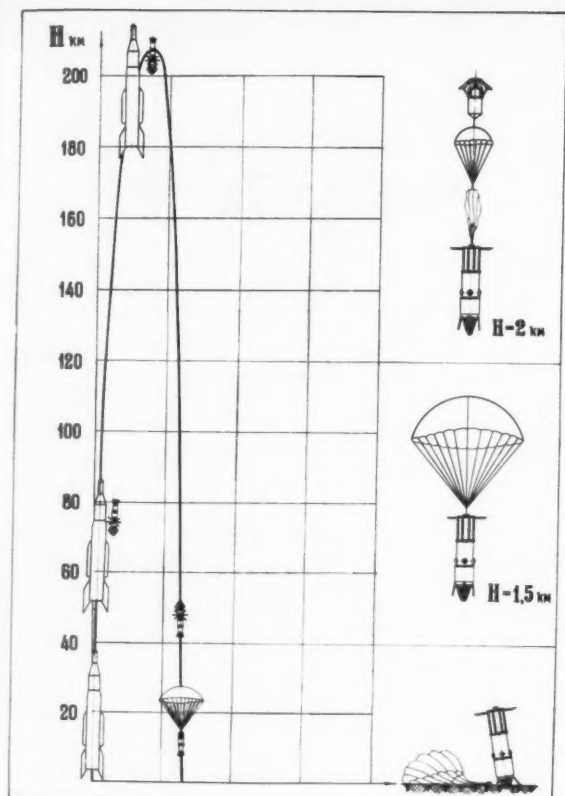


Fig. 2

are provided on the outside for registering meteor particles. There is also a bumper with a corrugated metal device for softening the landing impact. A fanning system of rods also serves the same purpose, and sometimes keeps the landing container in a vertical position. The middle compartment of the container is a latticed shell, containing glass bulbs for air sampling. The third part contains the parachute system.

Upon landing, the deformation of the head bumper generates a signal which uncouples the parachute, so as to prevent the wind from dragging the container along the ground.

This type of container is naturally not the only one. Mortars were also used to eject containers that did not need to be landed, for example, those carrying the telemetering system for the instrument readings. The principal advantage of the demonstrated system is therefore the possibility of performing different research programs with standard rockets without rebuilding the latter. All that need change is the equipment in the containers.

A second example of the problems encountered in the research concerns the orientation of the objects ejected in space, a task which also necessitated a number of investigations.

For example, one type of geophysical rocket carried a spherical container with a motor driven gyroscope wheel in its equatorial plane (Fig. 5). This gyroscope was accelerated directly before the launching of the rocket. After the container was separated from the rocket, the gyroscope axis remained almost vertical. Two photoelectric transducers were located in the equatorial plane 180 deg apart to provide a rough orientation. Depending on their position relative to the sun's rays, a signal was generated either to decelerate or to accelerate the gyroscope wheel, thereby tilting the container about the vertical axis in a direction necessary to bring the sun's ray to the null meridian between these transducers, where the instrument for precision orientation was installed. The latter disconnects the rough-orientation transducers at that instant and takes over control of the acceleration or deceleration of the wheel, thus aiming the null meridian directly at the sun (Fig. 6). In all the experiments performed, good orientation of the container was achieved until the latter entered the dense layers of the atmosphere.

Another method of orienting an object was used in the last launching of the lunar rocket to photograph the moon's surface from an automatic interplanetary station (AIS). (See Fig. 7.) The jet principle was used to rotate the station: Compressed air escaped from miniature nozzles, two pairs of which served to produce rotation about the longitudinal axis, and one about the transverse axes. Signals to start the gas flow from the various nozzles were generated by a special logical computer, which developed the optimum nozzle operating program from information on the direction of the sun's rays, obtained from the photoelectric transducers.

The flight trajectory of the AIS shows the successive steps in the operation of the orientation system (Fig. 8): 1—Start

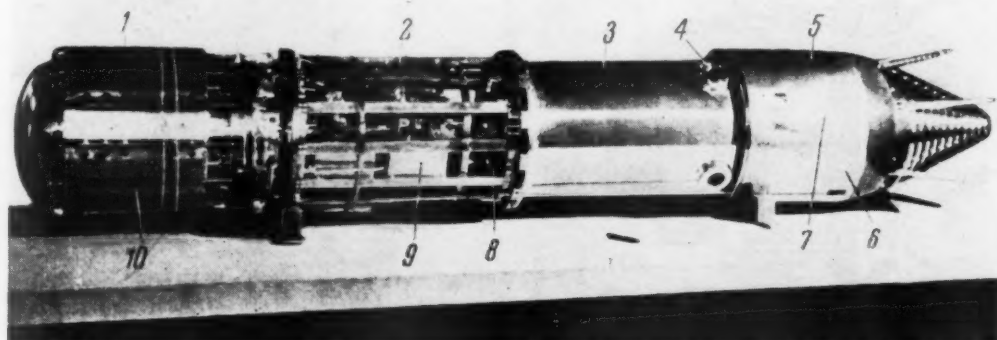


Fig. 3 1—Parachute compartment, 2—central compartment, 3—instrument compartment, 4—photographic compartment, 5—nose compartment, 6—storage battery compartment, 7—cassette for registration of micrometeorites, 8—manometers, 9—vessel for air sampling

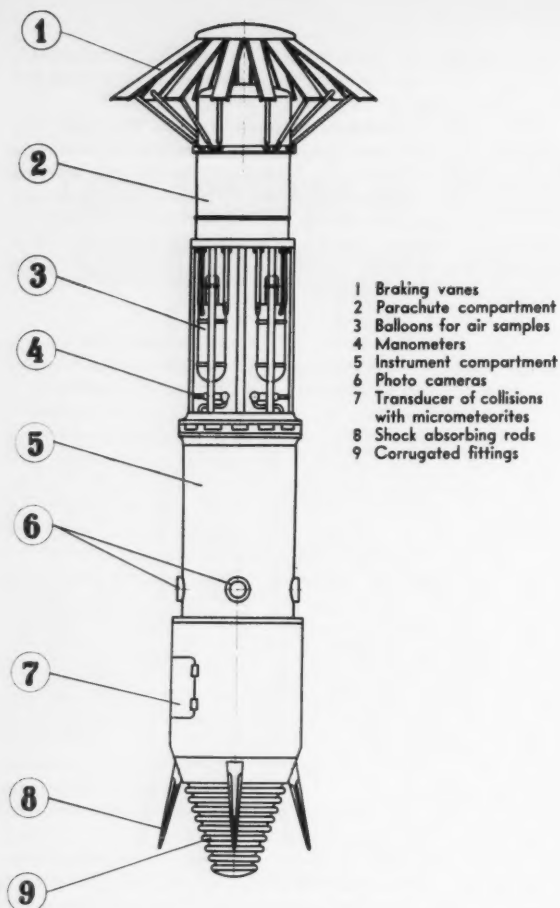


Fig. 4

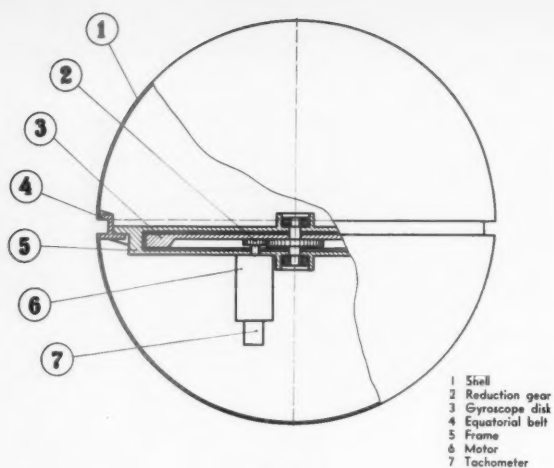


Fig. 5

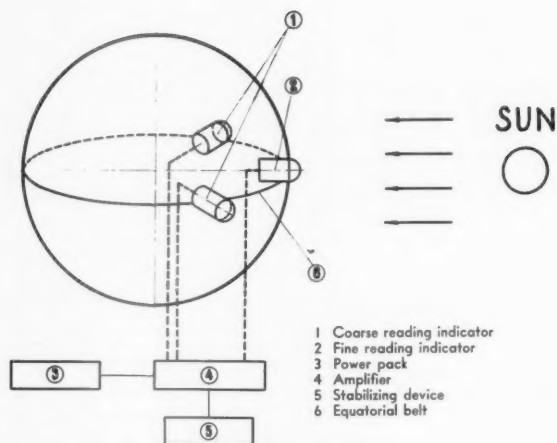


Fig. 6

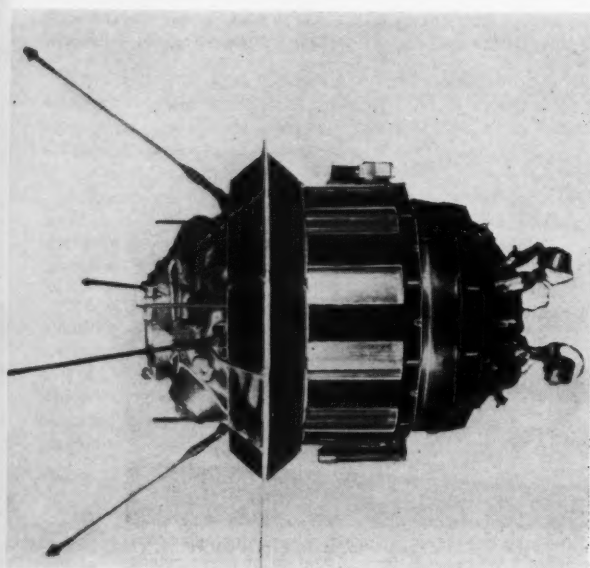
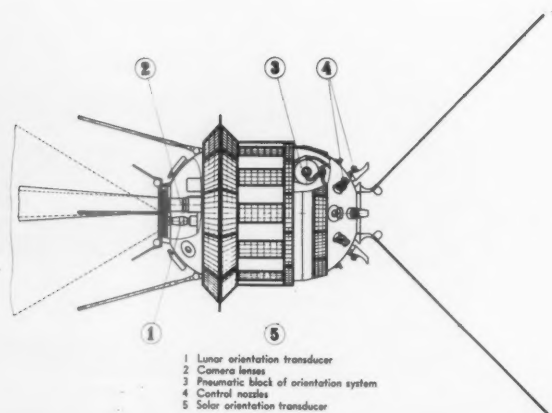


Fig. 7



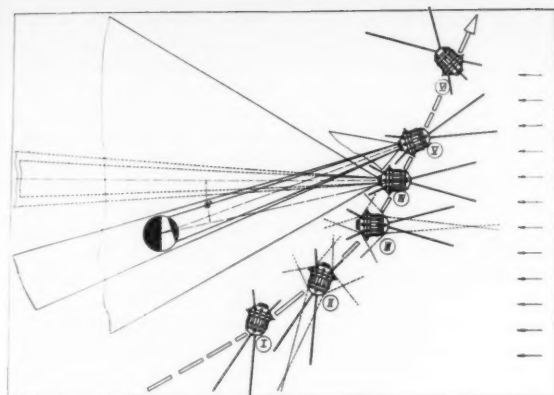


Fig. 8

of orientation; II—steading the station (elimination of rotation); III—station oriented toward the sun; IV—moon-orientation transducers are switched on automatically a certain time interval after the system is steadied; these transducers are located on the opposite side behind the window, the angle between the longitudinal axis aimed toward the sun and the orientation of the moon being 13 deg. Precise orientation toward the moon occurs in the section IV-V. Photography begins in position V. After the film advance is terminated, the window shutter is closed. In position VI, a pulse is produced to rotate the station to ensure further normal operation of the solar battery. In position V, one can see the field of view of the lenses of the two cameras.

As a third example of a solution of an individual technical problem raised by this research, we describe the heat control system used in the AIS.

The heating conditions of an AIS moving in orbit are determined by the joint action of the external and internal heat sources. The only external heat source is the sun. The internal heat is generated by the equipment. For normal operation of the AIS equipment, its temperature must be kept within fixed limits.

The AIS is a cylindrical body with two spherical end covers. Located inside the AIS is scientific, television and radio apparatus. The body of the station carries solar batteries, and on its cylindrical part is mounted a radiation surface (Fig. 9, 1) which is covered by rotating blinds (Fig. 9, 6) in the form of perforated cylindrical sleeves. The heat from the instruments is transferred to the shell through the frame by radiation and by forced circulation of the gas. The latter is produced by a fan (Fig. 9, 4) through an air duct (Fig. 9, 2).

The blinds open whenever the gas temperature rises above +25°C and close when the gas temperature drops below a permissible value. The use of blinds permits measurement of the optical coefficients of the outer surface of the AIS and thus regulates its heat conditions.

The nonradiating portion of the shell surface (Fig. 9, 3) is covered with screens, which serve to equalize the temperature field over the shell.

The power supply to the research and radio apparatus was always a troublesome matter and the subject of special care. The use of solar batteries on satellites and cosmic rockets has substantially eased the situation. Let us illustrate the general solution of the problems of power supply to the AIS.

The AIS power system contains autonomous chemical power sources to feed apparatus with a short operating time,

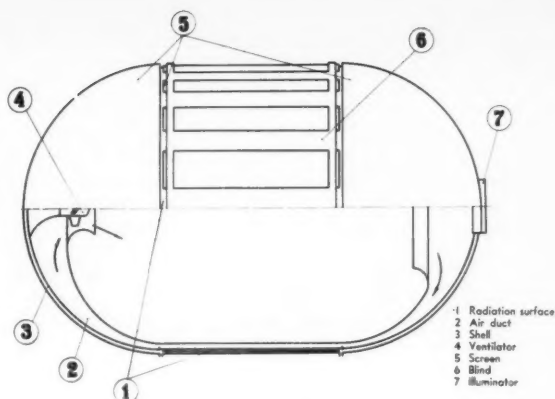


Fig. 9

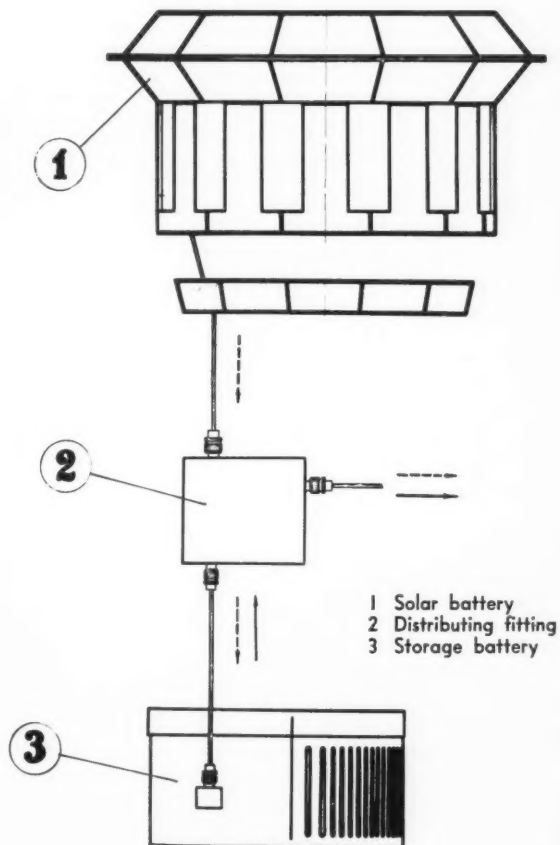


Fig. 10

as well as a centralized buffer block of chemical batteries (Fig. 10, 3). The spent energy of the buffer cells is replenished by the solar batteries (Fig. 10, 1), which are charged between broadcasts. During the time of the broadcast, the apparatus is fed from both the buffer and the solar batteries, via a distributing network.

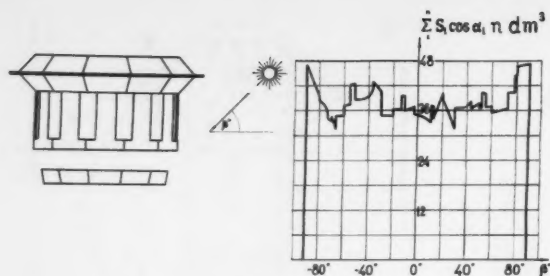


Fig. 11

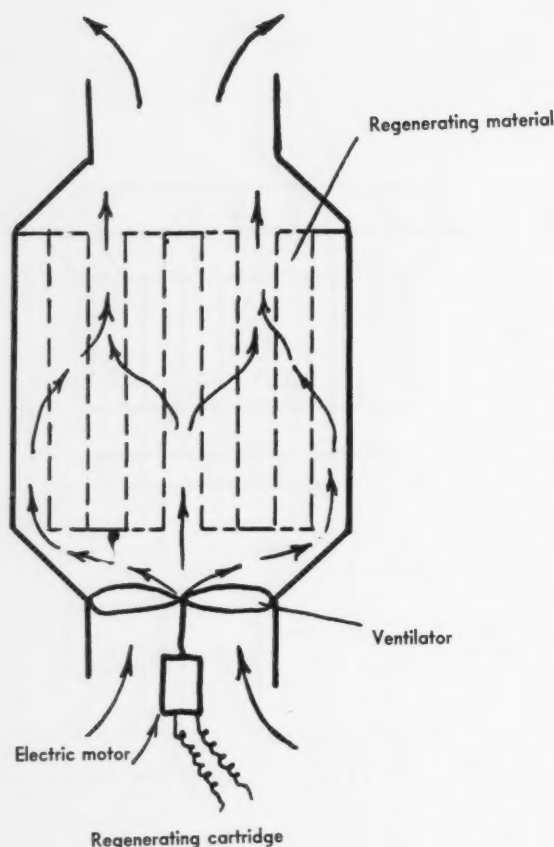


Fig. 12

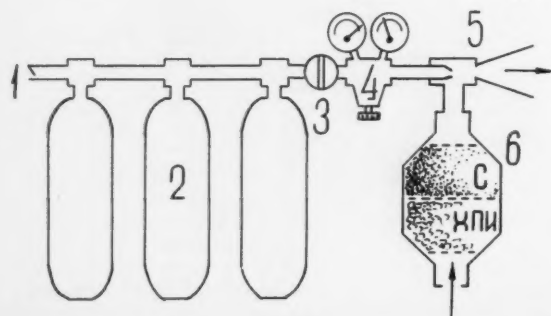


Fig. 13

Of particular interest in this system is the choice of shape of solar battery, which in turn influenced the overall view of the AIS. The shape selected insures high power stability in unoriented flight. By placing the elements of the solar battery on the surfaces of a 12-face prism and two truncated pyramids, the summary effective area of the entire battery, which is proportional to the output current, changes very little with changing direction of illumination.

The figure shows the variation of power with the angle of incidence of the rays. In the formula of Fig. 11, S_i is the illuminated area, α_i the angle of incidence of the ray on the face, and n_i the number of faces.

Finally, we dwell briefly on the organization of the physiological research, aimed at investigating the influence of various factors on living organisms during rocket flight. As is known, many flights of animals (principally dogs) were organized in the Soviet Union. These flights, too, necessitated the solution of many technical problems.

Let us describe a pressurized cabin for dogs and its equipment, as used in one type of geophysical rocket, designed for altitudes up to 475 km. The cabin permitted maintenance of normal pressure, gaseous air composition and relative humidity. It contained two removable trays for holding the animals, a regeneration plant and recording apparatus. The cabin was placed in the parachute equipped compartment of the rocket. The cabin was shaped nearly like a truncated cone, with bases in the form of spherical segments. The volume of the cabin was 460 liters. The inner wall of the cabin was covered with heat insulation.

In the initial experiments, the regeneration plant consisted of three 7-liter flasks, a reducer, an injector, a regeneration cartridge and control manometers (Fig. 12). In addition, to keep the air pressure in the cabin constant, a pressure regulator was used. In subsequent experiments, high activity chemical compounds were used to regenerate the air in the cabin. These were located in a specially constructed regeneration cartridge (Fig. 13). Draft was produced in the cartridge by an electric fan, which delivered 20 liters per min. Two cartridges were installed in the pressurized cabin, making the total volume of air 40 liters per min. With such a regenerating plant, the concentration of carbon dioxide in the cabin did not exceed 0.7 per cent, and the oxygen concentration remained practically constant.

To register the physiological functions, a set of medical apparatus was used, consisting of an automatic pressure

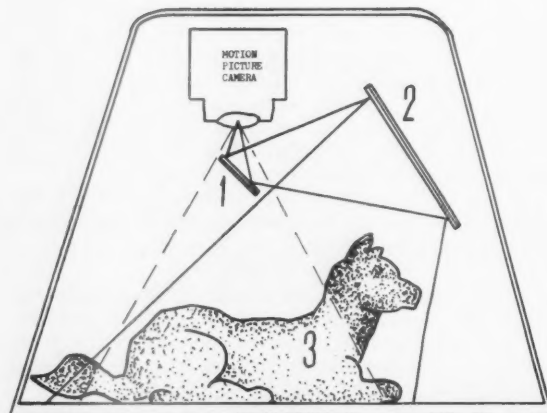


Fig. 14

recorder, an amplifier block, a matching network and a set of electrodes and transducers.

Records were made of the arterial pressure of the oscillations of the carotid (by means of a piezoelectric transducer), and of the depth and frequency of respiration. The respiration was recorded with a transducer comprising a rubber plate covered with a thin strain gage, the resistance of which increased with stretching of the rubber. The amplitudes of the records of breathing motion were regulated with a potentiometer.

The electrocardiograms of the animals were taken with the aid of a block consisting of four amplifiers feeding the vibrators of the automatic recorders.

In addition to recording the physiological functions, motion pictures were taken of the behavior of the dogs. A special electrically driven camera (fed with 26-30 v d-c) operating at 24 frames per sec was used. The camera cassettes held 300 m of film, enough for 11 or 12 min. The camera was provided with a short-focus lens of 20-28 mm focal length. The camera was mounted in the upper part of the cabin with the lens pointing downward. To increase the optical distance between the lens and the dogs, the pictures were taken through mirrors (Fig. 14).

The animals were illuminated with two 60-w bulbs. A watch with a second hand was included in the field of view of the camera.

The equipment installed in the cabin for a prolonged flight of an animal in a satellite—that of the historic Laika—was

more complicated. Particularly stringent requirements were imposed here on the pressurization of the cabin, which was in the form of a cylinder 650 mm in diameter and 800 mm long.

In addition to the equipment for air regeneration and temperature control, it became necessary to provide for automatic feeding, sanitation equipment, and telemetry of the air pressure, of the temperature at various points of the cabin, of electrocardiogram records, breathing depth, oscillations of the carotid, air pressure in the sphygmomanometer bag, and finally, the movements of the animal, which had limited freedom to lie down, stand and sit.

The data received made it possible to establish the variation of the physiological functions of the animal both during the active ascent of the rocket and during the orbiting of the satellite.

A discussion of these results is beyond the scope of this paper, particularly since a translation of an article on this subject was published in the October 1959 issue of *ARS JOURNAL*. However, I mention this example to illustrate one of the numerous sets of problems that must find technical solution in the organization of scientific research. Often the success or failure of an investigation depends on the solution of similar problems, which at first glance appear to be of secondary importance.

The success of the research now carried out in the USSR is evidence of an immense effort exerted toward solving numerous varied technical problems.

Results of Scientific Investigations Made by Soviet Sputniks and Cosmic Rockets¹

V. I. KRASOVSKI²

USSR Academy of Sciences
Moscow, USSR

THE ACHIEVEMENTS of the Soviet Union in rocketry made it possible to put into practice some new and important scientific explorations of the upper atmosphere and cosmic space. Soviet engineers and scientists created gigantic Sputniks and cosmic rockets. Geophysicists and astrophysicists placed their instruments on them to research different properties of the upper atmosphere and cosmic space, hard electromagnetic and corpuscular radiation of the sun, interplanetary dust and gaseous medium, magnetic fields, cosmic rays, planets and their satellites, and different processes around them. Before the launching of Sputniks, Soviet scientists were experienced in the exploration of the upper atmosphere with the help of geophysical rockets.

The launching of the first Soviet Sputnik marked a new era—an intensive assault aimed at complete mastery of the secrets of the upper atmosphere and interplanetary space and at the creation of continuously working laboratories beyond

the Earth's atmosphere. Every new Sputnik was more perfect than its predecessor and enriched our knowledge about the upper atmosphere and cosmic space.

The use of cosmic rockets is a further improvement in this respect. With their help, the scientists managed to get a fuller representation of huge processes in space surrounding the Earth, for the first time reaching another cosmic body—the moon—and getting information not known before.

The purpose of the present paper is to describe the results of scientific researches carried out by the Soviet Sputniks and cosmic rockets. Large groups of scientists, engineers and workers of many scientific institutions, design offices and industrial enterprises were engaged in this great research. All this became possible due to the high level of development of Soviet economics and industry. Valuable information about the upper atmosphere and cosmic space has been accumulated up to the present moment.

I have been instructed by all my colleagues to make a survey of the results of the subjects already treated. Much of it is still being treated and carefully studied.

Let us start with a few words about scientific research of the upper atmosphere. Before the launching of the first Soviet Sputnik, the upper atmosphere beginning with the

¹ This paper was presented, along with the papers by Sedov and Blagonravov, at the ARS Annual Meeting, Nov. 17, 1959, Washington, D. C., in response to an official invitation of the Society.

² Chief, Department for Research in Upper Atmospheric Physics, Institute of Atmospheric Physics.

200-km level was thought to be isothermal and to have a temperature of less than 1000 K, and, consequently, the scale height was thought small. However, by deceleration of the Sputniks, it was found that at a height of 220 km, the density of the atmosphere was equal to $2.5 \times 10^{-13} \text{ gm cm}^{-3}$. It exceeded what had been expected, and this result essentially changed the conceptions of density and temperature of the

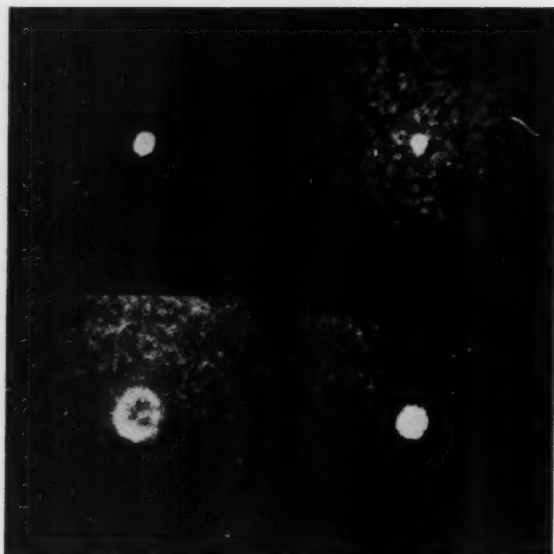


Fig. 1 Photo of an artificial sodium cloud at a distance of 152,000 km from Earth during the flight of the second cosmic rocket. The pictures were taken by an electron telescope with an exposure ~ 5 sec. The increase in diameter of the cloud corresponds to the sequence in time. The interval between the photos is 10 to 20 sec

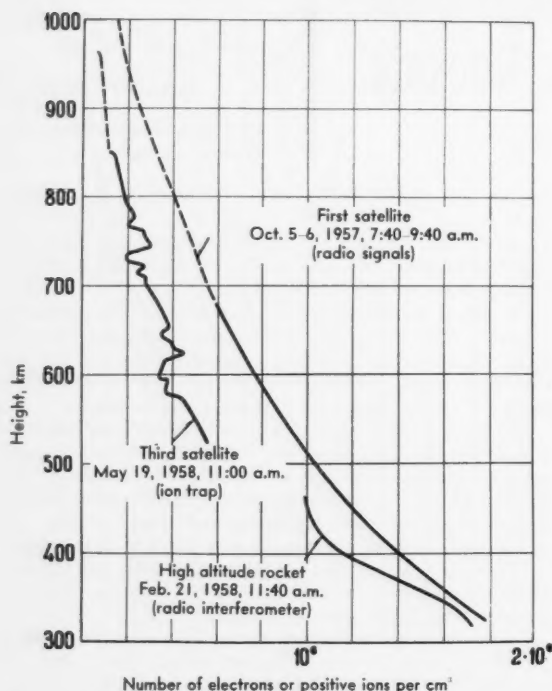


Fig. 2 Survey of different values of density of the upper atmosphere. The left curve represents data obtained by means of manometers; the right, by other means

upper atmosphere accepted before. By the change in the period of revolution of Sputniks around the Earth and by the change in the position of the perigee, it was found that, at the 220-km level, the density of the atmosphere was greater by day than at night and greater in the polar than in the equatorial regions.

To determine the exact coordinates of the cosmic rockets, a sodium cloud was tried. By means of a sodium vapor cloud the coordinates of the first and second cosmic rockets at a distance of 100,000–150,000 km were determined with an accuracy of a few angular seconds. The time of cloud formation was registered with an accuracy of some seconds in time. By way of preparation for this experiment, a sodium cloud was brought to being at the level of 430 km in twilight. Fig. 1 shows different stages in the formation of sodium clouds. By data on diffusion of this cloud, it was found that 1.8×10^8 particles cm^{-3} are present at this height. The comparison of values obtained with those from the retardation of the Soviet Sputniks showed that the estimated scale height at the 430-km level is 70 km. This points to the fact that the temperature of the upper atmosphere within the experimental region is 1600 K. For such a great scale height the density of air at a given level is much higher than was supposed previously.

Ionization and magnetic manometers were also mounted on the third Sputnik and their use allowed data about the density of the upper atmosphere to be obtained which agree with a new representation of the properties of the upper atmosphere within the error.

Fig. 2 shows the indicated properties of the upper atmosphere.

The third Soviet Sputnik carried a spectrometer for determining the nature of the atmospheric ions with a mass number of 6 up to 50 units. Before mounting this instrument on the Sputnik, it was tested on high altitude rockets. The ion of nitric oxide was found to be the most frequent up to the height of 250 km. The existence of this ion up to this height does not mean that it forms as a result of ionization of the neutral molecule of nitric oxide. As was shown by a number of theoretical and laboratory investigations, the ionized molecules of the nitric oxide appear in the upper layers of the atmosphere as a result of the reaction of an oxygen ion with a neutral molecule of nitrogen or in the reaction of the oxygen atom with an ionized molecule of nitrogen. The nitrogen ions found show that nitrogen molecules are present at altitudes up to 250 km. However, the exploration with the help of the third Sputnik revealed that there are only atomic ions of oxygen and nitrogen higher than 250 km; the ions of atomic oxygen are dominant, whereas the ions of atomic nitrogen constitute only several per cent of the oxygen ions. This is evidence that the upper atmosphere above 250 km has an atomic structure.

The third Sputnik and the cosmic rockets carried special ion traps which make it possible to estimate the ion density in the upper atmosphere and cosmic space. If a certain assumption is made as to the mechanism of charging the rocket and characteristics of the ion current depending on various differences of potentials between the electrodes of the ion trap, then the material obtained shows that the bodies are being charged in the ionosphere up to a negative potential of several volts. It has been shown that the estimated electron density is several million electrons cm^{-3} up to the height of 475 km, and that this is in good agreement with earlier investigations by ultra-short wave dispersion interferometers on high altitude rockets. It has also been found that there is a slow decrease in the density of ionized particles with height, and that above the maximum of the F_2 region, there are twice or three times as many electrons as below.

On the basis of the data about the electron density from the study of reception of radio signals from Sputniks, similar conclusions have been drawn. All the results are compared in Fig. 3.

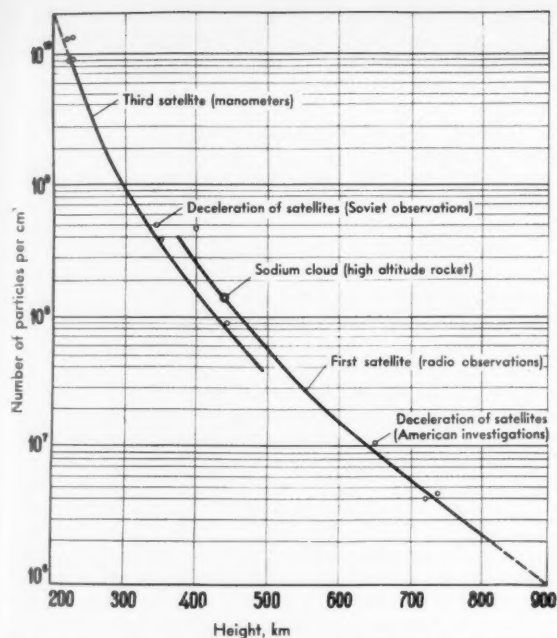


Fig. 3 Comparison of different values of the density of electrons in the upper atmosphere

All the cosmic rockets carried ion traps. They helped to determine the currents between the electrodes of ion traps at different distances from the Earth's center in cosmic space and near the moon. The preliminary treatment of the results allows us to assume that the density of ionized particles in the outer atmosphere at a distance of some radii from the Earth is of the order of several thousand ion pairs per cm^3 or less. Somewhat higher currents between the electrodes of an ion trap were observed near the moon. This requires further study.

Sputniks and cosmic rockets were used for the study of cosmic rays, using Geiger counters and scintillation counters combined with different absorbers. Fig. 4 illustrates the results of these investigations in comparison with the altitude dependence of the intensity of cosmic rays available since 1949. It concerns the particles capable of penetrating 10 gm cm^{-2} . The instruments of the second Sputnik made it possible to determine the intensity of cosmic rays as a function of the geomagnetic latitude. The results of these investigations

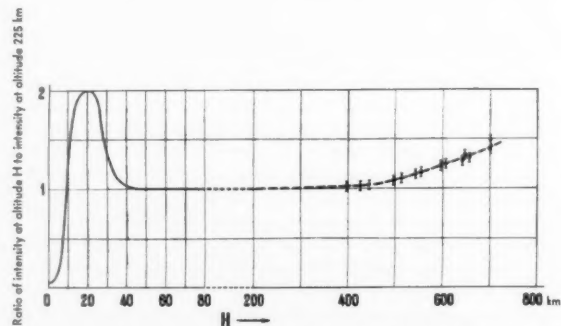


Fig. 4 The intensity of hard cosmic rays, penetrating 10 gm cm^{-2} , as a function of height. The solid curve represents the results obtained with rockets, the dashed curve above 400-km data obtained by the second Sputnik. The scale along the ordinate axis is in relative units

are given in Fig. 5. On Nov. 7, 1957, at 04:40 (Moscow time), an abnormally large increase in the intensity of cosmic rays was registered at high geomagnetic latitudes due to an external radiation zone (see Fig. 6). It was the first record of hard particles within an outer belt. There were no other explorations of this kind before at such a height.

Still more valuable information was obtained by the third Sputnik on regularity of change of intensity of pulse counting due to electrons of about 100 kev. Fig. 7 is a chart of data for May 15-22, 1958. A rapid growth of intensity of count-

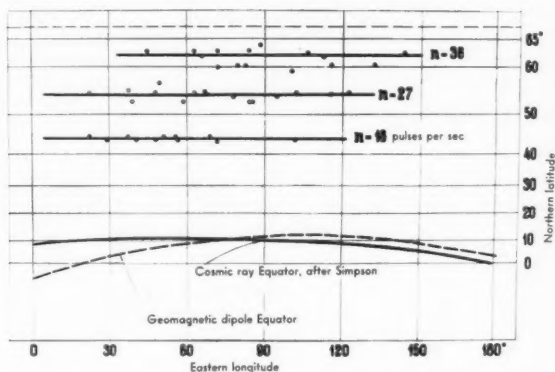


Fig. 5 Latitude relationship of hard cosmic rays, obtained with the help of the second Sputnik

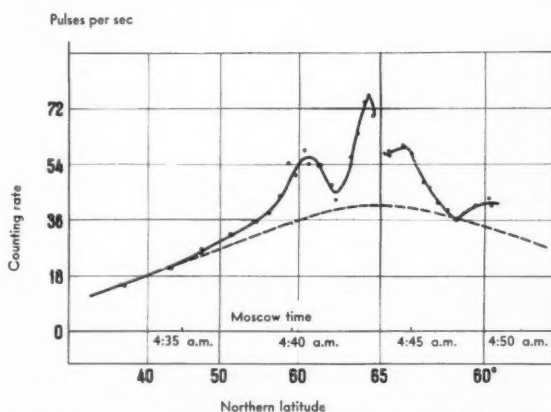


Fig. 6 Increase of the intensity of cosmic rays at high latitudes, discovered by the second Sputnik, Nov. 7, 1957. The dashed curve reflects the normal variation of the intensity, and the solid curve observed values

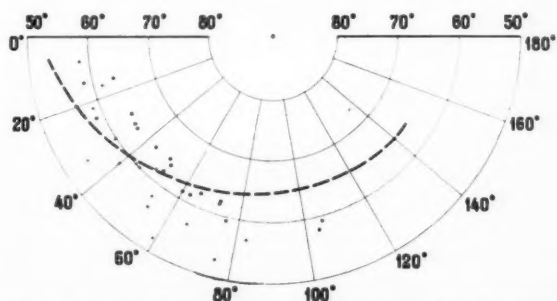


Fig. 7 Latitude distribution of intensity of 100-kev electrons. Black circles represent the position of the Sputnik when the instruments went off scale on the ascending loops and crosses the position of the Sputnik when they went back on scale in the descending loops. The dashed line is a geomagnetic parallel

ing is denoted by circles. Crosses represent the emergence of the Sputnik from the polar zone, where a higher intensity was observed. The crosses southward point to the relationship of the effect with height, since the crosses correspond to the backward loops, i.e., the greater height of flight. It was found that the zone of high intensity is asymmetrical with respect to the Earth's magnetic dipole. For illustration, the geomagnetic parallel is denoted with a dashed line. The component of 100 kev does not have a constant intensity. The analysis of the signals from the third Sputnik in the vicinity of South America showed the existence of a region of higher intensity of

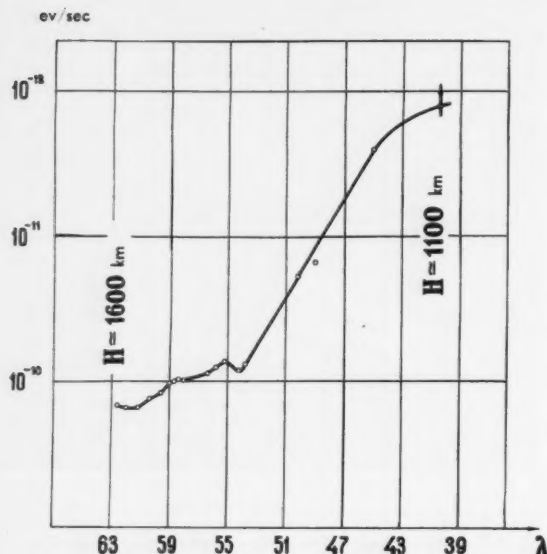


Fig. 8 Intensity of ionization in a scintillation counter as a function of a geomagnetic latitude and height above Earth's surface. The ordinate axis denotes energy in ev/sec deposited in a crystal of sodium iodide

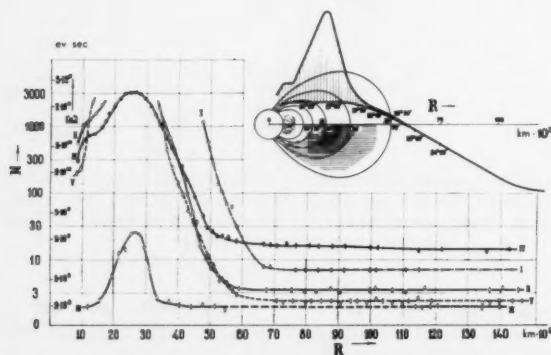


Fig. 9 Intensity of hard radiation as a function of distance from Earth during the flight of the first cosmic rocket. N—number of pulses registered by the counter; E—energy deposited in a crystal of sodium iodide. Roman numerals denote data: I, II and III—rate of counting with a threshold of 45 kev, 450 kev and 4.5 mev, respectively, with rate of counting referring to the area unit of the cross section of a crystal (19 cm²); IV—total ionization (total power delivered by a crystal per sec); V—readings of the Geiger counter. Number of impulses refers to the area unit of the cross section of counters (4 and 15 cm²). For great intensity, the data of a small counter are used. The position of the orbit of the first cosmic rocket with respect to radiation belts is shown schematically at upper right. Time corresponding to given points of the orbit is shown along the orbit. Distribution of the intensity of corpuscles at different distances from the Earth is shown schematically above the trajectory

ionizing particles above the Equator. The recorded particles in this region were harder than in the vicinity of polar regions.

Fig. 8 is a record obtained in the southern hemisphere in the range of heights from 1600 down to 1100 km. It is seen from the figure that, as the Sputnik moves toward the Equator, the intensity strongly increases although the height of the flight essentially decreases. The numerous analyses show that this equatorial zone of the higher intensity of cosmic rays extends up to 45 deg of geomagnetic latitude. Hard protons are, obviously, of importance here. In the material published, it was indicated that, no matter what the mechanism of forming the particles in the equatorial zone is, it is apparent that the factor of accumulation plays the main role in this effect. The concentration of particles in the equatorial zone, where they are able to oscillate at a great height above the Earth for a long time, presents convincing evidence.

The investigation of hard ionized particles showed the essential qualitative and quantitative difference between hard radiation near the equatorial zone and that of the polar zone. All these results were reported at the 5th meeting of CSAGI in Moscow in August 1958, and at the International Conference on Peaceful Use of Atomic Energy at Geneva in September 1958.

Further investigation of hard particles revealed the distribution of intensity of particles of different energy at various distances from the Earth in the vicinity of the moon. Fig. 9 shows the results obtained by the first cosmic rocket launched on Jan. 2, 1959. They enabled estimation of the type of energetic spectrum of electrons in the range of 20 to 100 kev. If the integral energetic spectrum of electrons is represented in the form

$$N(>E) \sim E^{-\gamma}$$

then $\gamma \sim 5$. The spectrum is notably harder ($\gamma \sim 3$) for the sections of smaller intensity at the outer edge of the zone. This points to an increase in the number of particles as the energy decreases. The maximum of intensity of the outer zone of the increased radiation was found to be $1\frac{1}{2}$ radii nearer to the Earth at the moment of exploration by the second cosmic rocket (Sept. 12, 1959) than by the first. By applying absorbers of different materials (lead and copper), the hard electron component was observed to contain in this zone a significant quantity of particles of energy greater than 0.5 mev.

It was thought before the launching of Sputniks that illumination, heating and ionization of the upper atmosphere are mainly due to the hard electromagnetic radiation of the sun. It was assumed only for the polar regions that the solar corpuscles (charged particles: Protons, α particles and electrons) may penetrate into the atmosphere while geomagnetic disturbances and aurorae are occurring. The study of the spectra of these aurorae showed that they are frequently caused by protons with a sizable range of speeds. However, no hydrogen emission was observed in many cases. Here again the aurorae were presumably explained by not very hard electrons of up to hundreds and thousands of electron volts penetrating into the atmosphere.

An attempt was made to discover these not very hard electrons by the third Sputnik. Two very thin fluorescent screens with aluminum foils of different thicknesses were used as indicators. The emission of the fluorescent screens was received by a photoelement. The photocurrent was then amplified. An electric signal was transmitted to a memory system and then, by radiotelemetry, transmitted to Earth. By using metal foils of different thickness it was possible to estimate both the intensity and the energy of the electrons that produced the greatest fluorescence on the screen. The peculiarity of the instrument was in its reaction practically only to electrons, without recording protons and photons of the same energies. As a result, powerful fluxes of electrons of about 10 kev were recorded at heights up to 1900 km over the South Pacific. The intensity of these fluxes was very high,

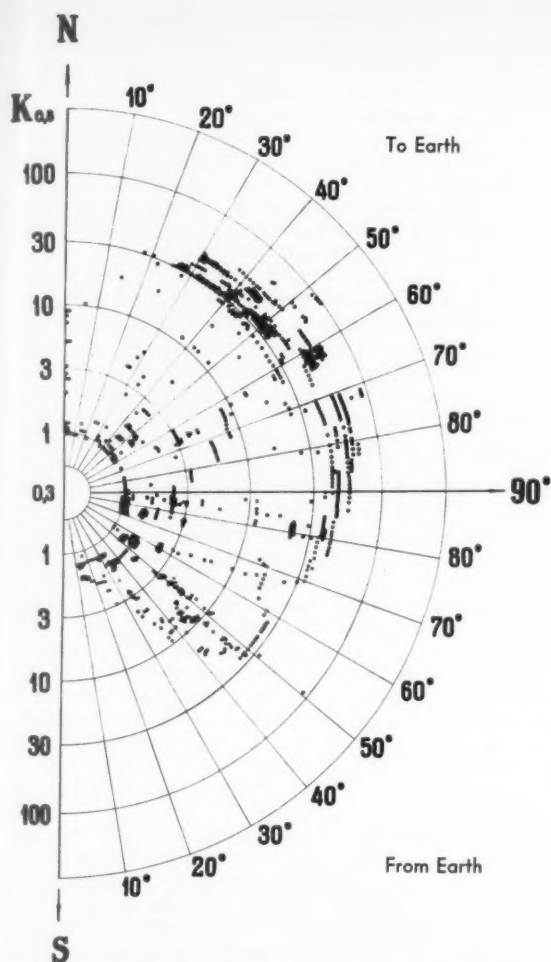


Fig. 10 Reading of the indicator of electrons with an aluminum foil $0.8 \times 10^{-3} \text{ gm cm}^{-2}$ as a function of an angle between the axis of the indicator and a magnetic field line. The scale of the indicator $K_{0.8}$ is proportional to the logarithm of the current of electrons

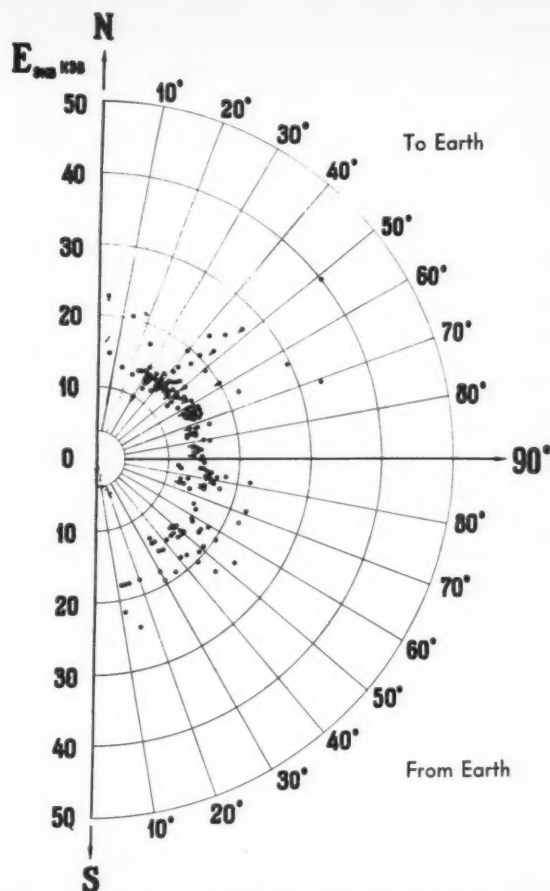


Fig. 11 Effective energy of electrons as a function of the angle between the indicator's axis and a magnetic field line, with data in this diagram corresponding to Fig. 10. The data represent the position of the Sputnik near the apogee within the range of height of 1720–1880 km. This section is divided into three intervals. The closed and open circles denote the consequent data, referring to these intervals. The symbol ! denotes off-scale values which actually can be a little greater

and in the majority of cases the instruments appeared to go off scale, since such high intensity was not expected. The effective energy of electrons changed during an experiment. The intensity of fluxes showed a tendency to decrease as the effective energy of the particles increased. The effective energy of electrons was observed to be less in the polar regions. The energy flux of the electrons studied exceeded $100 \text{ erg cm}^{-2} \text{ sec}^{-1}$ at the height up to 1900 km at the moment of going off scale. If the electron fluxes of the indicated intensity had penetrated into the lower layers of the atmosphere, i.e., the F region of the ionosphere, they could not have remained unnoticed, since they would essentially have increased ionization of the upper atmosphere and led to the appearance of aurorae. Since no such phenomena were observed, the recorded fluxes were explained to be electrons oscillating along the magnetic field lines (July 1958, Fifth Meeting of CSAGI).

Thus, information was obtained about the accumulation of electrons of about 10 keV at great heights up to 1900 km. All other explorations known to us refer to much lower altitudes and cannot be an indication of the existence of a magnetic trap around the Earth.

The majority of not very hard electrons move along the directions normal to the magnetic field lines. The electron flux is greater downward than upward. This can be seen in Fig. 10. In Fig. 11, the dependence of effective energy of the discovered electrons on the direction of the electron motion with respect to the magnetic field lines, is illustrated. Since the angle subtended by the indicators was $\frac{1}{4}$ steradian, the diagram shows that the opposite motion of electrons from the Earth near the magnetic field lines is practically absent. The electrons moving to the Earth were observed even under small angles to the magnetic field lines. This indicates that the particles penetrating to the lower layers of the atmosphere appear as a result of some processes at heights exceeding 1900 km. It has been found that the energy of electron fluxes able to reach the F layer of the ionosphere without reflection can reach values of about $1 \text{ erg cm}^{-2} \text{ sec}^{-1}$. Partial increases of intensity of corpuscles were registered above the Pacific even at -4° deg of geomagnetic latitude at the height of $\sim 1500 \text{ km}$, as was already reported in the material published.

It is no exaggeration to say that the powerful flux of the electrons discovered in the upper atmosphere is of extreme

importance in understanding many important processes, although it creates no threat for astronauts. It is of interest to note that sizable intensities of such electrons begin to appear at that geomagnetic latitude where, in the F region of the ionosphere, there had also been observed previously the increase of ionization but which could not be explained by the

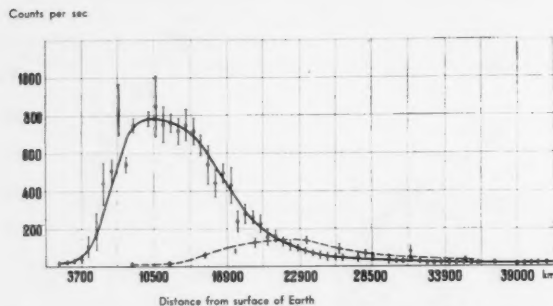


Fig. 12 Readings of the Cherenkov counter as a function of the distance from Earth's surface. Data denoted by a dashed line refer to the flight of the first cosmic rocket, and by the solid line to the second cosmic rocket. Scale of the ordinate axis is in angular units

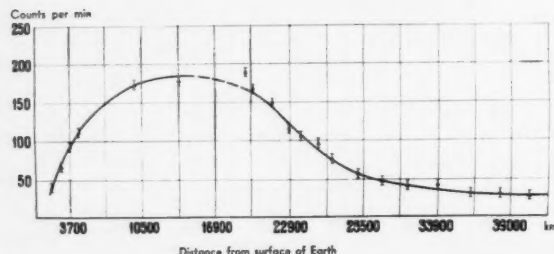


Fig. 13 Readings of nuclei with a charge equal to 2 or more as a function of distance from Earth. Scale along the ordinate axis is in relative units

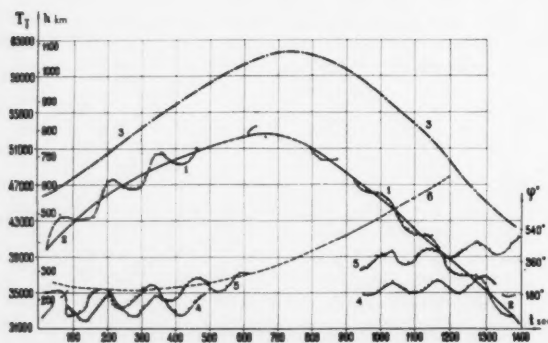


Fig. 14 Changes in intensity of the magnetic field during the third Sputnik's flight above the East Siberian world anomaly. Time in sec is measured along the abscissa axis; height and angle of the indicators' position along the ordinate axis. Numbers show the data referring to:

- 1 Field directly measured by the magnetometer above USSR territory.
- 2 Field measured by a magnetometer after elimination of the influence of the magnetic deviation caused by magnetic parts of the instrument.
- 3 Field at Earth's surface along the trajectory of the flight, taken from the magnetic map.
- 4 and 5 Readings of the orientation transmitters, showing a precession with a period of 136 sec and the rotation around the axis with a rate of 0.36 deg/sec.
- 6 Change of flight height.

effect of hard electromagnetic radiation of the sun. Some inhomogeneities in the ionization of the upper atmosphere and the system of ring currents around the Earth can be explained by the existence of such corpuscles. The dependence of the temperature variations and the density of the upper atmosphere upon solar activity becomes more understandable now, since the corpuscles, the intensity of which is governed by the solar activity, are the sources of heating. The heat flux brought by these electrons can well account for the increase of temperature with height and latitude, which could not be ascribed to the hard electromagnetic radiation of the sun alone.

The problem of great accumulation of hard particles in the upper atmosphere is now being widely discussed among geophysicists and astrophysicists, and there are different viewpoints on the problem.

Harder corpuscles discovered in the upper atmosphere are of no geophysical importance. They cannot essentially change the state of the upper atmosphere since their energy content is small. However, these hard corpuscles, as well as x-radiation arising in the Earth's atmosphere and in the body of rockets and Sputniks while they are irradiated by these electrons of energies of tens of kilo electron volts, are very unpleasant for astronauts, since the dose of dangerous radiation may reach tens of roentgens per hour. It is impossible to neglect this radiation, which requires that special measures be taken to defend cosmic travelers or photoemulsions in the apparatus. The investigations of hard radiation at great heights show that flight from the Earth of future astronauts will be less dangerous if the trajectory of the flight passes through the polar regions having the least concentration of hard particles. The best time for the flight from the Earth is, obviously, the time immediately after strong geomagnetic disturbances, after which the content of hard particles in the upper atmosphere greatly decreases.

The cosmic rockets carried Cherenkov counters of charged particles of a very great energy. The application of discriminators permitted registration of nuclei with charges greater than or equal to 2, 5 and 15. Apart from this, thanks to a photoeffect in the photomultiplier, x-rays of energy of tens and hundreds of kilo electron volts were registered. Since this radiation was mainly due to bombardment of the rocket bodies by hard electrons, then the registration of the sum photocurrent reflected the intensity of these particles. Figs. 12 and 13 show the results of these investigations. The intensity variation of x-radiation reflects the passage of indicators through the radiation belt around the Earth. In conformity with the experiments described in the foregoing, the maximum of the registered intensity during the flight of the second cosmic rocket was approximately $1\frac{1}{2}$ radii lower than in the flight of the first cosmic rocket. The fluxes of positive nuclei with charges greater than or equal to 2, 5 and 15, changed at great distances from the Earth, are in a ratio of 250:20:1, respectively. It is of interest that counting of nuclei with a charge equal to 2 or larger is of a greater value in the center of a radiation belt around the Earth. This circumstance is now being carefully studied. The existence of α particles in the radiative zone is supposed to be one of the possibilities.

The third Sputnik carried a magnetometer to investigate the Earth's magnetic field at great heights. This instrument determined the orientation of the Sputnik in the space around the Earth. Anomalies within the geomagnetic field were discovered by it. Many of them are of short duration and, obviously, are related to the ionospheric currents which cause magnetic disturbances. It is worth noting also that the character of height changes of intensity of abnormal and normal fields above the East Siberian world anomaly is the same, and this may be an indication of the fact that its sources are very deep. (See Fig. 14.) It allows one essentially to specify the known theories of a geomagnetic field and bring them into accord with the actual data.

It is of special interest to investigate the magnetic field of the Earth with the help of a magnetometer carried by the first and second cosmic rockets. Fig. 15 illustrates the expected change of the intensity of the magnetic field and its actual value during the flights of these rockets. So, for the first time, it was possible to register the magnetic field up to a distance of 60,000 km from the Earth, created by charged particles in the magnetic trap of the Earth. The result is in good agreement with the existence of not very hard electrons discovered around the Earth and described in the foregoing.

Attention should be drawn to the fact that the actual values of the magnetic field, given in Fig. 15, fluctuate. The deviations are much greater than those expected from the error in instruments. Thus, there are grounds to suspect that changes of intensity of the magnetic field near the Earth, estimated to be up to some tens and even a hundred of gammas, really exist. These fluctuations are being carefully studied. There are grounds to suppose that they are caused by short-period variations of the geomagnetic field, which were already thought by us to be exciters of the discovered corpuscles. Our attention is attracted by the closeness of the values of density of such a variable magnetic field and fluxes of electrons with an energy of about 10 kev at the moments of their maximum intensity. It is quite possible that these forms of magnetic and corpuscular energy are in balance or close to it.

To register micrometeors, the third Sputnik and the cosmic rockets carried piezoelectric elements. These elements registered the value proportional to impulse caused by a micrometeor's shock, which is, in turn, proportional to its energy. Table 1 gives information about the number of registered micrometeors and about the flux of matter brought by them into the atmosphere.

Exploration of the moon is most remarkable. It was established by the second cosmic rocket that the magnetic field close to the surface of the moon does not exceed 50-100 γ . The information about the magnetic field in the vicinity of the moon allows us to state that the effective magnetization of the moon is not higher than 5 per cent compared to the effective magnetization of the Earth. This is new and very important information for the conception of magnetism of cosmic bodies. We observed no inverse cube variations of the magnetic field near the moon. It is of interest to note, however, that fluctuations of the magnetic field similar to those discovered at the distance of some radii from the Earth have also been registered. Further investigations will reveal whether these fluctuations really exist and what characteristics they have. Moreover, if they reflect real values of the magnetic field, frozen into the interplanetary gas, then it is of great interest from the point of view of astrophysics, since it is the first direct indication of the interplanetary magnetic field. It has also been discovered that, within the error of

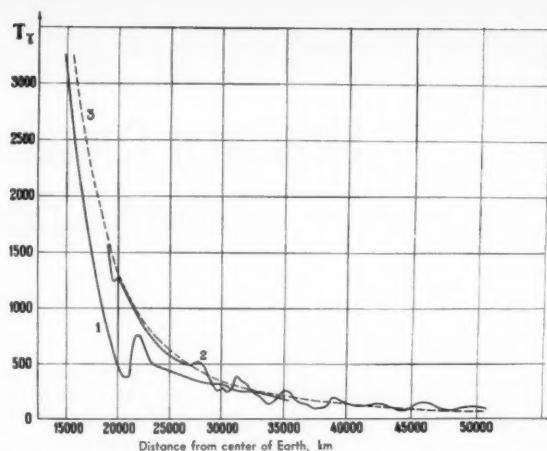


Fig. 15 Intensity of the magnetic field T as a function of the distance from the center of Earth. Curve 1 represents data obtained during the flight of the first cosmic rocket, curve 2 of the second cosmic rocket. Curve 3 shows the variation of the expected variation of magnetic field with distance, taking into account the dipole and quadrupole terms

measurements made close to the moon, there is no increase of intensity of hard corpuscular radiation as compared with that at the distance of some lunar radii. Cherenkov counters of hard charged particles also did not discover near the moon any deviations from that registered at a distance of several radii. The first photos of the unseen side of the moon have been obtained, and they will contribute to knowledge of the nature of this cosmic body.

As a result of the explorations described, our knowledge of the upper atmosphere and cosmic space have been greatly extended. New phenomena have been discovered and quantitative data obtained about those assumed before. A fascinating perspective of the exploration of the outer atmosphere and cosmic space at ever increasing heights, and of planets and their satellites by new and perfect means, now faces us. All this is a basis for new theoretical investigations.

A lively discussion is now taking place on the problems of physics of the upper atmosphere and cosmic space, and the not-too-distant future will give the answers to all these questions.

Table 1 Intensity of micrometeors

Means of exploration	Date	Mean approximate mass of registered micrometeors in gm, if $v = 4 \times 10^8$ cm sec ⁻¹	Intensity of a flux of micrometeors m ⁻² sec ⁻¹	Approximate mass of micrometeor matter in tons for the whole globe per 24 hr
Third Sputnik	May 15, 1957	2×10^{-8}	5 to 10	5 to 10×10^6
	May 16-17, 1957	$(8 \cdot 10^{-9} \text{ to } 30 \cdot 10^{-9})$	5×10^{-3}	5×10^3
	May 19-26, 1957		$< 10^{-4}$	$< 10^2$
First cosmic rocket		10^{-9}	$< 2 \times 10^{-4}$	$< 10^2$
Second cosmic rocket		10^{-9}	$\sim 2 \times 10^{-4}$	$\sim 10^2$
		$(2 \times 10^{-9} \text{ to } 20 \cdot 10^{-9})$		

Note: Material is treated partially.

Structural Considerations of Manned Space Vehicles

ANTHONY P. COPPA¹

General Electric Co.
Philadelphia, Pa.

This paper considers the structural requirements for a manned space vehicle. It gives approaches leading to an optimum vehicle considering the requirements of thermodynamics and human factors, in addition to structures. The necessity of early and thorough integration of these different requirements is emphasized. Several space vehicle configurations are presented including a ballistic and a glide type, in order to exemplify some of the various structural problems encountered in each type during the phases of spaceflight, entry into an atmosphere and landing. These include aerodynamic heating and loading, meteoroid impact and other problems. Materials and constructions suitable for optimum space structures are discussed sufficiently to demonstrate available choices and indicate areas of required development.

THE BOLD venture of manned flight into space presents sizable challenges in the conception and design of space vehicle structures. For the space vehicle must be for its occupants a world away from their natural world. It must provide a life-supporting atmosphere and protect them against meteoroid bombardment and the hazards of radiation; it must maintain comfortable cabin temperature levels in the presence of prolonged exposure to solar radiation; it must be a storehouse of food and water to nourish men, and of fuel to power machines; it must provide for the elimination of their waste products and for the expulsion of the large amounts of heat given off by electrical, electronic and mechanical components; it must provide an environment conducive to the maintenance of healthy mental and physical dispositions under otherwise unstimulating conditions. This means that for long duration flights there must be ample room for moving about, adequate noise suppression and reasonably comfortable furnishings. In addition, the space vehicle may well have to supply its own pseudogravitational field for the comfort and perhaps the safety of occupants during prolonged flights. Moreover in certain specific aspects, it must be more than our natural world, since it must survive the inferno of entry into planetary atmospheres while preventing the occupants from being baked to crisps! Finally, it must perform all of these functions having the minimum possible weight.

It is evident, therefore, that the consideration of space vehicle structures demands the compatible integration of many and varied technical disciplines. From the earliest stages of conception of the space vehicle, structural considerations, such as materials and construction operating under a wide range of temperatures, must be treated intimately with aerodynamic, thermodynamic, guidance, control and human factors considerations. For instance, a winged entry glide vehicle with sharp leading edges, although desirable from the viewpoint of aerodynamic efficiency, might be intolerable because of the enormous rate of aerodynamic heating over a sharp edge. Even though such a design were feasible from the thermodynamic consideration of available cooling schemes, it might not be feasible structurally because of

excessive thermal stresses and strains. Increasing the leading edge radius, however, though structurally feasible, might result in such intolerable aerodynamic losses, that a complete redesign of the basic shape might be required. Such an integrated approach is, of course, not a novel concept by any means. We are all familiar with the design caricatures which result when they are made from an isolated viewpoint. But the emphasis here is that this integration of disciplines must be considerably more intimate than in ordinary aircraft practice and timed sufficiently early to achieve optimum performance with minimum weight.

The problem of structural design of space vehicles, therefore, is more involved than merely formulating adequate structure on the basis of specified and uncoupled loading conditions; it is rather one part of an evolutionary process whereby the optimum vehicle design is attained through suitable tradeoffs with many and often widely different technical viewpoints.

In this paper some of the structural considerations of manned space flight such as atmospheric entry, heat protection schemes, meteoroid protection and landing will be discussed. Present state of the art and development needs will be indicated where pertinent.

Entry Into the Atmosphere

We first examine the entry phase of space vehicles into a planetary atmosphere, say the Earth's, since it is in this phase that the various disciplines of aerodynamics, thermodynamics, control and structures must be intimately bound together in order to achieve optimum design. The vehicle structural configurations meeting the requirements of the entry phase will then be considered in relation to the way they meet some of the other requirements stated previously.

Since we are concerned with manned vehicles we shall confine our attention to blunt nosed ballistic vehicles having low weight to drag ratios ($W/C_D A$) and glide vehicles having moderate lift to drag ratio (L/D), all of whose initial entry path angles are low. These conditions tend to minimize the severity of deceleration loading and aerodynamic heating.

In general a ballistic vehicle will experience higher levels of deceleration than a glide vehicle. Typical deceleration peaks attainable in manned ballistic and glide vehicles ($L/D \sim 1$) are $10g$ and $1g$ respectively without the aid of drag devices. These decelerations do not present difficult structural prob-

Presented at the ARS 13th Annual Meeting, New York, N. Y., Nov. 17-21, 1958.

¹ Specialist, Structural Systems, Aerosciences Laboratory, Missile and Space Vehicle Dept. Member ARS.

lems and are within the human tolerance limitations. A comparison of the heating rate histories of the various types of vehicles is given in Fig. 1. The heating rate curve corresponding to the pure ballistic type is for the stagnation point, since this represents the major heating problem for a blunt nosed vehicle. The curve given for the glide type (made available to the author by Flathers) corresponds to the side walls, since due to the very large proportion of side wall area to stagnation areas, this is representative of the major heating problem affecting the structure. The representative maximum heat flux of the ballistic type is considerably larger than that of the glide type, whereas the total heating time of the former is much smaller than that of the latter. The significance of this comparison is that blunt nosed ballistic vehicles must be designed to withstand relatively high rates of heat input with less total heat transferred to the cabin. Beryllium heat sink or ablation appear to be low weight solutions for handling the heat flux shown in Fig. 1. The glide types, on the other hand, must be designed to handle a relatively large total heat input, necessitating perhaps radiation-type cooling for the greater portions of the area. The stagnation regions like leading edges of wings, however, require protection schemes capable of handling much higher heat fluxes. For instance a 3-in. radius leading edge on the glide vehicle considered in Fig. 1 would have a heating rate approximately 10 times the peak side wall value for a substantially long time.

To facilitate discussion of some of the structural aspects of a ballistic-type entry vehicle, let us consider the hypothetical examples shown in Figs. 2 and 4. In both cases the vehicles are assumed to have a large radius blunt frontal surface called the heat shield. In Fig. 2 the shield considered is a heat sink type of beryllium. Beryllium, because of its relatively large heat capacity per unit weight and high strength, is outstanding as a heat sink despite its low ductility at room temperature and around 1200 F (1)² and the current problems of its toxicity and manufacturing of large one piece units. Since a heat sink sustains a high overall temperature and therefore undergoes a great deal of expansion, the manner in which it is mounted to the remaining structure is of considerable importance. A possible configuration (Fig. 2a) has the shield fastened to the supporting structure by means of a number of bolts which are free to move radially with the expanding shield. A layer of resilient material and insulation provides a distributed contact between the shield and supporting structure. Designing in this manner results in maximum support of the shield and minimizes thermal stresses.

To be an efficient heat sink for the heating history under discussion (\dot{q} max ~ 100 Btu/ft² sec, $t \sim 150$ sec), a material should have a high specific heat, a high melting temperature, a moderate thermal conductivity and not be structurally brittle. A comparison of the heat sink capabilities of several materials for equal weight is given in Fig. 3 (prepared from information made available to the author by Brunner). The temperatures shown with the various metals (except beryllium at 1200 F) are several hundred degrees below their melting points whereas that shown with graphite corresponds to its sublimation point. Hence, the relative potential of these materials as heat sinks for the heating history under discussion is indicated. Beryllium and graphite are the most efficient, whereas nickel, molybdenum and copper are relatively inferior at these lower heat fluxes. Beryllium³ at a temperature of 1200 F still retains its superiority over all other materials except graphite (6720 F).

Fig. 3 shows the relationship between the maximum heat flux (the peak re-entry flux) and the overall re-entry heating

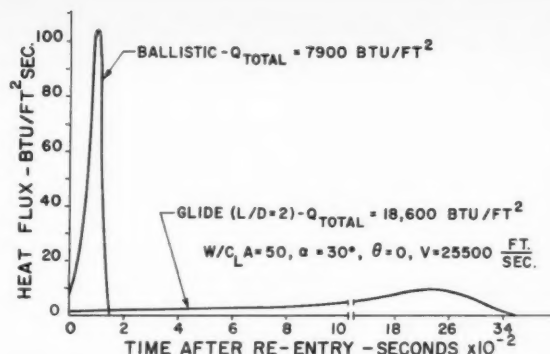


Fig. 1 Comparison of re-entry heating, ballistic vs. glide vehicle

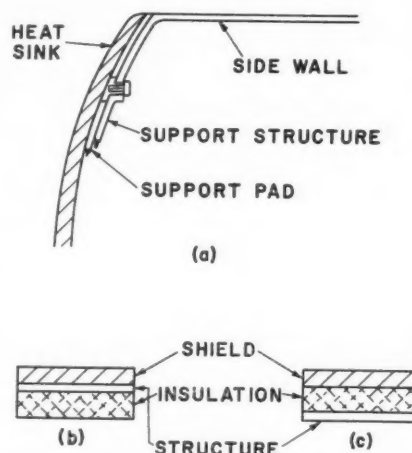


Fig. 2 Illustrative construction—passive heat sink

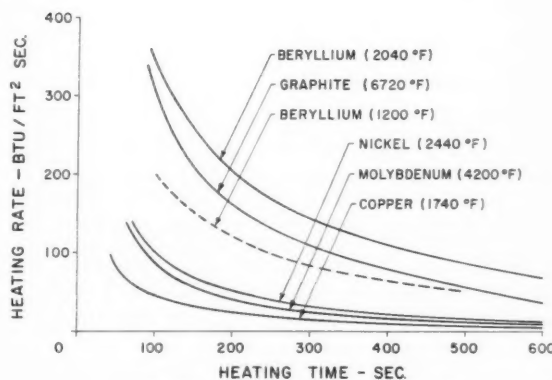


FIGURE 3 - COMPARISON OF HEAT SINK CAPABILITY OF SEVERAL MATERIALS HAVING THE SAME WEIGHT

Fig. 3 Comparison of heat sink capability of several materials

time which heat sinks of the specified materials can accommodate without the heated surface temperature exceeding the specified limitations. Fig. 3 applies to moderate weight heat sinks (~ 10 lb/ft³).

For the heating pulse under consideration (\dot{q} max ~ 100 Btu/ft² sec, $t \sim 150$ sec) the heat sinks shown in Fig. 3 are essentially finite slabs. Consequently, the temperature of the rear surface (opposite the heated surface) may assume intolerable levels considering the requirements of support

² Numbers in parentheses indicate References at end of paper.

³ At present there is some concern about the structural brittleness of beryllium above 1200 F. In this discussion graphite, also a brittle metal, has been assumed to be intimately attached to an adequate structure throughout its temperature range. Beryllium, for use at temperatures when it is brittle, can be considered in a like manner.

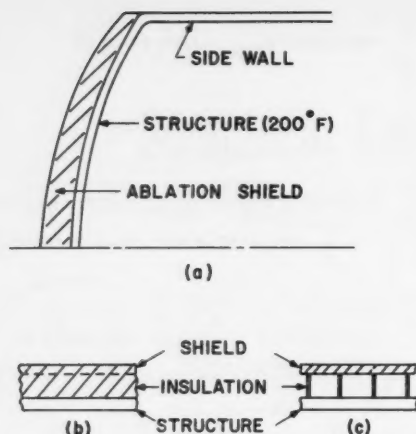


Fig. 4 Illustrative construction—ablation

structure and internal components. Therefore insulation will be required behind the heat shield. The selection of the insulation and the placement of it relative to the heat sink and support structure must be done on a system optimization basis. Placing the support structure next to the heat sink (Fig. 2b) will result in greater structural weight but makes possible the use of low density insulation for limiting internal compartment temperatures. On the other hand, placing insulation between the heat sink and the structure (Fig. 2c) will result in lower structural weight but higher insulation weight, since the insulation will have to transmit the re-entry decelerative loading from the heat sink to the support structure. Optimization of a heat sink system as the primary re-entry heat protection system for a drag decelerated, manned ballistic vehicle, therefore, lies in two basic considerations: Selection of the best heat sink material considering the heating history, and tradeoffs between structural temperature and insulation requirements.

In Fig. 4 is shown an ablation shield bonded to a low temperature structure. This type of shield serves both to remove some of the input heat by vaporization of the outer surface material and to insulate the internal structure against the remaining heat (Figs. 4a, b). A lighter shield construction would consist of a less than semi-infinite slab thickness ablating shield combined with an insulation layer of lower density than the insulating portion of the simple ablation shield. Such a configuration (Fig. 4c) offers substantial weight economies. However, since most of present low weight insulation materials possess low strength and since the insulation layer would have to support loading, suitable support of the insulation layer must be provided. Here also it is evident that for a given application an optimum weight

can be achieved by considering various materials at appropriate temperatures for the internal structure together with the corresponding insulation required. In the ablation type, however, since it is desirable to have a bond or an intimate support between the ablation layer and the insulation or main structure, it is important to select materials for the main structure which avoid thermal expansion incompatibilities between it and the ablation layer. A bond is considered necessary in the case of a continuous (nonsegmented) ablation shield because most of the efficient ablating materials are highly brittle and are not safe for primary load bearing functions. Table 1 (contributed by Abbate) shows some of these low fracture strains. At present, adhesive bonds are available for operation up to 500 F for short times. Some techniques utilizing a combination adhesive-mechanical bond are being developed for bond operation up to 1000-1200 F. For operation at bond temperatures of 2000 F which might be present at the inner face of a thin graphite ablation shield, suitable bonds are nonexistent at the present time.

In the absence of an adequate bonding technique for high bond temperatures or in the event that a continuous brittle shield, even though suitably supported, has excessive stresses, a shield composed of lateral segments (tiles) can be used to advantage, since the segments, if small enough and not too thick, can be relieved of the major thermal and load stresses. This also permits the use of a less rigid understructure, since cracking of the shield due to deformation of the understructure could not occur in the segmented shield. The individual segments can be attached to the main structure by minimum restraint mechanical fastening. The presence of many breaks in the shield surface due to the clearance between the segments, however, can produce turbulence and excessive heating in the region of the edges and corners of segments causing severe erosion. This deterioration of the surface contour with the attendant increasing turbulence and heating can be intolerable. This might be alleviated by making exposed edges blunt rather than sharp or by filling the clearance with a suitable material.

As previously stated, a glide entry vehicle is exposed over its major area to a smaller heating rate and a much larger total heat input than a ballistic entry vehicle to perform the same mission. A heat sink is undesirable for this type of heating because of the large heat capacity required (and hence excessive weight), whereas the heating rate is generally too small for effective ablation-type shielding. Radiation cooling, on the other hand is ideal for use here since with the low heat flux the equilibrium temperatures in the presence of high emissivities are within the operating temperatures of available materials and most of the incoming heat is radiated away from the structure. A plot of the heat fluxes which can be radiated from a surface vs. surface temperatures is given in Fig. 5 for several emissivities. Indicated also are materials suitable for radiation surfaces.

Shown in Fig. 6 is a cross section of a possible radiation cooled structure for the fuselage or cabin area. The outer-

Table 1 Ablation shield materials

Material	Tensile ultimate, psi $\times 10^{-3}$	Elastic modulus, psi $\times 10^{-4}$	Fracture strain, per cent	Density, lb/in. ³	Coeff. of thermal expansion, in./in. deg F $\times 10^6$
phenolic nylon	4.80	0.45	1.15	0.044	...
phenolic "leached" glass	4.90	2.30	0.25	0.058	...
quartz	7.10	10.0	0.07	0.079	0.30
graphite	2.00	1.50	0.13	0.080	1.40
Teflon polymer*	2.80	0.10	5.00	0.080	5.50
Duroid	2.80	0.072	...

*E. I. Du Pont de Nemours and Co.

most layer is the reradiating surface whose outer and inner surfaces would have a high and low emissivity, respectively. Beneath this is a layer of insulation, primarily for shielding against heat transferred from the inner surface of the radiating layer. Beneath this is the main load bearing structure followed by a layer of insulation. Since, as is evident from Fig. 5, the temperature of the radiating layer is quite high whereas that of the inner structure is considerably lower, a great deal of differential thermal expansion is to be expected, especially in fully circular structures like internally pressurized cabins. Restraining the hot outer shell against thermal expansion may cause it to buckle if it is sufficiently ductile or fracture if is brittle. Buckling can result in excessive aerodynamic losses or heating. This problem may be reduced to within tolerable limits by restraining the outer shell by means of closely spaced supports. This produces small uniform buckles having low amplitude over the surface. A freely expanding outer shell on the other hand may buckle under the aerodynamic pressures or be subject to flutter. The solution of this problem appears to lie in some of the following approaches:

1 Minimize differential expansion by selecting low expansion materials for the hotter structure and high expansion materials for the cooler structure, and by adjusting the heat transferred into the inner structure in accordance with the maximum tolerable differential thermal expansion (progressive stepdown of temperature).

2 Spread out a thermal buckling tendency by attaching the hot shell by means of closely spaced cellular supports, thereby reducing aerodynamic losses and excessive heating.

3 Allow unrestrained expansion of the hot shell only when it is capable of withstanding the loads applied to it.

4 Segment the hot shell, if no other solution is adequate.

In order to examine some of the heating problems corresponding to a radiation cooled structure in more detail, let us consider Fig. 7 (prepared from information made available to the author by Castelli). This shows the heating of the side walls of a vehicle experiencing the ballistic heat flux shown in Fig. 1, followed by a relatively long and gradual drag chute descent through the atmosphere (total time 1600 sec). Two radiation wall constructions are shown, configurations A and B. These are identical except that A has an effective emissivity factor $F_e = 0$ on the interior surfaces, whereas B has a corresponding effective value of $F_e = 0.20$. It is seen that the outer wall in each case responds quickly to the heat flux. The inner wall of A rises very slowly to a peak of 240 F, but the inner wall of B rises rapidly to a peak of 1000 F and only gradually decreases. In each case the temperature of the inner wall actually exceeds that of the outer wall for the greater portion of the descent. Thus a reversal of the thermal stresses of the outer and inner walls takes place, the outer and inner walls initially being in compression and tension, respectively, and then for the greater time reversed. The smaller temperature differences between the inner and outer walls of configuration B during the heating time make B appear more favorable than A with respect to maximum thermal stresses in the walls. On the other hand the temperature of the inner surface of the insulation layer (considered perfectly insulated at the surface) in configuration B (500 F peak) makes B inferior to A with respect to maintaining comfortable cabin temperatures. The foregoing example illustrates the necessity of minimizing the flow of heat into the interior of a relatively long time entry vehicle. It shows that for effective radiation cooling: (a) Very low interior surface emissivities must be maintained between the walls for substantially long times, (b) efficient radiant heat insulation is needed in the event that surface emissivities cannot be maintained due to oxidation, etc., or are not producible, and (c) conduction paths between outer and inner walls must be minimized.

This example serves also to illustrate basically some of the heating problems of a glide vehicle such as indicated in Fig. 1.

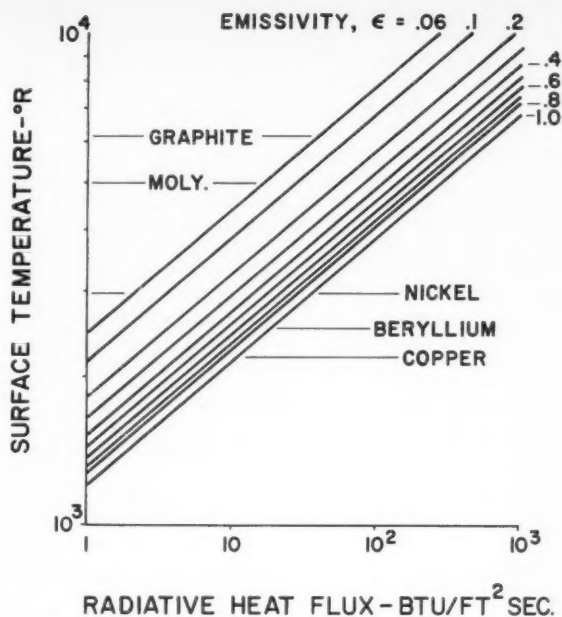
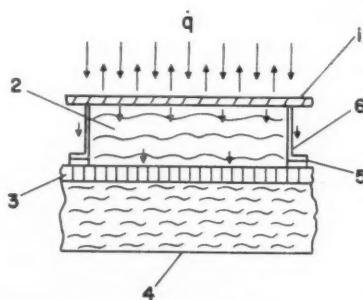


Fig. 5 Surface temperature vs. radiative heat flux



- 1 - RERADIATION WALL
- 2 - INSULATION (RADIANT HEAT)
- 3 - STRUCTURE
- 4 - CABIN INSULATION
- 5 - INSULATOR
- 6 - STIFFENER - ATTACHMENT

Fig. 6 Illustrative construction—radiation cooling

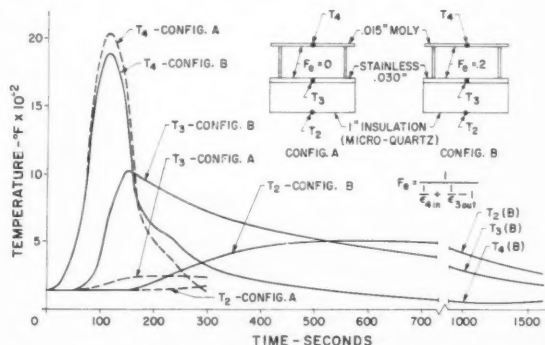


Fig. 7 Heating of a radiation cooled structure during re-entry heating, structural temperature vs. re-entry time

In order to minimize thermal stresses arising in mutually attached inner and outer walls having widely different temperatures, a wide variety of materials must be considered. In doing so, thermal incompatibilities can be minimized. Especially in the presence of the temperature reversal effect demonstrated in Fig. 7, such an approach will be required. A selection of materials suitable for the walls of, say a radiation cooled vehicle, can be made using the information in Figs. 8 and 9. In Fig. 8 it can be seen that for operation at the high outer surface temperature, materials like molybdenum and graphite can be used. Their low ratio of strength to density, however, renders them unattractive for use as main load bearing structures. For such use beryllium, inconel X and titanium among other materials appear quite attractive for temperatures around 1000 F. Fig. 9 shows that, fortunately, materials necessary for the high tempera-

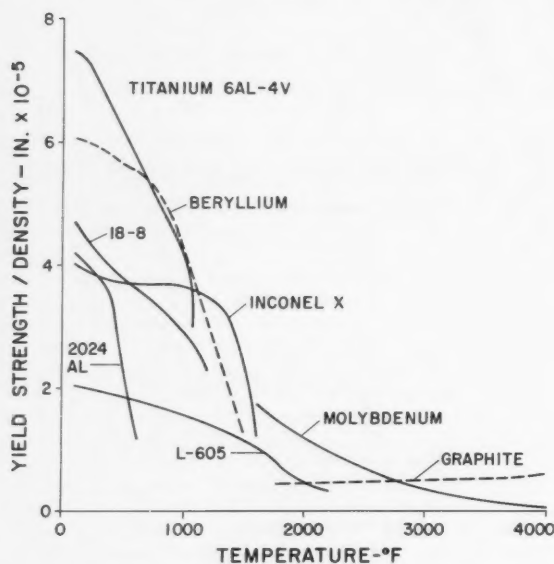


Fig. 8 Strength to density ratio vs. temperature for several re-entry vehicle materials

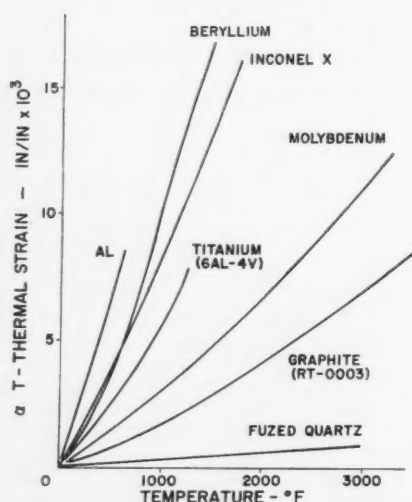


Fig. 9 Comparison of thermal expansions for several re-entry vehicle materials

ture use have low thermal expansion. This seems characteristic of many other high temperature materials like ceramics, quartz and tantalum. On the other hand, intermediate temperature materials such as beryllium, 18-8 stainless, titanium and inconel X have higher thermal expansions. Finally, low temperature materials like aluminum and magnesium have the highest thermal expansions of all. This suggests that by using the right material for the hot and cooler walls it might be possible to limit thermal stresses to allowable values. In Fig. 10 are shown the thermal stresses occurring in several double wall constructions utilizing graphite (0.125-in. thickness) as the hot wall. Aluminum, titanium and 17-7 PH steel serve as the inner wall. The thickness of the inner wall for each material was determined from the same bending buckling requirement and found to be 0.029, 0.042 and 0.036 in., respectively. Graphite was chosen in order to study the use of a brittle material under conditions of high thermal expansion. The graphite was assumed to be at a constant temperature of 2240 F, and the temperature of the inner wall was varied. The walls were assumed to be restrained by each other. For each combination a temperature is reached at which no thermal stresses exist in either wall. These are 400 F for aluminum, 780 F for 17-7 PH and 830 F for titanium. Below these temperatures the graphite is in compression, and the inner wall in tension. Above them, the situation is reversed. Considering that graphite breaks at 9500 and 2600 psi in compression and tension, respectively, it is seen that graphite would not be overstressed provided the aluminum wall did not exceed 550 F and the titanium and 17-7 PH did not exceed 1000 F. The stresses

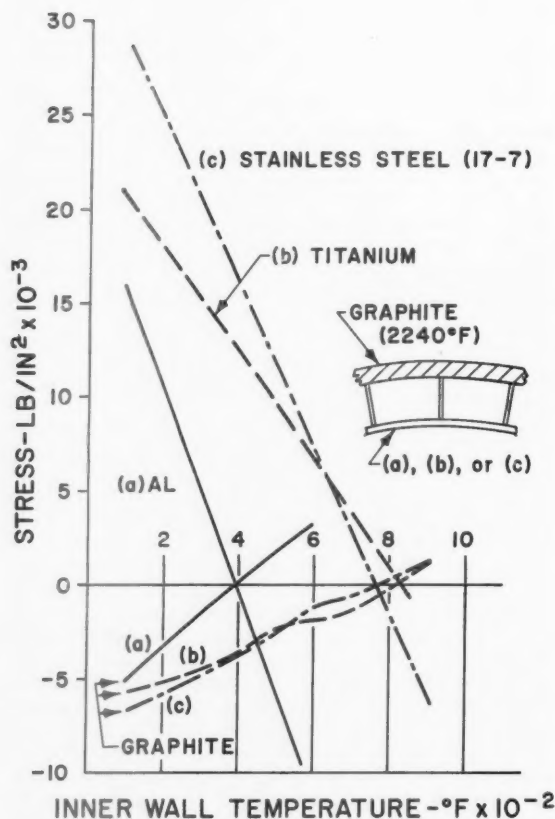


Fig. 10 Thermal stresses in several double wall structures consisting of a hot outer wall and a cooler inner wall whose temperature varies

induced in the inner walls are quite low, although buckling might be a design consideration at the higher temperatures when they are under compression.

The development and testing of materials and necessary protective coatings for operation at very high temperatures is being conducted on an accelerated basis. Manufacturing techniques of welding, brazing, diffusion bonding and flame spraying of ceramics, to mention only a few, are being developed to permit fabrication of these materials for use at these required high temperatures.

Meteoroid Impact

Recent investigations of meteoroid bombardment of space vehicles have led to quantitative estimates of the structural material required to reduce the probability of penetration of the vehicle wall to within conservative design limits. In Fig. 11, derived from (3), is presented the estimated thicknesses of various structural materials required for reasonably safe design for a vehicle having an external surface area of 100 ft². It is evident that materials with a high elastic modulus are the most effective meteoroid shields for a given thickness. For a given weight, however, a material like beryllium will be greatly superior to stainless steel and molybdenum, because of its superior ratio of elastic modulus to density.

Possible wall constructions for protection against meteoroids are shown in Fig. 12. Fig. 12a (from an idea attributed to Whipple) shows a multilayered construction in which the outer layer or layers, which provide the major heat protection, also provide the meteoroid protection. The inner layer is the main structural shell which also serves as the pressurized cabin wall. If the outer layer were punctured by a meteoroid, the resultant fragment should impinge on the inner wall over a wider area than that of the original puncture. This should make penetration of the inner wall unlikely.

The apparently high efficiency of beryllium as a meteoroid shield suggests the use of thin sheets or foils of beryllium placed between the heat shield and the pressurized cabin wall (Fig. 12b) whenever the heat shield is inadequate for meteoroid protection. Such sheets could also help protect the inner structure from heat radiated from the heat shield.

In any event, schemes for automatically detecting and sealing a penetration once it occurs should be perfected. This is emphasized by the fact that for a ratio of the volume of pressurized cabin to the area of the punctured hole equal to 10,000, atmospheric pressure is reduced to 3.0 psi within 30 sec, and that the time limit of human operation at such low pressures is about 15 sec (6).

In addition, the pressurized cabin shell should be constructed of materials which have high resistance to catastrophic bursting in the presence of a crack or hole. A comparison of the bursting resistance of several structural alloys is given in Fig. 13 from (4).

Landing Phase

Recovery of the vehicle may be accomplished by means of a drag chute or retrorocket decelerated landing on land and water for ballistic entry types, and more or less conventional type of landing on land or water for glide vehicles. The latter could also employ drag devices or retrorockets to assist in landing. Ballistic vehicles will experience high impact loadings, particularly in the case of ground impact. The shocks transmitted to the occupants can possibly be reduced by designing a sufficient length of collapsible shell structure forward of the occupant mounting point. Such design should allow for: (a) Cushioning the occupant against the very short time prebuckling elastic shocks, (b) limiting relatively long time deceleration force applied to the human body during collapse of the frontal structure to within the human shock tolerances, and (c) maintaining the supine

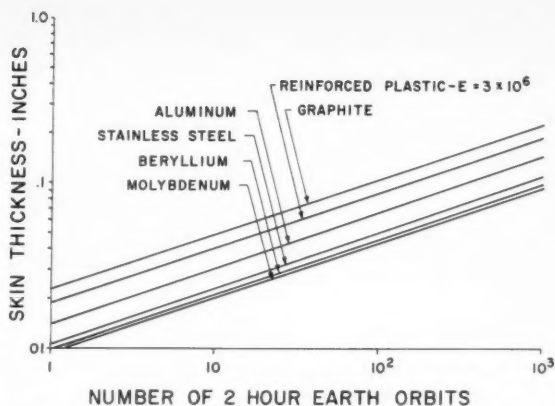


Fig. 11 Required wall thickness of several materials for meteoroid protection

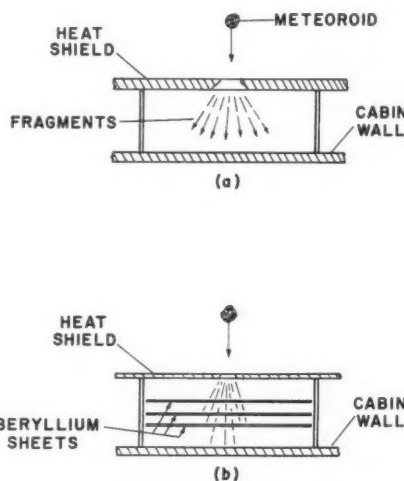


Fig. 12 Meteoroid bumpers

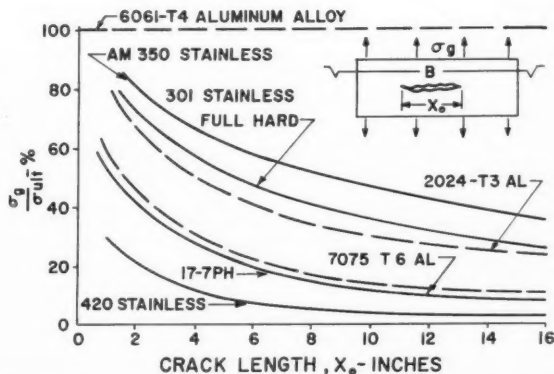


Fig. 13 Tear resistance of various sheet materials for wide panels

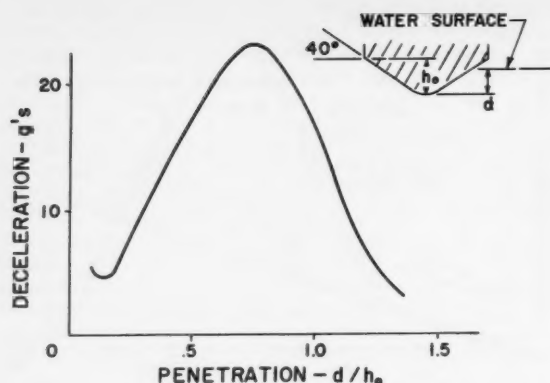


Fig. 14 Rigid body impact decelerations of a blunt nosed vehicle during water entry

body attitude and the broad distribution of forces of the body during the full deceleration interval. Recovery of the vehicle on water, on the other hand, precludes structural failure which would cause leakage of water into the cabin. Fortunately, the deceleration forces associated with moderate impact velocities on water can be kept within human tolerances without structural collapse by proper design of the vehicle frontal shape.

The landing of glide-type vehicles presents structural problems similar to the landing of present-day high performance fighter aircraft, except that landing velocities and attack angles may be higher.

We now consider briefly the recovery of a representative low weight to drag ballistic vehicle in water. By means of a drag chute or other drag devices, the flight velocity of the vehicle can be reduced sufficiently to permit safe landing on water. In Fig. 14, the rigid body decelerations of a blunt nosed vehicle impacting vertically on water with an initial velocity of 50 fps are plotted vs. the penetration depth ratio, d/h_0 . The deceleration pulse rises to a peak value of 23 g and falls below 5 g in a total elapsed time slightly greater than 0.1 sec. In addition, the rate of increase of deceleration to the peak value of 23 g is less than 800 g per sec. Medical authorities believe that the measure of severity of shock loading on human beings is the combination of the peak g and the rate of rise to the peak. The maximum ability to withstand shock loading depends on proper body support and orientation to

the loading. The best positioning of the body is supine with the maximum distribution of deceleration forces over the rear portions of the body. Shock tests with human subjects so supported indicate that a rate of rise of 1000 g per sec to a peak of 30 g is tolerable whereas a rate of 1500 g per sec to a peak of 40 g results in unconsciousness (5). Thus the decelerations shown in Fig. 14 are within the safe human tolerance.

Both the peak and the rate of rise of deceleration during water entry are very dependent on the frontal shape of the vehicle. In general, for a given vehicle mass, velocity and cross-sectional diameter, the greater the flatness of the frontal surface the higher is the decelerative peak and rate of rise. Human shock tolerances, therefore, can easily be exceeded if sufficient attention is not given to the frontal shape for the water entry condition.

The foregoing discussion does not consider the effect of surface waves or of a lateral velocity component such as might result from lateral drift or swinging of the drag chute-vehicle system. These factors, of course, must be considered in accordance with expected overall water entry conditions.

Acknowledgment

Grateful acknowledgment is given to members of the following groups at the Missile and Space Vehicle Department, General Electric Co. who contributed to this paper: Thermodynamics Engineering Operation for information and calculations relating to aerodynamic heating and heat transfer, Stress Analysis Engineering Operation for information on materials and for calculations and preparation of figures; Aerosciences Laboratory for information on materials and meteoroid protection.

References

- 1 O'Rourke, R. G., Hurd, J. N., Wickle, K. G. and Beaver, W. W., "Mechanical Properties of Reactor Grade Beryllium at Elevated Temperatures," Brush Beryllium Co. Rep., Aug. 1956, pp. 102, 103.
- 2 Preston, J. B., Row, W. P. and Kattus, J. R., "Determination of the Mechanical Properties of Aircraft-Structural Materials at Very High Temperatures After Rapid Heating," WADC Technical Rep. 57-649, Part 1, Nov. 1957.
- 3 Kornhauser, M., "Estimates of the Penetration of the Skin of a Satellite by Meteoroids," Missile and Space Vehicle Dept. Rep., General Electric Co., April 1958.
- 4 Melcon, M. A., "A Survey of the Structural Properties of Some High Strength Sheet Steels," AGARD Rep. no. 101, April 1957, pp. 5, 6, 22.
- 5 Stapp, J. P., Col. USAF (MC), "Effects of Mechanical Force on Living Tissues," *J. Aviation Medicine*, vol. 26, no. 4, Aug. 1955, pp. 281-287.
- 6 Konecni, E. B., "Decompression Events in Bio-Satellites," ARS Preprint 638-58, 1958.

Midcourse Guidance Problem in Satellite Interception¹—I

ANGELO J. SKALAFURIS²
DONALD H. SCHILLER³

Caywood-Schiller, Associates
Chicago, Ill.

This paper is concerned with the problem of midcourse guidance as applied to a vehicle attempting to contact an Earth satellite. For expository purposes and simplicity of computation, two-dimensional geometry and circular target orbits only are considered. Equations are developed yielding the required velocity corrections necessary for interception as a function of the rocket's present position and velocity, relative to the target. Velocity corrections for different types of interception, e.g., minimum landing power, minimum midcourse power, are considered. A brief numerical computation is included for illustrative purposes.

Midcourse Guidance

THE MAJOR problem of celestial navigation is the selection of an orbit which will intersect a given target orbit in space-time. In the case of present Earth satellites and for heavier Earth satellites of the near future, propulsion and technology limitations and/or mission requirements may dictate that near-circular satellite orbits be employed. Whether for purposes of satellite destruction or for the transfer of material to space stations, there will be a desire to rendezvous with these circularly orbiting satellites.

A typical planned interception may be divided into four stages: The initial or launch guidance stage; information stage, i.e., determination of post-launch phase-space coordinates of satellite and intercepting rocket; calculation and employment of midcourse propulsive corrections; and the terminal guidance maneuvers.

It is the function of midcourse guidance to place the intercepting vehicle in close proximity to the satellite at some future time so that the terminal guidance measures may be applied. That midcourse corrections will be needed can be safely predicted, not only due to launch errors, but due to effects of those physical space phenomena known to exist, but whose magnitudes have not as yet been accurately measured.

Concerning the information stage, we note that the problems associated with satellite tracking and the attainable accuracies have been discussed elsewhere (1).⁴ It is well known (2) that the determination of the satellite's position at three distinct times (assuming good accuracy) is sufficient to yield the position and velocity of the satellite at the mean observation time, and hence, by Newtonian mechanics, its entire future path is known. As a starting point we shall assume that such phase-space coordinates can be determined by a suitable data gathering system.

In actuality, the Newton-Kepler problem does not apply with complete accuracy to Earth satellite orbits. For precision the orbital perturbations due to atmospheric drag, oblateness of the Earth, the sun and moon force fields, etc.,

should be included. These corrections are also discussed in (2). Midcourse guidance as defined here, however, does not require inclusion of this level of precision.

The particular guidance scheme which should be used for midcourse guidance will depend upon the type of propulsive system being employed by the rocket, i.e., whether of the sustained or impulsive type. Moreover, the appropriate mathematical expansions and formulas will depend upon the magnitude of the anticipated corrections. We shall assume in this study that impulsive corrections are to be determined for the interception of an Earth satellite by a rocket vehicle. The satellite is moving in a circular orbit, and the rocket's present orbital course is co-planar and only slightly in error. The orbital corrections may then be assumed small in magnitude.

Terrestrial or Single Central Force Guidance Problem

In the terrestrial problem, the equation of path is the common conic section

$$r = \frac{a(1 - e^2)}{1 + e \cos(\theta - \theta_0)} \quad [1]$$

(provided the energy of the vehicle is nonzero, for then the path is parabolic).

The Newtonian differential equations of motion for a planetoid in a two-dimensional central force field require three constants of motion to be specified for a unique determination of the path. Two are required for the radial motion, and only one determines the angular momentum, a constant of the motion for the system.

The problem of midcourse guidance is solved when there are given the required changes in two orthogonal components of velocity such that the new trajectory will be a desired one. These changes in velocity are affected by a change of the constants of motion (determined from initial conditions), and since there are three such constants, two are chosen arbitrarily and the third is expressed in terms of these two. This choice now serves as a set of generalized coordinates from which the velocity changes are to be computed.

Conversely, any given point in phase space must determine these orbital parameters, and in the case of the conic section [1] the measured coordinates at any phase-space point in

Received March 16, 1959.

¹ The investigation upon which this research is based was sponsored by the Weapons Guidance Laboratory, Wright Air Development Center, under Air Force contract no. AF33(616)-3415.

² Operations Analyst.

³ Partner. Member ARS.

⁴ Numbers in parentheses indicate References at end of paper.

transit will yield the constants of the motion via (3)

$$\epsilon^2 = 1 - \frac{rV^2}{\mu} \left(2 - \frac{rV^2}{\mu} \right) \sin^2 \psi \quad [2]$$

$$a = \mu r / (2\mu - rV^2) \quad [3]$$

$$\theta_0 = \theta - \cos^{-1} \frac{(rV^2/\mu) \sin^2 \psi - 1}{\sqrt{1 - (rV^2/\mu)[2 - (rV^2/\mu)] \sin^2 \psi}} \quad [4]$$

Here r , θ , V are the rocket's radial and angular positions and its velocity, respectively, ψ is the "heading," which is determined from the ratio of transverse to radial velocities by the equation

$$\tan \psi = V_\theta / V_r$$

and μ is the Earth's gravitational constant.

The time required for a rocket in this central force field, to travel from its present radial position r to the satellite's radius r_m is given by

$$t = \frac{a^{3/2}}{\sqrt{\mu}} \left[\sin^{-1} \left(\frac{r' - a}{a\epsilon} \right) - \epsilon \sqrt{1 - \left(\frac{r' - a}{a\epsilon} \right)^2} \right]_{r'=r}^{r'=r_m} \quad [5]$$

(provided r_m is in the domain of r'). The following is a sketch of the derivation of Equation [5]. It is noted that

$$dt = ds/V$$

V is evaluated from the energy equation

$$V^2 = (2\mu/r) - (\mu/a)$$

The differential arc length can be written

$$ds = \sqrt{1 + r^2(d\theta/dr)^2} dr$$

From the equation of path it follows that

$$\frac{d\theta}{dr} = \frac{a(1 - \epsilon^2)}{r^2 \epsilon \sin(\theta - \theta_0)}$$

Eliminating angular coordinates reveals that

$$r^2 \left(\frac{d\theta}{dr} \right)^2 = \frac{a^2(1 - \epsilon^2)}{a^2\epsilon^2 - (r - a)^2}$$

The subsequent substitution yields

$$dt = \left\{ \frac{ar^2}{\mu[a^2\epsilon^2 - (r - a)^2]} \right\}^{1/2} dr$$

from which formula [5] follows by direct integration.

If the corresponding time for the satellite to travel an angular distance from its present position ϕ to some ϕ_m is subtracted from the foregoing, a time difference is obtained which becomes a useful quantity when the satellite's final angular position ϕ_m is required to coincide with the rocket's, i.e., $\phi_m = \theta_m$.

The angle F can be written in terms of the previous relations as

$$F = \left\{ \frac{a^{3/2}\omega}{\sqrt{\mu}} \left[\sin^{-1} \left(\frac{r' - a}{a\epsilon} \right) - \epsilon \sqrt{1 - \left(\frac{r' - a}{a\epsilon} \right)^2} \right] - \cos^{-1} \left[\frac{1 - \epsilon^2}{\epsilon} \frac{a}{r'} - \frac{1}{\epsilon} \right] \right\}_{r'=r}^{r'=r_m} - (\theta - \phi) \quad [6]$$

$(\theta - \phi)$ is the present angle observed at the Earth, between the rocket and the satellite. In order for a space-time intersection to occur between these two objects, the angle F must vanish. Thus F represents the angular difference in position of the satellite and rocket, that will result should the rocket be allowed to continue on its present orbit out to satellite radius.

If F does not vanish, guidance is required, and the problem becomes one of determining what variation in the generalized coordinates a and ϵ will result in the vanishing of F .

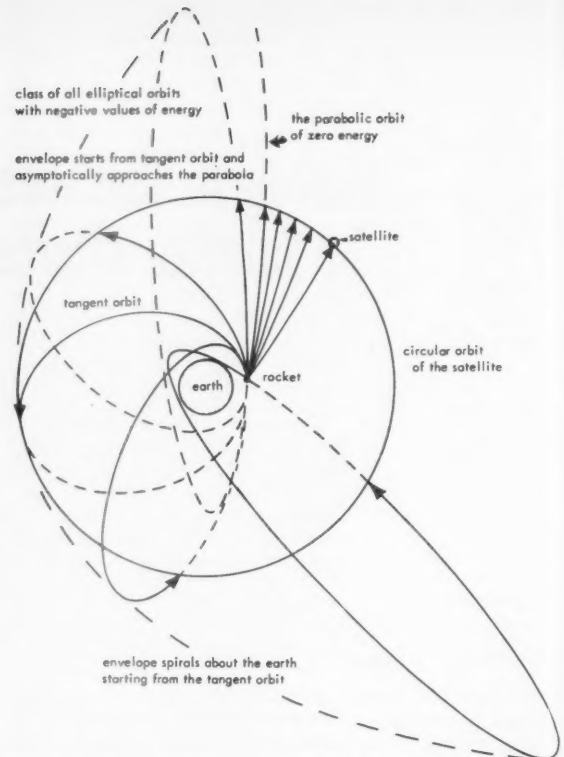


Fig. 1 Graphical illustration of the space-time restraining trajectories

The variation will take place in a system with two degrees of freedom; hence the constraint imposed by $F = 0$ will be satisfied by a number of trajectories (Fig. 1). An additional constraint yielding a unique solution to the problem may be imposed. In particular, two alternatives based on power requirements are considered here.

Tangential Interception

This alternative is accomplished by that orbit whose apogee is tangent to the satellite's orbit at the point of interception. This may be a desirable constraint because the time spent in the vicinity of the satellite is maximized. Moreover, at apogee it would be possible to impart a final velocity thrust which would superimpose the rocket vehicle's orbit on that of the satellite and the two vehicles would circle the Earth in permanent juxtaposition. This final thrust would always be needed because the rocket's velocity at apogee is not equal to the satellite's velocity. Such a maneuver may be preferable to nontangential interception followed by an attempt to change orbits, for in the latter case the velocity component perpendicular to the satellite's orbit would have to be extinguished.

The requirement that the trajectory's apogee be tangent to the satellite's orbit may be expressed by the following equation

$$G = r_m - a(1 + \epsilon) = 0 \quad [7]$$

Presumably G will not be zero, and it is a measure of how far the turning point P of the orbit has missed tangency with the satellite. In theory then, Equations [6] and [7] can be solved for a and ϵ , requiring F and G to be zero. With these values of a and ϵ the required velocity components can be

calculated by means of the following equations

$$V_\theta^2 = \frac{\mu}{a} \left(\frac{a}{r} \right)^2 (1 - \epsilon^2)$$

$$V_r^2 = \frac{\mu}{a} \left[\left(\frac{a\epsilon}{r} \right)^2 - \left(1 - \frac{a}{r} \right)^2 \right]$$

Now, under the assumption of small corrections

$$F(a + da, \epsilon + d\epsilon) \doteq F(a, \epsilon) + \frac{\partial F}{\partial a} da + \frac{\partial F}{\partial \epsilon} d\epsilon = 0$$

similarly for $G(a + da, \epsilon + d\epsilon)$. We compute the corrections $da, d\epsilon$ which will make F and G zero from the equations

$$-F = \frac{\partial F}{\partial a} da + \frac{\partial F}{\partial \epsilon} d\epsilon$$

$$-G = \frac{\partial G}{\partial a} da + \frac{\partial G}{\partial \epsilon} d\epsilon$$

Solving

$$da = \frac{(\partial F / \partial \epsilon)G - (\partial G / \partial \epsilon)F}{(\partial F / \partial a)(\partial G / \partial \epsilon) - (\partial F / \partial \epsilon)(\partial G / \partial a)}$$

$$d\epsilon = \frac{(\partial G / \partial a)F - (\partial F / \partial a)G}{(\partial F / \partial a)(\partial G / \partial \epsilon) - (\partial F / \partial \epsilon)(\partial G / \partial a)}$$

These formulas are true in general. The partial derivatives are easily computed for the F and G given, and they are collected at the end of this section on the terrestrial or single central force guidance problem. (They have not been substituted here, for they appear to reveal no new physical consequences.)

The corresponding incremental velocity changes are

$$dV_r = \frac{\mu}{2aV_r} \left\{ \left[1 - \frac{a^2}{r^2} (1 - \epsilon^2) \right] \frac{da}{a} + 2\epsilon \left(\frac{a}{r} \right)^2 d\epsilon \right\}$$

$$dV_\theta = \frac{V_\theta}{2} \left(\frac{da}{a} - \frac{2\epsilon}{1 - \epsilon^2} d\epsilon \right)$$

Minimum Midcourse Guidance Power

This alternative is accomplished by choosing the impacting orbit requiring the minimum expenditure of fuel during midcourse correction.

A similar minimization problem is well known in the literature. This problem has been formulated in the following manner.

Given the phase-space coordinates of two points in a gravitational field, and the equation for the burning rate of the fuel, what course is to be followed between these two points such that minimum fuel is expended? Mathematically, this is a problem in the calculus of variations in which two points in phase-space are given, and the relative minimization of the integral for fuel consumption over all co-terminal curves is considered. This solution merely will give the path in which a minimum amount of work is done against the fields, with most of the work going into changing the kinetic energy of the rocket. This important problem is distinct from the problem that is being considered here; namely, if the rocket is off course, what revised orbit shall be taken at that point which will evolve successfully to the satellite intercept and how shall the alterations be brought about with a minimum expenditure of fuel?

This minimal condition must be a scalar, for ultimately it is the change in mass of the fuel which is to be minimized. The potential energy of the fuel, be it chemical or nuclear, is proportional to its mass, and any change in the mass of the fuel must reflect itself in an equivalent change in kinetic energy of the rocket. The momentum given to the field can be neglected for impulses of small time durations.

The change in kinetic energy of the rocket is given by

$$dK = 2\mathbf{V} \cdot d\mathbf{V} + dV \cdot dV$$

First-order terms are not sufficient as a measure of this change, for a maneuver consisting of

$$V_\theta dV_\theta = -V_r dV_r$$

would cause the first-order term to vanish; however, this would not be a measure of the power used in the transition. On the other hand, the complete expression cannot be the correct one either, for in the case of a mere rotation of the velocity vector, power is expended, but the energy of the initial and final states is the same; moreover, the complete expression would be a measure which is velocity dependent.

An attractive scalar to minimize is one that measures only the power expended in the transition, and is not proportional to the velocity

$$dk = d\mathbf{V} \cdot d\mathbf{V}$$

$$dk = \left[\left(\frac{\partial V_r}{\partial a} \right)^2 + \left(\frac{\partial V_\theta}{\partial a} \right)^2 \right] da^2 + 2 \left[\frac{\partial V_r}{\partial a} \frac{\partial V_r}{\partial \epsilon} + \frac{\partial V_\theta}{\partial a} \frac{\partial V_\theta}{\partial \epsilon} \right] da d\epsilon + \left[\left(\frac{\partial V_r}{\partial \epsilon} \right)^2 + \left(\frac{\partial V_\theta}{\partial \epsilon} \right)^2 \right] d\epsilon^2$$

This quantity is to be minimized subject to the constraint of space-time intersection, i.e.

$$F(a, \epsilon, da, d\epsilon) = 0$$

Consistent with the previous assumption, Taylor's theorem is used to the first order to measure F

$$F(a, \epsilon, da, d\epsilon) \doteq F(a, \epsilon) + \frac{\partial F}{\partial a} da + \frac{\partial F}{\partial \epsilon} d\epsilon$$

Here a and ϵ are given parameters computed from the present phase-space coordinates, and the variable quantities da and $d\epsilon$ are to be chosen on the basis of the two foregoing conditions.

By the method of Lagrange multipliers m must be eliminated from the three equations (following), and then the independent variables da and $d\epsilon$ must be obtained.

$$2 \left[\left(\frac{\partial V_r}{\partial a} \right)^2 + \left(\frac{\partial V_\theta}{\partial a} \right)^2 \right] da + 2 \left[\frac{\partial V_r}{\partial a} \frac{\partial V_r}{\partial \epsilon} + \frac{\partial V_\theta}{\partial a} \frac{\partial V_\theta}{\partial \epsilon} \right] d\epsilon + m \frac{\partial F}{\partial a} = 0$$

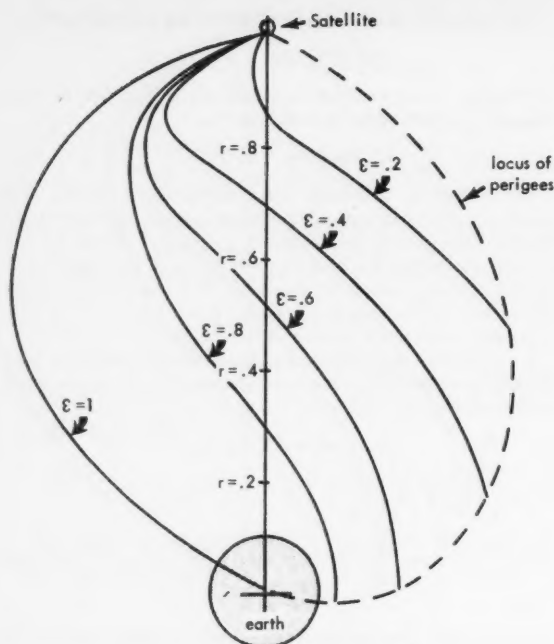
$$2 \left[\left(\frac{\partial V_r}{\partial \epsilon} \right)^2 + \left(\frac{\partial V_\theta}{\partial \epsilon} \right)^2 \right] d\epsilon + 2 \left[\frac{\partial V_r}{\partial a} \frac{\partial V_r}{\partial \epsilon} + \frac{\partial V_\theta}{\partial a} \frac{\partial V_\theta}{\partial \epsilon} \right] da + m \frac{\partial F}{\partial \epsilon} = 0$$

$$F + \frac{\partial F}{\partial a} da + \frac{\partial F}{\partial \epsilon} d\epsilon = 0$$

The solutions are

$$da = -\frac{F}{\Delta} \left\{ \frac{\partial F}{\partial \epsilon} \left[\frac{\partial V_r}{\partial a} \frac{\partial V_r}{\partial \epsilon} + \frac{\partial V_\theta}{\partial a} \frac{\partial V_\theta}{\partial \epsilon} \right] - \frac{\partial F}{\partial a} \left[\left(\frac{\partial V_r}{\partial \epsilon} \right)^2 + \left(\frac{\partial V_\theta}{\partial \epsilon} \right)^2 \right] \right\}$$

$$d\epsilon = \frac{F}{\Delta} \left\{ \frac{\partial F}{\partial a} \left[\frac{\partial V_r}{\partial a} \frac{\partial V_r}{\partial \epsilon} + \frac{\partial V_\theta}{\partial a} \frac{\partial V_\theta}{\partial \epsilon} \right] - \frac{\partial F}{\partial \epsilon} \left[\left(\frac{\partial V_r}{\partial a} \right)^2 + \left(\frac{\partial V_\theta}{\partial a} \right)^2 \right] \right\}$$



Angles are measured in degrees.
Distances are in satellite radius units.

Fig. 2 Required eccentricities for trajectories which contact the satellite at the apogee

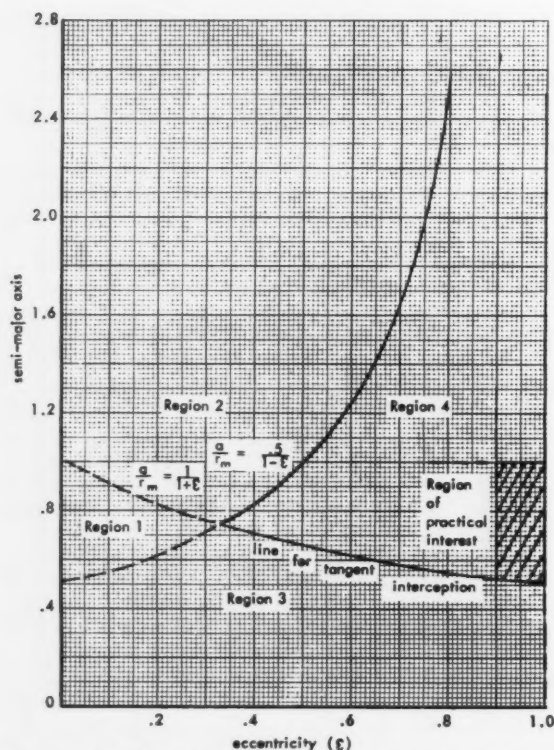


Fig. 3 Navigation plot of the guidance parameters for the range $r/r_m = 0.5$

Region 1—maximum range is too short, and range never assumes $r/r_m = 0.5$; region 2—maximum range is sufficient, but range never assumes $r/r_m = 0.5$; region 3—maximum range is too short, but range does assume $r/r_m = 0.5$; region 4—maximum range is sufficient, and range does assume $r/r_m = 0.5$

where

$$\Delta = \left(\frac{\partial F}{\partial \epsilon} \right)^2 \left[\left(\frac{\partial V_r}{\partial a} \right)^2 + \left(\frac{\partial V_\theta}{\partial a} \right)^2 \right] - 2 \frac{\partial F}{\partial a} \frac{\partial F}{\partial \epsilon} \times \left[\frac{\partial V_r}{\partial a} \frac{\partial V_r}{\partial \epsilon} + \frac{\partial V_\theta}{\partial a} \frac{\partial V_\theta}{\partial \epsilon} \right] + \left(\frac{\partial F}{\partial a} \right)^2 \left[\left(\frac{\partial V_r}{\partial \epsilon} \right)^2 + \left(\frac{\partial V_\theta}{\partial \epsilon} \right)^2 \right]$$

The differential changes da and $d\epsilon$ vanish when F vanishes. Physically this is not only to be expected but lends support to postulate that $dV \cdot dV$ is an appropriate quantity to be minimized. If the complete change in kinetic energy were taken as the minimal condition, it would contain terms linear in da and $d\epsilon$, and thus nonzero values of da and $d\epsilon$ would appear when F is zero, i.e., even when the principal constraint of space-time intersection is met a maneuver would be called for. This is an absurdity since only the nonvanishing of F should dictate the execution of the maneuver.

The partial derivatives required for explicit determination of the velocity changes are

$$\frac{\partial F}{\partial a} = \frac{3\omega}{2} \sqrt{\frac{a}{\mu}} \left[\sin^{-1} \left(\frac{r-a}{a\epsilon} \right) - \epsilon \sqrt{1 - \left(\frac{r-a}{a\epsilon} \right)^2} \right] - \frac{a^{3/2}\omega}{\sqrt{\mu}} \left[\frac{r^2}{a^2\epsilon\sqrt{1 - [(r-a)/a\epsilon]^2}} \right] + \frac{\sqrt{1 - \epsilon^2}}{a\epsilon\sqrt{1 - [(r-a)/a\epsilon]^2}}$$

$$\frac{\partial F}{\partial \epsilon} = \frac{r - a(1 + \epsilon^2)}{a\epsilon^2\sqrt{1 - \epsilon^2}\sqrt{1 - [(r-a)/a\epsilon]^2}} - \frac{a^{3/2}\omega}{\sqrt{\mu}} \left[\frac{r - a(1 - \epsilon^2)}{a\epsilon^2\sqrt{1 - [(r-a)/a\epsilon]^2}} \right]$$

$$\frac{\partial G}{\partial a} = -(\epsilon + 1)$$

$$\frac{\partial G}{\partial \epsilon} = -a$$

$$\frac{\partial V_r}{\partial a} = \frac{\mu}{2V_r a^2} \left[1 - \frac{a^2}{r^2} (1 - \epsilon^2) \right]$$

$$\frac{\partial V_r}{\partial \epsilon} = \frac{\mu \epsilon}{a V_r} \left(\frac{a}{r} \right)^2$$

$$\frac{\partial V_\theta}{\partial a} = \frac{V_\theta}{2a}$$

$$\frac{\partial V_\theta}{\partial \epsilon} = -\frac{\epsilon V_\theta}{1 - \epsilon^2}$$

Numerical Example of Satellite Interception

This section displays sample impacting trajectories and a semi-analytic, or graphical solution to the midcourse guidance problem as applied to the space vehicle in a single force field. It is assumed here that the satellite orbits the Earth in a circular path. If the vehicle is to intersect the satellite in space-time, it has been shown to be necessary for a and ϵ to satisfy the relation

$$\phi - \theta = \left\{ \cos^{-1} \left[\frac{a(1 - \epsilon^2) - r}{\epsilon r} \right] + \left(\frac{a}{r_m} \right)^{3/2} \left[\epsilon \sqrt{1 - \left(\frac{r-a}{a\epsilon} \right)^2} - \sin^{-1} \left(\frac{r-a}{a\epsilon} \right) \right] \right\}_{r/r_m} \quad [8]$$

This expression is obtained from 6 when all distances are normalized by the satellite's radius r_m and the satellite's angular velocity $\sqrt{\mu/r_m}$ is taken as the unit of angular velocity.

A convenient coordinate system here is one with an origin at the Earth's center and the x axis through the satellite,

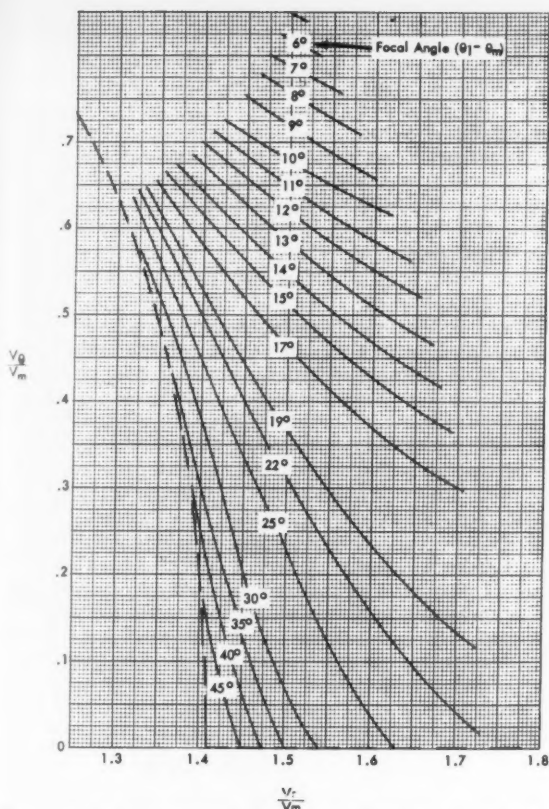


Fig. 4 Velocity component contours as a function of focal angle for satellite interception when $r/r_m = 0.5$

so that the system rotates with the angular velocity of the satellite. The polar coordinates of a particle in this system are then $(\phi - \theta, r_1/r_m)$. Trajectories of different eccentricities which contact the satellite at their apogees are shown in this coordinate space in Fig. 2. The trajectories are relative to the Earth satellite axis and depict how the rocket positions would appear to an observer on Earth who faced the satellite at all times.

The set of conditions

$$0 \leq \epsilon \leq 1$$

$$a \geq \frac{r_m}{1 + \epsilon}$$

$$a \leq \frac{r}{1 - \epsilon}$$

..... [9]

describe a region in (a, ϵ) space within which these trajectory parameters must lie in order to intercept the satellite. This region is a function of the distance to the vehicle and is shown in Fig. 3 for $r/r_m = 0.5$. Within this region the (a, ϵ) combinations of practical interest are those in the shaded subregion which correspond to ellipses of high eccentricity; those not wasteful of power.

Now at any point $(\phi - \theta, r/r_m)$ in space, all values (a, ϵ) obtained from Equation [8] and satisfying conditions [9] will allow space-time intersection with the satellite. Since the variables under control of the vehicle are the velocity components, it is desirable to transfer the consideration to

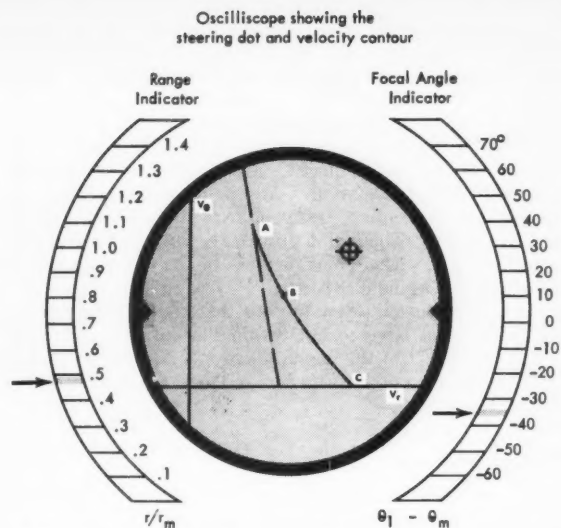


Fig. 5 Instrument layout for presenting the guidance information

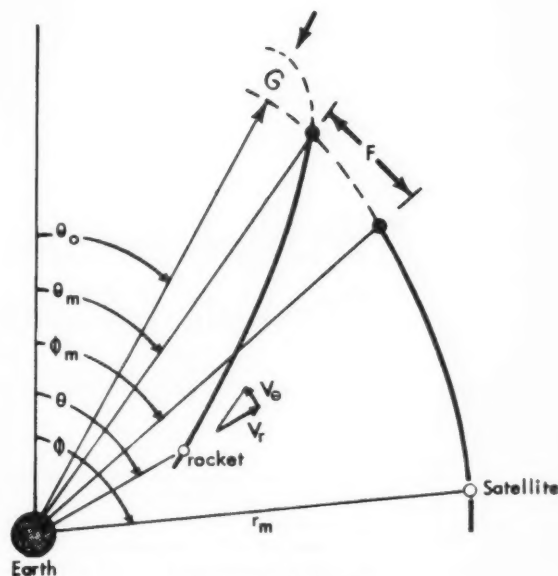


Fig. 6 Angle analysis

velocity coordinates by means of the equations

$$\left(\frac{V_\theta}{V_m}\right)^2 = \frac{r_m a}{r^2} (1 - \epsilon^2)$$

$$\left(\frac{V_r}{V_m}\right)^2 = \frac{r_m a}{r^2} \epsilon^2 \left[1 - \left(\frac{r - a}{a\epsilon}\right)^2\right]$$

..... [10]

where V_m is satellite velocity.

The dashed envelope in Fig. 4 represents the inner region of Fig. 3 as plotted in V_r, V_θ space, at $r/r_m = 0.5$.

For any angle $(\theta - \phi)$ measured at this range, the terminal point of the velocity vector must lie upon the appropriate contour if satellite interception is to be accomplished. If it does not, sufficient rocket power must be applied to bring the velocity vector to the required contour.

A further example of the guidance technique is displayed in Fig. 5. Here the single velocity contour, ABC (as a function of the measured range and angle) is continually generated and can be presented on the face of a scope. The measured velocity is also presented as a steering dot. If the missile is on a proper trajectory, the dot should remain on the contour throughout the flight. If it is off, the dot must be "steered" onto the contour. Any point on the contour will provide an interception; two points are of particular interest:

1 Point A: This point provides a tangent interception.

2 Point B: This point, nearest to the dot, requires the least midcourse guidance power.

It is of further interest to note that the steering dot initially does not have to fall within the outlined region. A point to the left of the region merely means that the rocket will not reach satellite's radius without the application of additional power.

Nomenclature

r_m	= radial distance between the Earth and the satellite
r	= present radial position of the rocket
θ	= present angular position of the rocket
θ_m	= angular position of the rocket when its radial position is r_m
ϕ	= present angular position of the satellite

ϕ_m	= angular position of the satellite when the radial position of the rocket has reached r_m
ω	= angular velocity of the satellite when circular motion is assumed
a, e, θ_0	= semimajor axis, eccentricity, and angular orientation of the elliptic conic section
F	= focal angle between the rocket and the satellite measured at the Earth, when the radial position of the rocket has reached the value r_m
G	= distance from the turning point P of the orbit to the trajectory of the satellite measured from the Earth along a common radius
P	= turning point or maximal point of the orbit from the Earth
V_r	= radial component of the velocity of the rocket
V_θ	= transverse component of the velocity of the rocket
V	= speed of the rocket
μ	= gravitational constant of the Earth
ψ	= arc tangent of the quotient of V_r to V_θ ; see Fig. 6

References

- 1 Van Allen, J. et al., "The Scientific Use of Earth Satellites," University of Michigan Press, Ann Arbor, 1956, pp. 23-43.
- 2 Kooy, J. M. J., "On the Application of the Method of Variation of Elliptic Orbit Elements in Case of a Satellite Vehicle," *Astronautica Acta*, vol. III/Fasc. 3, 1957, p. 179.
- 3 Whittaker, E. T., "A Treatise on the Analytical Dynamics of Particles and Rigid Bodies," Dover Publications, Inc., New York 1944, p. 87.

Missile Orientation Errors in Command Guidance Systems

KENNETH C. MATHEWS¹

Sylvania Electronic Products, Inc.
Waltham, Mass.

Some types of command guidance systems utilize tracker data plus the missile roll autopilot control equation to compute missile angular orientation at the command point. In these systems tracker errors, autopilot transient errors and angles-of-attack result in incorrect command transmission and a consequent performance degradation. An analysis is made of command errors and performance degradation resulting from tracker errors and angles-of-attack in two types of command guidance systems employing the roll autopilot control equation for orientation computations. It is shown that much smaller command errors are expected to occur in a system in which the roll autopilot keeps the time integral of roll rate equal to zero, than in a system in which the roll autopilot maintains perpendicularity between one wing plane and a fixed inertial reference plane.

IN ALL guidance systems it is necessary to maintain knowledge of missile angular orientation. In a command guidance system, maintaining this knowledge at the command point poses a special problem because of the inability of tracking devices to measure orientation of a remote missile (1).² Some degree of cooperation from the missile is necessary, and this may be achieved in a variety of ways. One method, which is sometimes necessary but substantially increases missile cost and complexity, makes use of a complete missile-borne inertial reference capable of transforming received commands phrased in inertial coordinates into missile pitch

and yaw commands. Another method, which lessens the burden on missile-borne components and which in some cases functions satisfactorily, employs the properties of the roll autopilot control equation to deduce (at the command point) missile orientation. Commands transmitted to the missile can then be phrased directly in pitch and yaw terms. Unfortunately, missile orientation cannot be deduced with perfect accuracy by this method and a degree of guidance degradation is introduced.

Command errors and guidance degradation in command guidance systems employing two types of roll autopilot control equations are analyzed below. These two types of autopilot control are designated bank stabilization and roll stabilization, respectively. The bank stabilization roll

Received Feb. 12, 1959.

¹ Engineering Specialist.

² Numbers in parentheses indicate References at end of paper.

autopilot maintains perpendicularity between one wing plane and an inertia-fixed reference plane. (In some applications this is called the belly-down or one-wing-vertical system.) The roll stabilization roll autopilot keeps the time integral of roll rate equal to zero. Typical equipment configurations (2,3) for both types of attitude control are shown schematically in Fig. 1. For convenience, consideration has been restricted to a cruciform missile configuration.

The manner in which missile orientation is deduced at the command point is common to both bank and roll stabilization systems. In essence, missile orientation is completely defined by three angles, ψ , θ and ϕ , or azimuth, elevation and bank respectively, regardless of whether these appear explicitly in guidance computations. Further explanatory material can be found in the following section. Approximations to azimuth and elevation of the missile longitudinal axis are obtained from tracker measurements by assuming that the missile longitudinal axis is colinear with the flight path tangent. Bank angle ϕ is either assumed to be zero in the bank stabilized system or is computed from Equation [1] in the roll stabilized system

$$\phi = \int_{\psi_1}^{\psi_2} \sin \theta d\psi \quad [1]$$

The direction cosines of the missile pitch and yaw axes with respect to an inertia-fixed coordinate system are trigonometric functions of ψ , θ and ϕ . Errors in command point computation of these direction cosines result in incorrect pitch and yaw command transmission with a consequent guidance degradation. Errors appear initially in ψ and θ , because angle-of-attack invalidates the assumption of colinearity of missile longitudinal axis and flight path tangent; furthermore, tracker measurements are not perfect and the roll autopilot is subject to transient errors.

It is shown in the following sections that the effects of angle-of-attack and tracker inaccuracy in the bank stabilized system differ materially from those in the roll stabilized system. (Angle of attack, or sideslip, and an error in measurement of direction of the flight path tangent have identical effects upon command errors.) Specifically, the roll stabilized system is much less affected by angle-of-attack and tracker inaccuracy than the bank stabilized system.

Coordinate Geometry

With reference to Fig. 2, the set of mutually orthogonal unit vectors $\bar{X}_0, \bar{Y}_0, \bar{Z}_0$ is fixed in inertial space. The relative orientation of a second mutually orthogonal set of unit vectors $\bar{x}, \bar{y}, \bar{z}$ fixed to the missile body, is given in terms of the Euler angles ψ , θ and ϕ (azimuth, elevation and bank angles respectively). A seventh vector \bar{N} is defined by Equation [2], and is therefore a unit vector colinear with the node line

$$\bar{N} = (\bar{Z}_0 \times \bar{x}) \sec \theta \quad [2]$$

The directions of \bar{x}, \bar{N} and \bar{Z}_0 are frequently called Euler axes and correspond to the rotation axes of a three-axis gimbal system. In Fig. 2, an $\bar{X}_0 - \bar{Y}_0$ inertial reference plane is shown as a horizontal plane; however, all following statements and derivations apply irrespective of $\bar{X}_0 - \bar{Y}_0$ plane orientation, providing the relative orientation between $\bar{x}, \bar{y}, \bar{z}$ and $\bar{X}_0, \bar{Y}_0, \bar{Z}_0$ is as shown.

Any vector \bar{u} can be expressed as the vector sum of inertial, missile body or Euler axis components. That is

$$\begin{aligned} \bar{u} &= u_{10}\bar{X}_0 + u_{20}\bar{Y}_0 + u_{30}\bar{Z}_0 & (\text{inertial}) \\ \bar{u} &= u_{1b}\bar{x} + u_{2b}\bar{y} + u_{3b}\bar{z} & (\text{body}) \\ \bar{u} &= u_{1e}\bar{x} + u_{2e}\bar{N} + u_{3e}\bar{Z}_0 & (\text{Euler}) \end{aligned} \quad [3]$$

It follows that the instantaneous missile angular velocity can be expressed in either of two ways as the vector sum of angu-

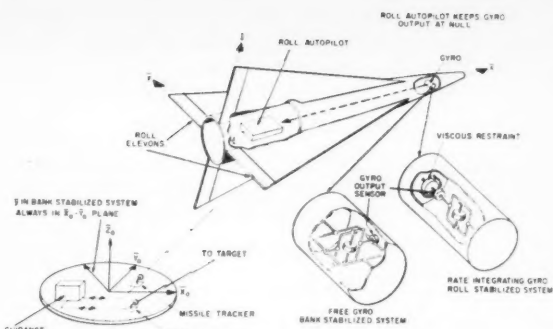


Fig. 1 Bank and roll stabilized command guidance systems

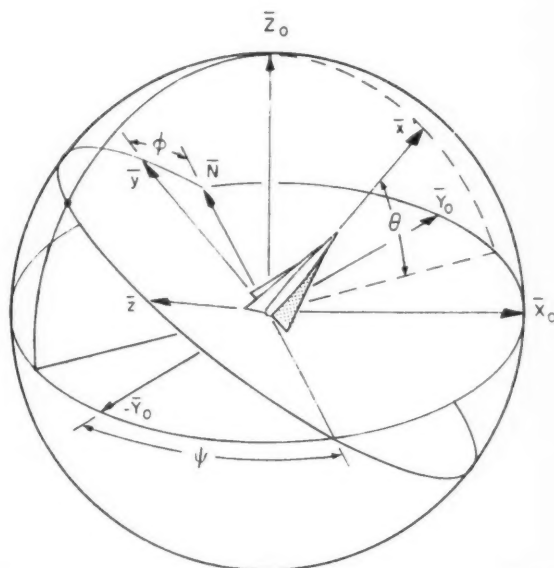


Fig. 2 Coordinate geometry. As shown ψ and ϕ are positive, θ is negative

lar rates. That is

$$\bar{\omega} = \dot{\phi}\bar{x} + \dot{\theta}\bar{N} + \dot{\psi}\bar{Z}_0 = p\bar{x} + q\bar{y} + r\bar{z} \quad [4]$$

where $\bar{\omega}$ is the instantaneous vector angular velocity and p, q, r are the missile angular velocity components along \bar{x}, \bar{y} and \bar{z} respectively. Specifically, p is roll rate and it can be shown that

$$p = \dot{\phi} - (\sin \theta)\dot{\psi} \quad [5]$$

In the roll stabilized case

$$\int p dt = 0$$

so that, in this case

$$\phi_2 - \phi_1 = \int_{\psi_1}^{\psi_2} \sin \theta d\psi \quad [6]$$

Command Errors

In both the bank and roll stabilized systems, approximations to ψ and θ are computed from tracker data by the assumption that \bar{x} is colinear with the flight path tangent, an assumption which is generally not true because of angle-of-attack (or sideslip). In the bank stabilized system,

$\phi = 0$ by virtue of autopilot control, and in the roll stabilized system, ϕ is computed from Equation [11]. Let ψ' , θ' and ϕ' be the apparent, or approximate values of the true Euler angles ψ , θ and ϕ . Then, with reference to Equation [3], if

$$\bar{u} = (u_{10}\bar{X}_0 + u_{20}\bar{Y}_0 + u_{30}\bar{Z}_0) \quad [7]$$

is the desired command vector at any instant of time (for example, \bar{u} may be the desired acceleration vector), the ground computed pitch and yaw commands are

$$(\text{pitch command}) = u'_{3b}$$

$$(\text{yaw command}) = u'_{2b}$$

where, from the usual coordinate transformation equations (4)

$$\begin{aligned} u'_{3b} &= (\sin \psi' \sin \phi' + \cos \psi' \sin \theta' \cos \phi')u_{10} + \\ &\quad (-\cos \psi' \sin \phi' + \sin \psi' \sin \theta' \cos \phi')u_{20} + \\ &\quad (\cos \theta' \cos \phi')u_{30} \\ u'_{2b} &= (-\sin \psi' \cos \phi' + \cos \psi' \sin \theta' \sin \phi')u_{10} + \\ &\quad (\cos \psi' \cos \phi' + \sin \psi' \sin \theta' \sin \phi')u_{20} + \\ &\quad (\cos \theta' \sin \phi')u_{30} \end{aligned} \quad [8]$$

(Note that the normal force produced by a pitch angle-of-attack, rotation about the y axis, is directed along the \bar{z} axis. It is assumed that means for producing command accelerations along the \bar{x} axis are not available.)

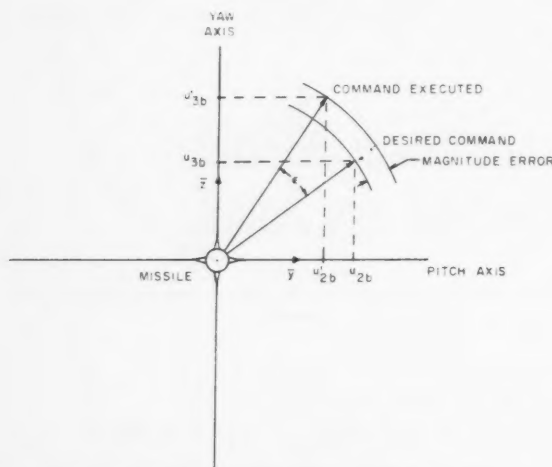


Fig. 3 Command geometry missile viewed head-on

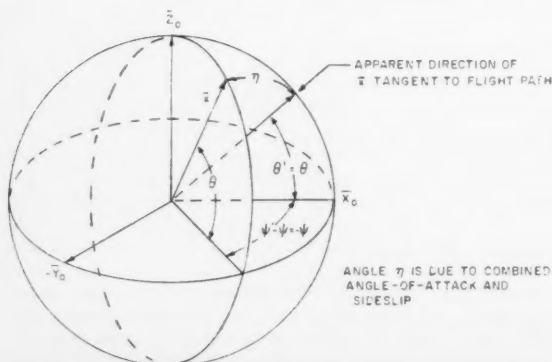


Fig. 4 Combined angle-of-attack and sideslip geometry

These commands are executed by the missile along the true y and z directions, so that, whereas the desired response is

$$(u_{2b}\bar{y} + u_{3b}\bar{z})$$

the actual response is

$$(u'_{2b}\bar{y} + u'_{3b}\bar{z})$$

If the missile is viewed head-on, looking along the longitudinal, or \bar{x} axis, the command geometry will appear as shown in Fig. 3. In this way, the command error can be visualized as a rotation ϵ and a fractional magnitude change δ where

$$\begin{aligned} \epsilon &= \tan^{-1} \frac{u'_{3b}}{u'_{2b}} - \tan^{-1} \frac{u_{3b}}{u_{2b}} \\ \delta &= \left(\frac{(u'_{2b})^2 + (u'_{3b})^2}{u_{2b}^2 + u_{3b}^2} \right)^{1/2} - 1 \end{aligned} \quad [9]$$

A preliminary comparison of the bank stabilized and roll stabilized systems is presented below in terms of the errors ϵ and δ under a limited number of conditions. It is assumed that at some time t all errors are zero and $\psi = \phi = 0$. Immediately after time t , the missile trims a particular combination of angle-of-attack and sideslip designated η , Fig. 4, such that the radar error is

$$\begin{aligned} \psi' - \psi &= -\psi \\ \theta' - \theta &= 0 \end{aligned}$$

In the presence of this radar error, a command $\bar{u} = k\bar{Y}_0$ is transmitted to the missile. Since η as described produces a change in ψ only, the relation between ψ and η is readily determined. With reference to Fig. 4

$$-\sin \psi/2 = \sec \theta \sin \eta/2 \quad [10]$$

Thus, from Equations [6, 8 and 10]:

In both systems

$$\begin{aligned} u_{10} &= u_{30} = 0 \\ u_{20} &= k \end{aligned} \quad [11]$$

In the bank stabilized system

$$\begin{aligned} \phi &= \phi' = 0 \\ u_{3b} &= k \sin \psi \sin \theta \\ u_{2b} &= k \cos \psi \\ u'_{3b} &= 0 \\ u'_{2b} &= k \end{aligned} \quad [12]$$

In the roll stabilized system

$$\begin{aligned} \phi &= \psi \sin \theta \\ u_{3b} &= \{-\cos \psi \sin (\psi \sin \theta) + \sin \psi \sin \theta \cos (\psi \sin \theta)\}k \\ u_{2b} &= \{\cos \psi \cos (\psi \sin \theta) + \sin \psi \sin \theta \sin (\psi \sin \theta)\}k \\ u'_{3b} &= 0 \\ u'_{2b} &= k \end{aligned} \quad [13]$$

The resulting error ϵ computed from equations [9 through 13] is plotted as a function of η with θ as a parameter in Fig. 5. These results show a rather striking superiority of the roll stabilized system over the bank stabilized system under the specific conditions chosen. It should be noted that the choice $\psi' = \psi(t) = 0$ is not at all restrictive, since the direction of \bar{Y}_0 in the "horizontal" reference plane is completely arbitrary. The magnitude error δ is comparable in both systems and does not exceed 0.15 for $\eta < 30$ deg.

Guidance Degradation Due to Command Errors

An intuitive appreciation for the effect of a rotation error ϵ can be obtained by analysis of a simplified sampled data guidance model in which missile position measurements are made at regular intervals and a lateral translation of the missile is effected without delay in response to command immediately after a measurement is made. In the case considered, the missile is initially flying a straight line path parallel to, but displaced from, the desired straight line trajectory. It is assumed that differences in displacement of the missile from the desired path, measured normal to the missile longitudinal axis, due to changes in missile heading are small enough to be neglected. Heading changes of ± 30 deg are probably acceptable in this context.

The error geometry viewed in a missile head-on perspective is as shown in Fig. 6. A coordinate system fixed to the desired trajectory is oriented so that the initial displacement is along the abscissa. The missile vector displacement at the i th data sampling time is \bar{E}_i , and the vector command displacement executed by the missile immediately thereafter is \bar{C}_i . Ideally \bar{C}_i would equal $-\bar{E}_i$; however, due to ϵ , \bar{C}_i is unintentionally rotated from $-\bar{E}_i$ and because of this rotation it is desirable to modify the magnitude of \bar{C}_i by a factor A . Thus

$$\begin{aligned}\bar{E}_{i+1} &= \bar{E}_i + \bar{C}_i \\ |\bar{C}_i| &= A|\bar{E}_i|\end{aligned}\quad [14]$$

and if

$$\bar{E}_i = a_i \bar{v}_1 + b_i \bar{v}_2 \quad [15]$$

then, in matrix notation

$$\begin{pmatrix} a_{i+1} \\ b_{i+1} \end{pmatrix} = \begin{pmatrix} a_i \\ b_i \end{pmatrix} - A \begin{pmatrix} \cos \epsilon & -\sin \epsilon \\ \sin \epsilon & \cos \epsilon \end{pmatrix} \begin{pmatrix} a_i \\ b_i \end{pmatrix} \quad [16]$$

which can be reduced to

$$\begin{pmatrix} a_{i+1} \\ b_{i+1} \end{pmatrix} = M \begin{pmatrix} a_i \\ b_i \end{pmatrix} \quad [17]$$

where

$$M = \begin{pmatrix} 1 - A \cos \epsilon & -A \sin \epsilon \\ A \sin \epsilon & 1 - A \cos \epsilon \end{pmatrix} \quad [18]$$

Consequently

$$\begin{pmatrix} a_i \\ b_i \end{pmatrix} = M^i \begin{pmatrix} a_0 \\ b_0 \end{pmatrix} \quad [19]$$

where

$$\begin{pmatrix} a_0 \\ b_0 \end{pmatrix} = \text{initial vector displacement}$$

Let

$$\begin{aligned}\rho &= (1 - 2A \cos \epsilon + A^2)^{1/2} \\ \xi &= \sin^{-1} \left(\frac{A \sin \epsilon}{\rho} \right)\end{aligned}\quad [20]$$

Then

$$M = \rho \begin{pmatrix} \cos \xi & -\sin \xi \\ \sin \xi & \cos \xi \end{pmatrix} \quad [21]$$

which is the product of a scalar ρ and a magnitude preserving rotation matrix. Therefore

$$\frac{|\bar{E}_i|}{|\bar{E}_0|} = \rho^i \quad [22]$$

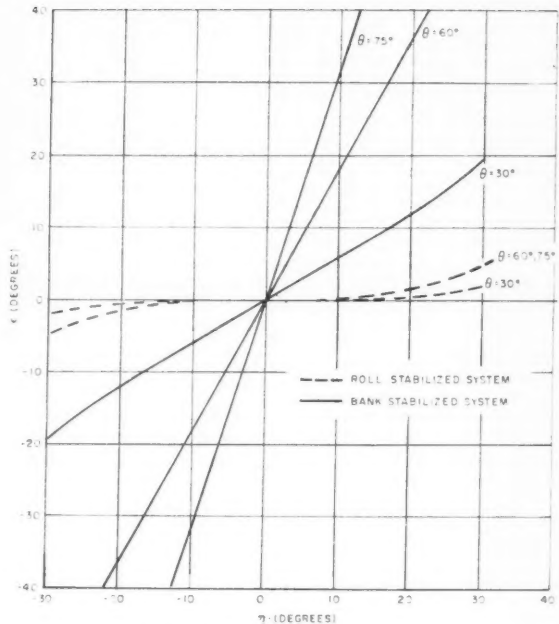


Fig. 5 Rotation error ϵ vs. η

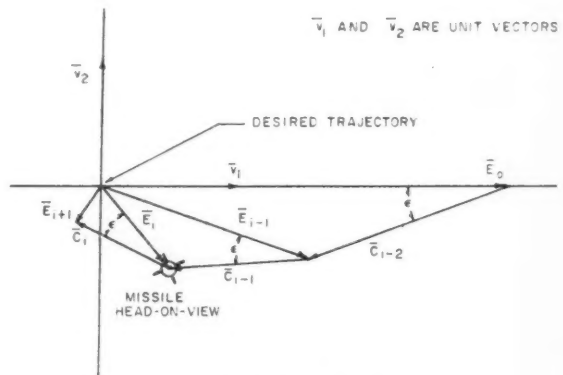


Fig. 6 Error geometry

A quasi system rise time τ can be defined as the number of sample periods required to reduce the ratio $|\bar{E}_i|/|\bar{E}_0|$ to 0.1. It follows that

$$0.1 = \rho^\tau$$

or

$$\tau = \frac{1}{\log_{10}(1/\rho)} \quad [23]$$

It is evident that the sequence \bar{E}_i will not converge if $\rho \geq 1$, and further, that τ will be minimum when ρ is minimum. Minimization of ρ is accomplished by adjustment of A , Equation [21]. A tabulation of τ vs. ϵ for two values of A , minimizing ρ for $\epsilon = 0$ and $\epsilon = 30$ deg respectively is given

Table 1 Rise time τ vs. command rotation error ϵ

ϵ , deg	τ (sample periods)	
	ρ minimized at $\epsilon = 0$ deg	ρ minimized at $\epsilon = 30$ deg
0	0	1
5	1	1
10	1	1
20	2	2
30	4	3
45	9	7
60	∞	37

in Table 1. The value of τ listed is the integer nearest the value computed from Equation [23].

Conclusions

From the preceding analyses, it is concluded that in many cases³ much smaller command errors occur in a roll stabilized system than in a bank stabilized system. It has been shown

³ The author has been unable to conceive of any case in which the reverse is true.

that situations can readily be synthesized in which errors in the two systems differ by an order of magnitude.

For example, with reference to Fig. 5, if $\theta = 60$ deg and if the combined angle-of-attack and angle-of-sideslip η is 20 deg, then the rotation errors are approximately 37 and 2 deg in the bank and roll stabilized systems respectively. Further reference to Table 1 shows that in this case the bank system rise time, τ , is more than three times as large as the roll system rise time. In both systems a reduction of command errors can be accomplished by guidance computer estimation of angle-of-attack from missile lift characteristics and command history; however, this additional correction is probably unnecessary in a roll stabilized system.

In addition to the roll stabilized system advantages shown in this analysis, it should be noted, with reference to Fig. 1, that the roll system rate integrating gyro (or rate gyro plus integrator) will never tumble and is inherently a more rugged device than the bank system free gyro.

References

- 1 Locke, A. S. et al., "Guidance," D. Van Nostrand Co., Princeton, N. J., 1955, p. 565.
- 2 Dow, R. B., "Fundamentals of Advanced Missiles," John Wiley and Sons, 1958, p. 217.
- 3 Locke, A. S. et al., "Guidance," D. Van Nostrand Co., Princeton, N. J., 1955, p. 329.
- 4 Goldstein, H., "Classical Mechanics," Addison-Wesley Publishing Co., Reading, Mass., 1950, pp. 107-109.

An Approximation to the Re-Entry Trajectory

MILDRED M. MOE¹

Space Technology Laboratories, Inc.
Los Angeles, Calif.

An approximation to the re-entry trajectory of a rocket or satellite is obtained by writing an integral equation for the trajectory angle and using simply the re-entry angle as a trial solution. The integrals can be evaluated if a constant drag coefficient and exponential atmospheric density are assumed. The approximation is good if the re-entry angle is greater than 5 deg and if the trajectory angle does not change greatly. However, even for trajectories which bend greatly, the approximation gives the qualitative behavior of the descent correctly. Results for a wide range of weight-to-drag ratios and initial conditions are compared with exact solutions.

WHEN a rocket or satellite enters the Earth's atmosphere, its trajectory is strongly influenced by air resistance. An accurate determination of the trajectory usually requires a numerical integration of the equations of motion. However, an approximate analytic solution can sometimes be useful for obtaining the important features of the descent. For example, the Allen-Eggers approximation,² which takes into account the effect of air resistance but neglects the gravitational force, is often adequate for calculating the maximum

deceleration of the vehicle. The purpose of this paper is to give an improved approximation which includes the effects of both air resistance and gravity on the re-entry trajectory of a nonlifting, freely falling body.

Equations of Motion

The force due to air drag is usually expressed as

$$F_D = (1/2)\rho(r)v^2C_DA$$

where

$\rho(r)$ = density of air at a distance r from the Earth's center
(assuming a spherically symmetric, nonrotating atmosphere)

Received Feb. 24, 1959.

¹ Member of the Technical Staff.

² Allen, H. J. and Eggers, A. J., Jr., "A Study of the Motion and Aerodynamic Heating of Missiles Entering the Earth's Atmosphere at High Supersonic Speeds," NACA TN 4047, Oct. 1957.

Equations [7 and 8] become

$$\cos \theta(h) = \frac{\cos \theta_0}{\left\{ 1 + 2 \ln \frac{r}{r_0} + \frac{2gr_0^2 e^{-z_0}}{\alpha v_0^2 r_0^2} [Ei(z) - Ei(z_0)] \right\}^{1/2}} \quad [9]$$

$$v(h) = v_0 \frac{\cos \theta_0}{\cos \theta} \frac{r_0}{r} e^{-(z-z_0)/2} \quad [10]$$

where

$$z = \frac{\lambda}{\alpha \sin \theta_0} e^{-\alpha h}$$

$$z_0 = \frac{\lambda}{\alpha \sin \theta_0} e^{-\alpha h_0}$$

$$Ei(z) = \int_{-\infty}^z \frac{e^x}{x} dx$$

Although this approximation should be valid only over the initial portion of the trajectory, it has been used for the entire trajectory in Table 1 to show how far it may be carried. The initial conditions are typical re-entry conditions for rockets and satellites and the weight-to-drag ratios $W/C_D A$ cover a reasonable range. The value of h_0 was taken to be 250,000 ft and the density of the atmosphere was approximated by using $\alpha = 1/24,000 \text{ ft}^{-1}$ and $\rho_s = 2.37 \times 10^{-3} \text{ slug/ft}^3$. For comparison the exact trajectories, obtained by numerical integration⁴ of Equations [1 and 2], are also given. The program for numerical integration usually employs a variable C_D and a standard atmosphere, but in this case a constant C_D and an exponential atmospheric density with $\alpha = 1/24,000 \text{ ft}^{-1}$ and $\rho_s = 2.37 \times 10^{-3} \text{ slug/ft}^3$ were used.

The approximation can be improved by using expressions [9 and 10] down to an altitude h_1 where $\theta(h_1)$ is found to differ considerably from the initial angle θ_0 . Then the values $v_1 = v(h_1)$ and $\theta_1 = \theta(h_1)$ can be used as initial conditions for calculating the remaining portion of the trajectory by Equations [9 and 10] with θ_0, v_0 and z_0 now replaced by θ_1, v_1 and z_1 . If desired new values of α and C_D may be used to give a more realistic trajectory. Several such steps should greatly improve the results. However, if an accurate trajectory is needed and a high speed computer is available, it is far faster to integrate numerically Equations [1 and 2] directly than to use many steps in this approximation procedure. The range of the re-entry trajectory is

$$R = r_s \int_0^\Phi d\phi = -r_s \int_{r_0}^{r_e} \cot \theta \frac{dr}{r}$$

By approximation [9] this is

$$R = -r_s \cot \theta_0 \int_{r_0}^{r_e} \left\{ 1 + \frac{2}{\sin^2 \theta_0} \ln \frac{r}{r_0} + \frac{A_0 r_s^2}{r_0^2} [Ei(z) - Ei(z_0)] \right\}^{-1/2} \frac{dr}{r} \quad [11]$$

where

$$A_0 = 2ge^{-z_0}/\alpha v_0^2 \sin^2 \theta_0$$

If the trajectory is short range, so the Earth's curvature is unimportant, these approximations take a simpler form suitable to a "flat Earth." By letting r_0, r_s and r approach infinity, we obtain

$$\cos \theta(h) = \frac{\cos \theta_0}{\left\{ 1 + (2g/\alpha v_0^2) e^{-z_0} [Ei(z) - Ei(z_0)] \right\}^{1/2}} \quad [12]$$

$$v(h) = v_0 \frac{\cos \theta_0}{\cos \theta} e^{-(z-z_0)/2} \quad [13]$$

⁴ The numerical integration was done on the IBM 704 by a program used for trajectory studies by the Applied Aerodynamics Department of Space Technology Laboratories.

The range becomes

$$R = -\cot \theta_0 \int_{h_0}^0 \{ 1 + A_0 [Ei(z) - Ei(z_0)] \}^{-1/2} dh \quad [14]$$

or

$$R = \frac{\cot \theta_0}{\alpha \sqrt{B_0}} \int_{z_0}^{z_s} \{ 1 + C_0 Ei(z) \}^{-1/2} \frac{dz}{z} \quad [15]$$

where

$$C_0 = A_0/B_0$$

$$B_0 = 1 - A_0 Ei(z_0)$$

$$z_s = \lambda/\alpha \sin \theta_0$$

As a special case we set $g = 0$ to remove the effect of gravity. Equations [12 and 13] then yield the Allen-Eggers approximation

$$\theta(h) = \theta_0 \quad v(h) = v_0 e^{-(z-z_0)/2} \quad [16]$$

The body moves in a straight line with its speed decreasing due to air resistance. This approximation is good for bodies with high weight-to-drag ratios, since such bodies are not retarded enough for gravity to produce an important bending of their trajectories.

With the gravity term retained, Equation [15] for the range may be evaluated approximately by dividing the range of integration into several parts. From $z = z_0$ to $z = 1$, $C_0 Ei(z)$ is usually small compared to 1. Therefore, the quantity $\{ 1 + C_0 Ei(z) \}^{-1/2}$ can be expanded and the first two terms easily integrated. From $z = 1$ to $z = 10$, $Ei(z)$ can be approximated by a few quadratic sections, again making an integration possible. Beyond $z = 10$, $C_0 Ei(z)$ is usually large compared to 1. If we neglect 1 and use the first term e^z/z of the asymptotic expansion of $Ei(z)$, the integral from $z = 10$ to $z = z_s$ (if z_s extends into this range) becomes an error function. If we use this method to estimate, for example, the re-entry range of the first trajectory in Table 1 ($W/C_D A = 10 \text{ lb/ft}^2$, $\theta_0 = 45 \text{ deg}$, $v_0 = 8000 \text{ fps}$), we obtain $1.34 \times 10^5 \text{ ft}$ compared to the exact range of $1.49 \times 10^5 \text{ ft}$. (If the body fell under the force of gravity alone, the re-entry trajectory would have been approximately a parabola of range $2.24 \times 10^5 \text{ ft}$.) The range on a round Earth, as given by Equation [11], can be approximated in a similar manner. If the term $(2/\sin^2 \theta_0) \ln(r/r_0)$ is small compared to the other terms, the quantity in the square root may be expanded suitably and the logarithmic term integrated to give a correction to the flat Earth range [15]. For example, the range of the second trajectory in Table 1 ($W/C_D A = 10 \text{ lb/ft}^2$, $\theta_0 = 20 \text{ deg}$, $v_0 = 24,000 \text{ fps}$) is 3.86×10^5 in this approximation compared to $3.98 \times 10^5 \text{ ft}$ for the exact range.⁵

Conclusions

This approximation to the re-entry trajectory gives an extension and improvement of the Allen-Eggers result (Eq. [16]). In particular, it gives a better value for the speed of the vehicle, it approximates the curvature of the trajectory and provides a reasonable estimate of the re-entry range. The examples in Table 1 show that, as expected, the approximation is good whenever the changes in the trajectory angle are small. Even when the angle changes by a large

⁵ It is difficult to say how much the exact (or model) trajectories given here differ from actual trajectories, since the latter are determined partly by the dependence of drag coefficient on Mach number for the particular re-entry body. To obtain some measure of the discrepancies one should expect, a number of actual trajectories were calculated by a numerical integration using the density of the ARDC model atmosphere (1956) and three different curves of drag coefficient vs. Mach number. It was found that the re-entry ranges of these trajectories differed by -1 to $+3$ per cent from the ranges of the model trajectories. The final speeds were in all cases of the same order as those of the model trajectories, varying from 50 to 130 per cent of those given in Table 1 in the columns labeled "exact."

Table 1 Approximate trajectories computed from Equations [9 and 10] compared to exact trajectories obtained by numerical integration of Equations [1 and 2]

$\frac{W}{C_D A} \left(\frac{\text{lb}}{\text{ft}^2} \right)$	$h, \text{ft} \times 10^3$	Approximate		Exact		Approximate		Exact		Approximate		Exact	
		θ, deg	$v \times 10^{-3}, \text{fps}$	θ	$v \times 10^{-3}$	θ	$v \times 10^{-3}$	θ	$v \times 10^{-3}$	θ	$v \times 10^{-3}$	θ	$v \times 10^{-3}$
10	250	45.00	8.00	45.00	8.00	20.00	24.00	20.00	24.00	5.00	30.00	5.00	30.00
	200	46.25	7.98	46.24	7.98	20.07	22.75	20.07	22.73	4.78	24.10	4.79	23.88
	150	47.64	6.59	47.62	6.62	20.37	14.53	20.36	14.60	10.43	4.15	9.19	5.90
	100	55.40	1.35	54.43	1.54	53.15	0.601	41.14	1.02	90.00	0.220	59.22	0.856
	50	90.00	0.222	89.99	0.266	90.00	0.153	89.99	0.266	90.00	0.000	90.00	0.265
	0.000	90.00	0.000	90.00	0.092	90.00	0.000	90.00	0.092	90.00	0.000	90.00	0.092
10^2	250	45.00	8.00	45.00	8.00	20.00	24.00	20.00	24.00	5.00	30.00	5.00	30.00
	200	46.22	8.17	46.22	8.17	20.06	23.93	20.05	23.93	4.60	29.40	4.60	29.36
	150	47.37	8.19	47.35	8.19	20.13	22.94	20.13	22.94	4.37	24.66	4.40	24.06
	100	48.61	7.05	48.58	7.09	20.38	16.01	20.38	16.03	8.19	5.98	8.06	7.00
	50	53.44	1.91	52.86	2.15	36.75	1.01	32.16	1.46	89.99	0.247	51.63	0.987
	0.000	90.00	0.249	89.94	0.299	90.00	0.171	89.95	0.299	90.00	0.000	89.97	0.299
10^3	250	45.00	8.00	45.00	8.00	20.00	24.00	20.00	24.00	5.00	30.00	5.00	30.00
	200	46.22	8.19	46.21	8.19	20.06	24.05	20.06	24.05	4.58	29.99	4.58	29.99
	150	47.34	8.37	47.33	8.37	20.12	24.01	20.11	24.01	4.13	29.51	4.14	29.42
	100	48.40	8.41	48.37	8.41	20.19	23.22	20.18	23.25	3.82	25.64	3.90	24.59
	50	49.51	7.49	49.46	7.53	20.38	17.40	20.37	17.45	6.49	8.21	7.13	8.05
	0.000	52.73	2.59	52.33	2.87	28.10	1.78	26.62	2.21	89.83	0.278	58.24	0.879

amount (for example, from 5 to 90 deg), it gives qualitatively the rapid bending of the trajectory near the bottom of the atmosphere. The results may be improved by dividing the trajectory into several sections in which different values of h_0 , v_0 and θ_0 are used. The appropriate division can be estimated from the rate at which the angle θ is found to change. This approximation cannot, of course, replace machine computations when accurate results are needed. It serves

mainly as an analytical structure for understanding re-entry trajectories and predicting their general behavior.

Acknowledgment

The author wishes to thank Dr. A. D. Wheelon for suggesting this problem. The development of this approximation is due largely to his encouragement.

ARS SOLID PROPELLANTS CONFERENCE

January 28-29, 1960

Princeton University, Princeton, N. J.

Unstable Burning—Theoretical
Unstable Burning—Experimental
Grain Design

Combustion, Gas Kinetics and Ignition
Interrelations of Nozzle Geometry
and Nozzle Performance

Use of Energy Storage in Low Thrust Spaceflight¹

MORTON CAMAC

Avco-Everett Research Laboratory
Everett, Mass.

This paper analyzes flight plans for spacecraft operating at thrust levels that are much smaller than the local gravitational force, e.g., electrical propulsion near the Earth. The thrust is limited by the average power generated. For power limited flight, it has been suggested by Irving and Blum that the shortest flight times are obtained when operating at constant (thrust) acceleration. However, there was no consideration of the use of energy storage which permits more freedom for programming the thrust while still utilizing all the available energy. In particular, the electric energy can be stored in batteries over a portion of an orbit revolution and used to provide a short thrust impulse at a point along the orbit. The batteries would be recycled each revolution and used repeatedly. The performance with and without energy storage is compared for two types of missions, both in the gravitational field of the Earth: Round trips from small to larger circular orbits, and rendezvous maneuvers between orbits at low altitudes. It is shown in case 1 that even with the extra weight of the storage batteries, flight plans can be achieved in some cases which reduce both the flight time and the propellant requirements. For case 2 many flight plans require that thrust be applied at only limited portions of the orbit. With energy storage all the available energy can be utilized, thereby substantially decreasing the flight time and the guidance problem.

THE PROBLEM of making a transfer between two orbits has been considered by many authors. For example, Hohmann (2)² showed that for a transfer between two circular orbits there is a minimum impulse flight plan consisting of two impulses of short duration; see Fig. 5. The first impulse changes the vehicle's orbit from the initial circle to the transfer ellipse which is tangent to the final desired orbit; the vehicle proceeds in free flight along the ellipse. The second impulse is applied at the point of tangency to the final orbit and the vehicle thereafter moves along the final circular orbit. Each impulse must be applied over a time interval that is very small compared to an orbit revolution. For missions originating from a low altitude above the Earth, Hohmann flight plans are limited to chemical propulsion.

Irving and Blum (1) and Stuhlinger (4) have made analyses of transfers between circular orbits when using power limited low thrust propulsion systems. Examples of these are electrical or solar heater (3) propulsion. The thrust acceleration of these systems is much less than 1 *g* (32 fps), and the Hohmann flight plan with two short intense impulses cannot be achieved. These authors show that the shortest flight time is obtained when the thrust is applied continuously, producing a spiral orbit. However, they did not incorporate the possibility of storing some of the energy, and in this respect, their analyses were incomplete. It can be shown that the total thrust impulse required to make a transfer between two orbits depends upon the flight plan, the total impulse for the Hohmann flight plan being much less than that for the spiral orbit flight plan. With the use of energy storage flight plans can be obtained that have the same total impulse as

for the Hohmann flight plan. This can lead to a reduction in both the propellant consumption and flight time.

This paper analyzes flight plans in which a part of the energy is stored for a portion of the orbit flight. This energy is then used more effectively when expended for short thrust impulses at desirable points along the orbit. The storage system is recycled during each orbit, thereby permitting a sequence of thrust impulses. A comparison between propulsion systems with and without energy storage is presented for two missions within the gravitational field of the Earth: 1 Flight from an altitude of 100 miles to an orbit at a larger altitude, and subsequent return to the Earth; 2 simple interception and rendezvous missions between two satellite vehicles at low altitudes.

Energy storage is also advantageous for missions at low altitudes. In most low altitude maneuvers (for example, transfers from circular to elliptical orbits, or between orbits that are not in the same plane), optimum operation is achieved when impulses are applied only over limited portions of the orbits. The use of energy storage in low thrust propulsion systems permits the application of short impulses while still utilizing all available energy. This decreases the flight time for the maneuver, and considerably simplifies the guidance and control problem.

As a specific example, the present paper considers the use of storage in electrical propulsion systems, for which electric energy is stored in batteries. The advantage of storage is that better flight performance is obtained with short thrust impulses at limited regions along the orbits, while utilizing all the available energy. The disadvantage is the weight penalty of the storage batteries that must be used. The extent to which electric storage is useful for reducing the flight time and propellant consumption depends mainly upon the relative weights of the batteries and the rest of the propulsion system. The practical use of batteries was examined for missions to lunar orbits. It is shown that with nickel-cadmium cells, battery storage is of advantage when the specific weights of propulsion systems are about 20 lb/kw or more.

An original version of this paper was presented at the ARS 13th Annual Meeting, New York, N. Y., Nov. 17-21, 1958, titled "Reduction of Flight Time and Propellant Requirements of Satellites with Electric Propulsion by the Use of Stored Electrical Energy."

¹ The work was sponsored in part by the U. S. Air Force Office of Scientific Research, ARDC, under contract AF 49 (638)-61.

² Numbers in parentheses indicate References at end of paper.

Missions to Large Circular Orbits

In this section missions that require transfers between low and high altitude circular orbits are considered. The flight plans with and without the use of electric energy storage are evaluated, and a comparison is made of the propellant requirements and the flight times. In order to use a minimum of calculations, two approximate flight plans are treated since the results can be expressed in simple analytical form: 1 A series of elliptical orbits produced by short thrust impulses; 2 the spiral orbit resulting from continuous thrust.

Some preparatory material is now presented with which this evaluation is made. First, satellite orbit nomenclature and kinematics are described. Next, the total mission impulse for a Hohmann transfer ellipse, and for elliptical and spiral orbit flight plans are determined. Then the formulas for the payload weight ratio are presented as a function of the flight time for given mission parameters. Finally, a comparison is made of the performance with and without energy storage using these preparatory results.

Orbit Description and Kinematics

We will assume that the only gravitational force felt by the satellite is the inverse square force acting from the center of the Earth. Perturbations due to the equatorial bulge, air drag and other celestial bodies are neglected. Thus, the orbit is an ellipse which is described by the variables shown in Fig. 1, where

- R = distance from Earth's center to satellite
- R_p = distance from Earth's center to perigee point
- R_a = distance from Earth's center to apogee point
- θ = angle that radius vector makes with perigee line

The equation of the ellipse is

$$R = \frac{a(1 - e^2)}{1 + e \cos \theta} \quad [1]$$

where the semimajor axis $a = \frac{1}{2}(R_a + R_p)$ and the eccentricity $e = (R_a - R_p)/(R_a + R_p)$. In terms of R_a and R_p

$$R = \frac{2R_a R_p}{(R_a + R_p) + (R_a - R_p) \cos \theta} \quad [2]$$

Also shown in Fig. 1 is the Earth with a mean radius R_E . The altitude of the satellite above the surface of the Earth is given by $h = (R - R_E)$. The apogee and perigee altitudes are $h_a = (R_a - R_E)$ and $h_p = (R_p - R_E)$, respectively.

The period of an orbit revolution τ is given by the formula (6)

$$\tau = \frac{\pi}{\sqrt{2g_0 R_E^2}} (R_a + R_p)^{3/2} \quad [3]$$

where g_0 (32.1 ft/sec²) is the gravitational acceleration at the surface of the Earth. Fig. 2 presents the orbit period as a function of altitude h for two cases: Circular orbits, and elliptical orbits with perigee altitude at 100 nautical miles and apogee at h .

In order to determine the velocities of the satellite in a given orbit, it is convenient to start with the equation for the total energy which is constant in time. The total energy E is equal to the potential plus kinetic energies as shown in the formula

$$E = -\frac{g_0 R_E^2}{R} + \frac{v^2}{2} \quad [4]$$

Note that the total energy is zero when the satellite is at rest a very large distance from the Earth. Constant angular momentum along the orbit gives the result that $R_a v_a = R_p v_p$ (6). Inserting this relation into the equation for the energy, we obtain the desired form for the velocity of the satellite at

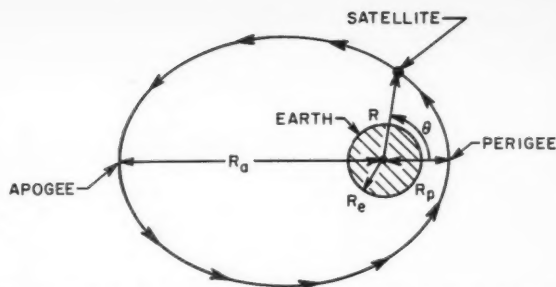


Fig. 1 Notation used for the description of the elliptical orbit

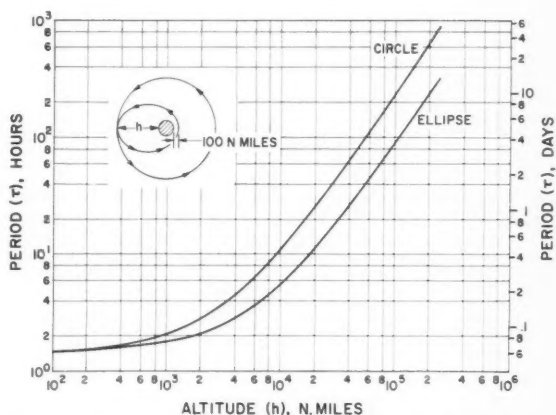


Fig. 2 The period of orbit revolution for circular orbits at altitude h and for elliptical orbits with perigee at 100 nautical miles and apogee at altitude h

any point along the orbit

$$v^2 = 2g_0 R_E^2 \left(\frac{1}{R} - \frac{1}{R_a + R_p} \right) \quad [5]$$

Thus the velocities at apogee and perigee are

$$v_a = \sqrt{\frac{2g_0 R_E^2 R_p}{(R_a + R_p) R_a}} \quad v_p = \sqrt{\frac{2g_0 R_E^2 R_a}{(R_a + R_p) R_p}} \quad [6a]$$

For the special case of a circular orbit the velocity v_c is

$$v_c = \sqrt{\frac{g_0 R_E^2}{R}} = \sqrt{\frac{g_0 R_E^2}{R_E + h}} \quad [6b]$$

Equation [6b] is plotted in Fig. 3 and denoted by v_c . The other two curves give the velocities at apogee v_a and perigee v_p for an elliptical orbit with perigee at 100 miles and apogee at an altitude h as calculated from Equation [6a]. Also shown are three intervals Δv_p , Δv_a and Δv_i . These intervals have the following physical significance: Δv_p is the difference in velocity at 100 miles altitude between a 100-mile circular orbit and an elliptical orbit with perigee at 100 miles and an apogee altitude at h . Similarly, Δv_a is the difference in velocity at an altitude h between a circular orbit at an altitude h and an elliptical orbit with apogee at h and perigee at 100 miles. Δv_i is the difference of velocity between two circular orbits at altitudes 100 miles and h . Fig. 4 shows the variation of the incremental velocities Δv_p , Δv_a , Δv_i and $(\Delta v_p + \Delta v_a)$ with h as just described in Fig. 3.

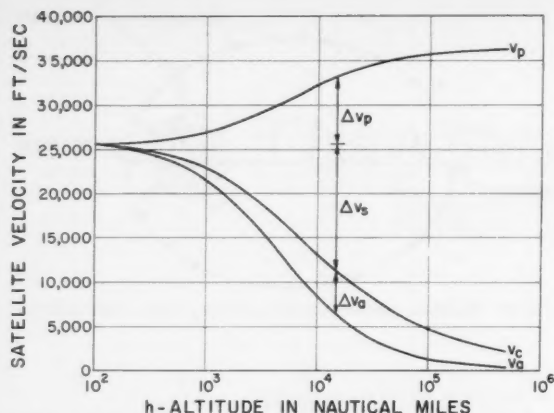


Fig. 3 Satellite velocity in a circular orbit v_c . Satellite velocities v_p and v_a at perigee and apogee, respectively, in an elliptical orbit with perigee at 100 miles and apogee at an altitude h

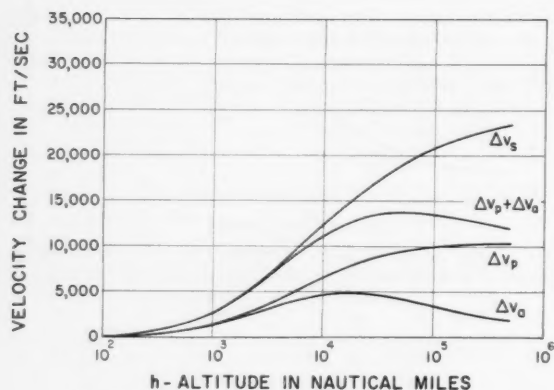


Fig. 4 Velocity differences as defined in Fig. 3

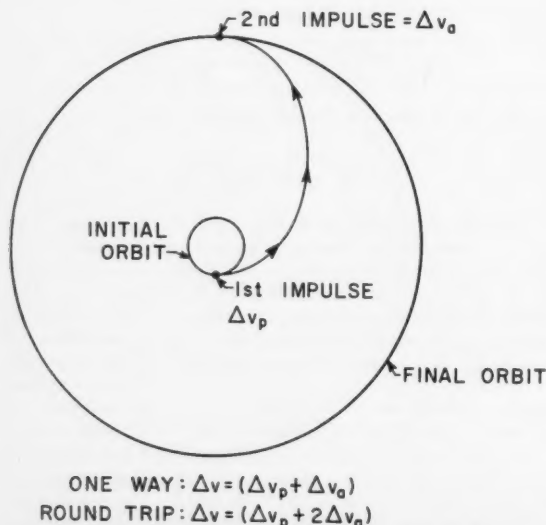


Fig. 5 Flight plan for the Hohmann transfer ellipse

Total Impulse for Missions

In order to obtain simple and analytic results, the total impulse requirements and the flight times will be determined for two extreme flight plans: 1 Short intense thrust impulses; 2 spiral orbits. In case 1 the thrust is assumed to be much larger than the local gravitational force, and the latter is neglected in determining the change in the orbit during the short impulse. Because of this assumption of rectilinear motion during the short impulse, the change in the vehicle's velocity is equal to the integrated thrust acceleration. For case 2 of the "tightly wound" spiral flight plan, the thrust is smaller than the local gravitational force, and is applied continuously in the direction of motion. The orbit, if initially circular, remains essentially a circle but of varying radius during the mission. Note that in a circular orbit a satellite's speed remains constant due to the balance of the gravitational and centrifugal forces. Thus, for the tightly wound spiral where the orbit is essentially always circular, any change in the vehicle's speed is equal to the velocity change produced by the thrust chamber. Thus, for these two extreme cases, we will make use of the simple result that the velocity increment produced by the integrated thrust acceleration during the transfer between two orbits is equal to the difference in speed of the vehicle in the two orbits. By assuming in case 2 that the vehicle's orbit remains essentially circular throughout the thrust period, the vehicle's gravitational potential energy is always twice the magnitude of the kinetic energy; see Equation [4]. Any change in the kinetic energy requires that the potential energy have twice as much change. Thus, it can be shown that when applying positive thrust the vehicle's velocity decreases, and that this velocity change is equal in magnitude to the integrated thrust acceleration but of opposite sign.

Hohmann Flight Plan

The Hohmann transfer ellipse flight plan is presented here because it represents the minimum total impulse plan. While it cannot be achieved with low thrust systems, it will serve as a guide in determining other flight plans. The two impulses required for a transfer from an initial circular orbit at 100 miles to a large circular orbit are shown in Fig. 5. For very short intense impulses at perigee and apogee, the required velocity changes of the vehicle are the Δv_p and Δv_a given in Fig. 4. As shown in the previous paragraph these velocity changes are equal to the integrated thrust acceleration that the thrust chamber must supply for this mission. Since the Hohmann transfer ellipse requires the minimum total impulse, the sum $(\Delta v_p + \Delta v_a)$ is the minimum velocity change due to thrust for a transfer between two circular orbits.

Spiral Orbit Flight Plan

In the spiral orbit flight plan the thrust is applied continuously for the transfer between two circular orbits. As shown previously in the limiting case of a tightly wound spiral, the integrated thrust acceleration is equal to the difference in velocity of the two orbits. This velocity increment is Δv_s for a mission from 100 miles altitude to a large circular orbit; see Fig. 4. Note that Δv_s is always larger than the sum $(\Delta v_p + \Delta v_a)$. Thus, other factors remaining unchanged, the spiral orbit flight plan always requires more propellant consumption than the Hohmann transfer ellipse. In fact, it is this difference that leads to the advantages of electrical energy storage for such missions.

It is interesting to discuss the reason why the total impulse requirements vary with the flight plan in making a transfer between two given orbits. A vehicle moving along a given orbit in space has a total energy that is independent of the way in which the vehicle reached that particular orbit. Consider a mission between two orbits of energies E_1 and E_2 . To effect a transfer between these two orbits would require the work $(E_1 - E_2)$ irrespective of the flight plan

$$E_1 - E_2 = \int (F \cdot v) dt \quad [7]$$

where F and v are the exhaust thrust force and the vehicle velocity vectors, respectively. We will assume that the thrust is applied in the direction of motion, thereby producing the most work. The vector equation becomes scalar and the integral reduces to

$$E_1 - E_2 = \int F v dt \quad [8]$$

The usual definition of the average velocity \bar{v} is

$$\bar{v} = \int g v dt / \int g dt \quad [9]$$

where g is an arbitrary function. In this case $\int F v dt = \bar{v} \int F dt$. Note that $\int F dt$ is the total thrust impulse for the mission and is equal to

$$\int F dt = (E_1 - E_2) / \bar{v} \quad [10]$$

Since the energy difference is independent of the flight path, the lowest total impulse is obtained when the thrust is applied at the highest satellite velocity. In more general terms, the thrust should also be applied in the direction of motion at the point of lowest potential energy. The Hohmann transfer ellipse flight plan meets these requirements for the first impulse. There are several ways to reach the final circular orbit by using one or more impulses. The Hohmann transfer ellipse is best only when both the impulse and the flight time are considered.

Elliptical Orbits With Low Thrust Systems

Electrical propulsion systems are limited to low thrust acceleration. For example, to obtain an acceleration of $10^{-2}g_0$ with specific impulse of 1000 sec, the total vehicle weight must be less than 5 lb for each kilowatt of directed power in the exhaust. This weight would be considered low for the power supply alone. Even for such a thrust operating continuously in the direction of motion, the shape of a low altitude orbit cannot be appreciably distorted. Starting with a circular orbit, a spiral orbit would result.

A method for approximating the minimum total impulse flight plan with the use of a low thrust propulsion system will now be presented. It is based on the fact that with the provision for energy storage, all the electric energy produced can be applied in short impulses. Consider a mission from 100 miles altitude to a high altitude orbit. Electric power produced at a constant rate (using solar or nuclear energy) would be stored in batteries over a portion of an orbit revolution. In the vicinity of perigee, the thrust chamber would be turned on and the batteries discharged producing a short impulse.³ The resulting flight path is shown in Fig. 6. With the short impulses at perigee, the apogee altitude would increase, but the perigee altitude would not change. This series of small thrust impulses at perigee requires the same total impulse as the single impulse Δv_p , used in the Hohmann transfer ellipse. When the apogee reaches the desired altitude, then impulses are applied at this apogee point in order to increase the perigee and thereby circularize the orbit.

The advantage of the elliptical orbits flight plan (using storage) over the spiral orbit plan (continuous thrust) becomes greater for a round trip from a low to a high altitude orbit and return. For the elliptical orbits flight plan part of the return trip can be assisted with atmospheric drag: The apogee pulses would make an elliptical orbit whose perigee lies inside the Earth's atmosphere. The collapsing of this ellipse into a low altitude circular orbit can be accomplished with atmospheric drag on the vehicle.

³ For most electrical propulsion systems (arc jet, magnetic accelerators, but not the ion rocket), the higher thrust level results in a more efficient operation of the thrust chamber.

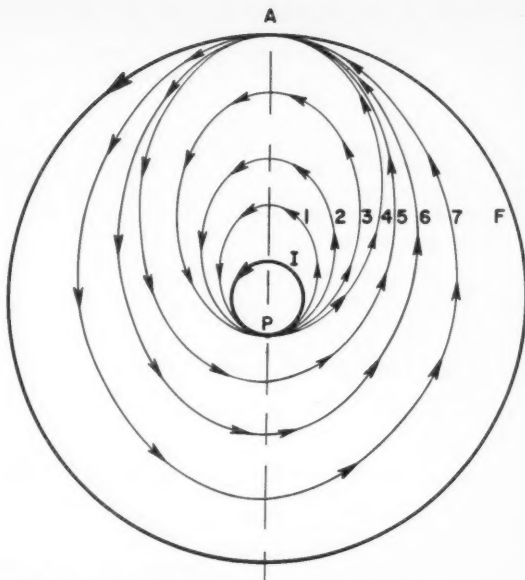


Fig. 6 Flight plan for a satellite using electrical propulsion with energy storage to go from a low altitude circular orbit at I to a larger circular orbit at F. Short impulses are initially applied at the point P producing a series of expanding ellipses 1, 2, 3 and 4. When the apogee of the expanding ellipses reaches the final circular orbit then pulses are applied at this apogee point A thereby increasing the perigee altitude and circularizing the ellipses 5, 6 and 7

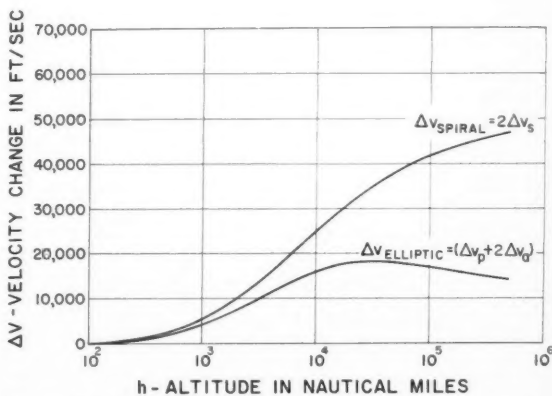


Fig. 7 Velocity increments Δv required to go from 100 miles altitude to a circular orbit at altitude h and return to Earth. Δv_{spiral} and $\Delta v_{\text{elliptic}}$ are the velocity increments for the spiral orbit and expanding ellipses flight plan, respectively

Fig. 7 shows the velocity increment Δv required for a round trip from a 100-mile circular orbit to a larger circular orbit of altitude h and return. The curve denoted by $\Delta v_{\text{elliptic}}$ is for the minimum impulse flight plan shown in Fig. 6 with atmospheric drag circularizing the return ellipse. The other curve Δv_{spiral} is for the spiral orbit flight; atmospheric drag cannot be used. The formulas for these velocity increments are

$$\Delta v_{\text{elliptic}} = (\Delta v_p + 2\Delta v_a) \quad \Delta v_{\text{spiral}} = 2\Delta v_s \quad [11]$$

Practical Propulsion Systems Using Battery Storage

The use of energy storage requires the incorporation of electric batteries in the propulsion system. Since these batteries have to be recycled many times the battery materials and the mode of operation are limited. Nickel cadmium and silver cadmium cells appear to be the most practical at the present time. These batteries have an operating weight of about 20 to 25 lb/kw-hr storage capacity. In order to maintain reliable operation over many recycles, the charging time must be at

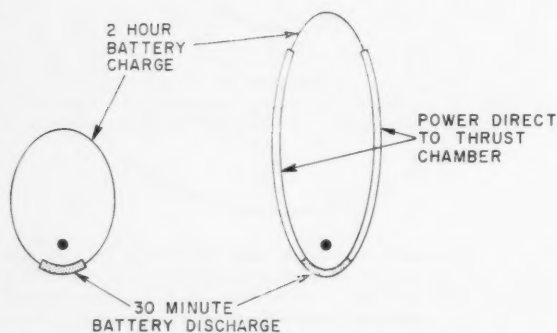


Fig. 8 Thrust program when using electrical energy storage for expanding the orbit

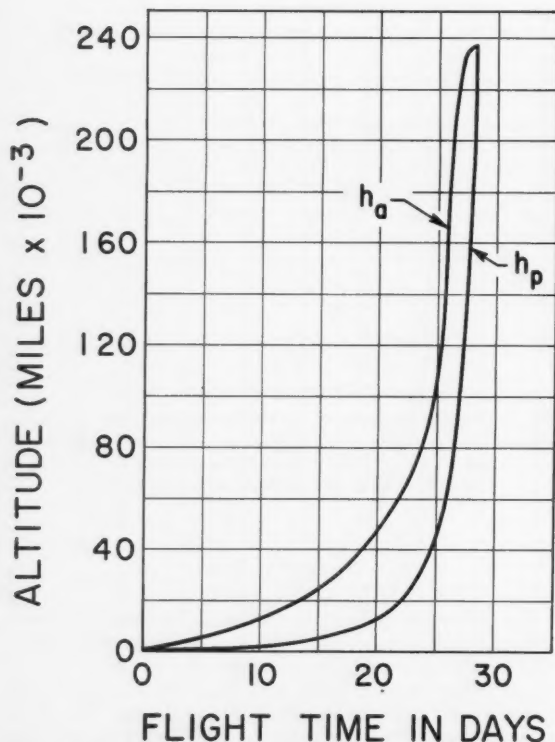


Fig. 9 Instantaneous apogee h_a and perigee h_p altitudes variation with time for the particular example given in text. The satellite makes many elliptical revolutions similar to the orbits shown in Fig. 6

least 1 hr and the discharge should be at least $\frac{1}{2}$ hr. The newly developed fuel cells show promise for a lighter weight with higher storage capacity. In the present discussion we have considered only the commercially available batteries.

A practical compromise has to be made between the most desirable storage capacity and the weight penalty of the batteries. For low altitude circular orbits, the orbit period is of the order of 1.5 hr. Since the batteries are recycled each revolution, the storage time need not be larger than the period of revolution. For larger orbits the orbit period increases with increasing apogee as shown in Fig. 2. However, the period is still only 2 hr even when the apogee is at 2000 miles altitude. When expanding into a highly elliptical orbit, the major part of the thrust is required in the initial expansion of the apogee from 100 miles to several thousand miles altitude, because the gravitational forces decrease with the square of the distance from the Earth's center.

A practical flight plan is shown in Fig. 8 where a 2-hr storage capacity is included in the electrical propulsion system. When the period of revolution is less than 2.5 hr, then the left figure applies. The solid line shows the free flight part of the orbit during which the electric energy production goes to the batteries for storage. The batteries are discharged into the thrust chamber for 30 min around perigee. These charging and discharging rates are consistent with long-life operation of the batteries. For periods greater than 2.5 hr the figure to the right applies; for 2 hr around apogee the electric energy is stored in the batteries, and for 30 min around perigee the batteries are discharged. During the rest of the orbit the battery system is not in use and the power goes directly to the thrust chamber. In this way all the energy produced is used for thrust.

We have carried out exact calculations (using a high speed computer) in order to determine the flight path when transferring from a 100-mile circular orbit to a lunar orbit using the thrust program similar to that described in Fig. 8 with 1, 1.5 and 2-hr battery storage capacity. Some of the results are presented in Fig. 9 for a 2-hr storage capacity case. The curves show the apogee and perigee altitudes as a function of time; the vehicle actually makes many elliptical revolutions similar to the orbits shown in Fig. 6. For this example, the total thrust requirement was within 10 per cent of that for the Hohmann transfer ellipse. Thus, little is to be gained in more than 2-hr storage capacity. When using 1-hr storage capacity, the thrust requirement was about 50 per cent greater. Different conclusions would be obtained when considering a transfer to another altitude. Obviously, the mission requirements and the specific weight of the power supply must be known before the amount of storage can be optimized and the advantages of storage can be evaluated.

Optimizing Payload Weight Ratio

In order to make a comparison of the spiral and elliptical orbit flight plans for specific missions, the payload weight ratio and the flight time must be calculated. We will use the following notation

- a = thrust acceleration
- c = exhaust velocity
- P = thrust power in the exhaust
- k = structure factor (propellant container is assumed proportional to the propellant weight)
- m = vehicle weight
- m_B = battery weight
- m_i = initial vehicle weight
- m_L = payload weight
- m_p = initial propellant weight
- m_w = power supply weight
- T = mission flight time
- $v_c = \sqrt{2T(1+k)/\alpha} \equiv$ characteristic velocity

$$\begin{aligned}\Delta v &= \int_0^T a dt = \text{velocity increment due to thrust acceleration} \\ \alpha &= m_w/P = \text{specific weight of propulsion system} \\ \alpha_B &= m_B/P = \text{specific weight of batteries}\end{aligned}$$

A given mission will have parameters that are fixed while others can be optimized. For example, the fixed quantities may be flight time T ; velocity change due to thrust Δv ; structure factor k , and specific weight α . The expression for the payload weight ratio (m_L/m_i) will be derived assuming that the exhaust power P , averaged over an orbit revolution, is constant. Conservation of mass gives the relation

$$m_i = (1+k)m_p + m_w + m_L \quad [12]$$

when the subscripts i , p , w and L are defined in the foregoing. The use of the structure factor k assumes that the propellant container is proportional to the propellant. The propellant required for the mission is

$$m_p = \int_0^T \dot{m} dt = \int_0^T \frac{2P}{c^2} dt = \frac{2m_w}{\alpha} \int_0^T \frac{dt}{c^2} \quad [13]$$

where

$$\begin{aligned}c &= \text{exhaust velocity} \\ \alpha &= \text{specific weight of the propulsion system} \\ T &= \text{total flight time}\end{aligned}$$

Integrating the rocket reaction equation $a = \dot{m}c/m$

$$m_p = m_i(1-e)^{-\int_0^T (a/c) dt} \quad [14]$$

where a and c are the instantaneous acceleration and exhaust velocity. These equations combine to give the payload weight ratio

$$\frac{m_L}{m_i} = 1 - \left(1 - e^{-\int_0^T (a/c) dt}\right) \left(1 + k + \frac{\alpha}{2 \int_0^T (dt/c^2)}\right) \quad [15]$$

No attempt has been made to maximize the payload weight ratio for all possible flight paths between two circular orbits. However, the results presented are for two important cases: 1 Constant acceleration, and 2 constant exhaust velocity. It has been shown (1) that a larger payload weight ratio is obtained for the constant acceleration case. However, the difference between the two cases is negligible when the payload weight ratio is over 20 per cent as shown in Fig. 10. Case 2 with constant exhaust velocity is applicable to systems like the nuclear rocket or solar heater where it is desirable to operate at the maximum specific impulse obtainable.

CASE 1: The acceleration a is kept constant. The payload weight ratio is obtained by first eliminating c in the equations $\dot{m}c = am$ and $mc^2 = 2m_w/\alpha$, and then integrating. One obtains the relation

$$\frac{m_i}{m_p} = 1 + \frac{m_w}{m_i} \frac{2T}{\alpha(\Delta v)^2} \quad [16]$$

where Δv is the velocity increment produced by thrust acceleration. Substituting for m_p in Equation [8] the payload weight ratio becomes

$$\frac{m_L}{m_i} = 1 - \left\{ \frac{1}{[m_w/m_i][2T/\alpha(\Delta v)^2] + 1} \right\} (1+k) - \frac{m_w}{m_i} \quad [17]$$

where (m_w/m_i) can take a range of values. m_L/m_i is a maximum when

$$\frac{m_w}{m_i} = (1+k) \left[\left(\frac{\Delta v}{v_c} \right) - \left(\frac{\Delta v}{v_c} \right)^2 \right] \quad [18]$$

where v_c is called the characteristic velocity and is defined

$$v_c \equiv \sqrt{\frac{2T(1+k)}{\alpha}} \quad [19]$$

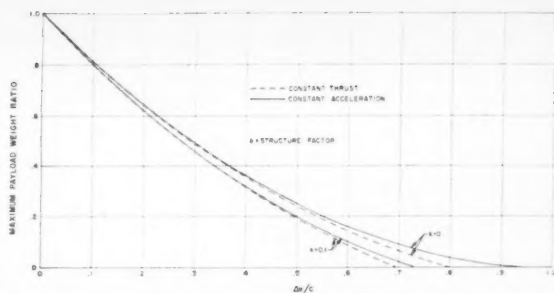


Fig. 10 The maximum payload weight ratio as a function of $\Delta v/c$. The structure factor k was fixed at 0 and 0.1. The solid curves are for constant acceleration and the dashed curves are for constant exhaust velocity flight plans

The maximum payload weight ratios becomes

$$\left(\frac{m_L}{m_i} \right) = (1+k) \left(1 - \frac{\Delta v}{v_c} \right)^2 - k \quad [20]$$

which is only a function of $\Delta v/v_c$ and k .

CASE 2: The exhaust velocity c is kept constant. Then Equation [15] becomes

$$\frac{m_L}{m_i} = 1 - (1+k)(1 - e^{\Delta v/c}) \left(1 + \frac{c^2}{v_c^2} \right) \quad [21]$$

The exhaust velocity c is the only variable, as Δv , k , α and v_c are fixed quantities. The maximum value of m_L/m_i is obtained when the following relation is fulfilled

$$\left(\frac{v_c}{\Delta v} \right)^2 = 2 \left(\frac{c}{\Delta v} \right)^2 \left(e^{\Delta v/c} - 1 - \frac{\Delta v}{2c} \right) \quad [22]$$

Note that $(\Delta v/c)$ is in implicit function of $(v_c/\Delta v)$ only. Solving Equation [22] for $(\Delta v/c)$, and inserting it in Equation [21] leads to an expression for the payload weight ratio which is only a function of $(v_c/\Delta v)$ and k . Fig. 10 shows a plot of the maximum payload weight vs. $(\Delta v/v_c)$; k was fixed at 0 and 0.1. Equation [20] is used for the constant acceleration case, and Equations [21 and 22] combined for the case of constant exhaust velocity. It should be noted that the curves practically overlap when (m_L/m_i) is greater than 0.2. Thus for practical flight problems there is no essential advantage of the constant acceleration over the constant thrust flight plan; in fact, operation of thrust devices over too wide a specific impulse range may require inefficient operation.

For the case of constant exhaust velocity the maximum payload can be expressed in terms of k and $\Delta v/c$ by substituting for v_c from Equation [22] into Equation [21]

$$\frac{m_L}{m_i} = 1 - \frac{(1+k)(1 - e^{-\Delta v/c})^2}{1 - [1 + (\Delta v/2c)]e^{-\Delta v/c}} \quad [23]$$

Equation [23] is plotted in Fig. 11. It is not possible to obtain a flight plan that could be represented by a point in the region to the left of these curves. Thus, such curves can be used to determine the optimum exhaust velocity c for each mission; i.e., for a given velocity increment Δv and desired payload weight ratio.

Comparison of Flight Time and Payload

The framework necessary for comparing the performance of electrical propulsion systems with and without electrical storage has thus been prepared. We will use two of the several ways in which this comparison can be made: 1 The

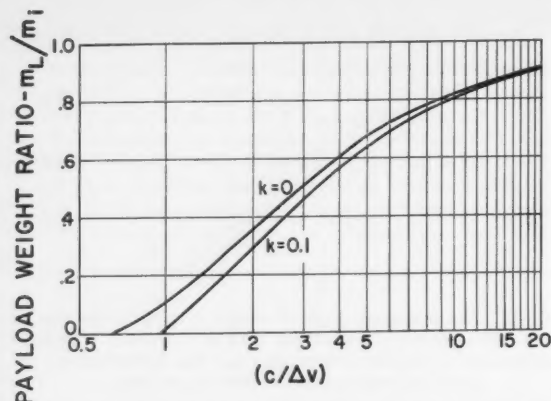


Fig. 11 The maximum payload weight ratio plot as a function of $(c/\Delta v)$ for constant exhaust velocity c . Δv is the velocity increment that the thrust acceleration must supply for the mission. The structure factor k was fixed at 0 and 0.1

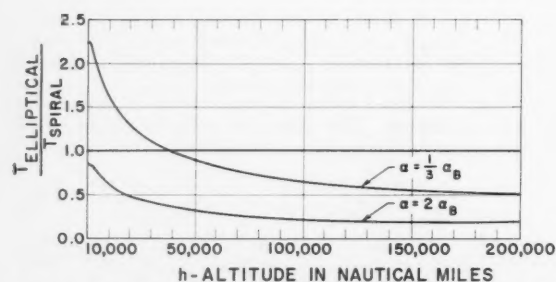


Fig. 12 The ratio of the flight times for the same payload weight ratio as a function h for a trip from 100-mile altitude to a circular orbit at h and return to Earth. α and α_B are the specific weight of the propulsion system and the storage batteries

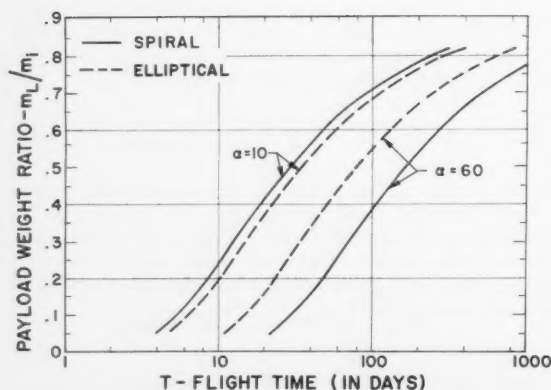


Fig. 13 The payload weight ratio as a function of flight time for a round trip from 100 miles altitude to the 24-hr orbit (22,000 miles altitude). Two values for the propulsion system specific weight are shown: $\alpha = 10$ lb/kw and $\alpha = 60$ lb/kw. The battery specific weight $\alpha_B = 30$ lb/kw

flight times are compared for a fixed payload weight ratio; 2 the payload weight ratio is compared for the same flight times.

In the previous section it was shown that the payload weight ratio is only a function of $(\Delta v/v_c)$ and k . Thus, for a fixed payload weight ratio m_L/m_i and structure factor k , $(\Delta v/v_c)$ is constant independent of the flight plan. This important result states that the flight time T is given by the relation

$$T = \frac{\alpha(\Delta v)^2}{2(1+k)} \quad [24]$$

for all flight plans. Thus, the ratio of the elliptical and spiral orbit flight times is

$$\frac{T_{\text{elliptical}}}{T_{\text{spiral}}} = \frac{(\alpha_{\text{elliptical}})(\Delta v_{\text{elliptical}})^2}{(\alpha_{\text{spiral}})(\Delta v_{\text{spiral}})^2} \quad [25]$$

The structure factor is assumed to be the same for both cases. The Δv required for a round trip mission to a circular orbit and return to Earth is shown in Fig. 7. $\Delta v_{\text{elliptical}} = (\Delta v_p + 2\Delta v_a)$ and $\Delta v_{\text{spiral}} = 2\Delta v_a$. For the elliptical orbit, the extra weight of the batteries, say m_B , must be added. The weight of the whole propulsion system becomes $m_p + m_B$. The corresponding specific weight $\alpha_{\text{elliptical}} = (m_p/P) + m_B/P = \alpha + \alpha_B$ where α_B is the specific weight of the batteries alone. For the spiral orbit case there is no storage so $\alpha_{\text{spiral}} = \alpha$ assuming the same propulsion system in both cases. Substituting these values for Δv and α in Equation [24]

$$\frac{T_{\text{elliptical}}}{T_{\text{spiral}}} = \frac{\alpha + \alpha_B}{\alpha} \left(\frac{\Delta v_p + 2\Delta v_a}{2\Delta v_a} \right)^2 \quad [26]$$

The specific weight of the batteries α_B for a practical design is estimated to be from 20 to 40 lb/kw depending on the mission. The power supply specific weight will vary between 10 and 60 lb/kw depending on the size of the power supply. Thus the ratio (α_B/α) will range from 0.5 to 3. In Fig. 12 is shown the variation of the flight time ratio given by Equation [26] for round trip missions from a 100-mile circular orbit to larger circular orbits. The curves are for (α_B/α) equal to 3 and 0.5. Note that when $\alpha_B/\alpha = 0.5$, corresponding to $\alpha \approx 60$ lb/kw, the flight time is always less for the elliptical orbits. For $\alpha_B/\alpha = 3$ ($\alpha \approx 10$ lb/kw), elliptical orbits become more favorable only above 40,000 miles altitude.

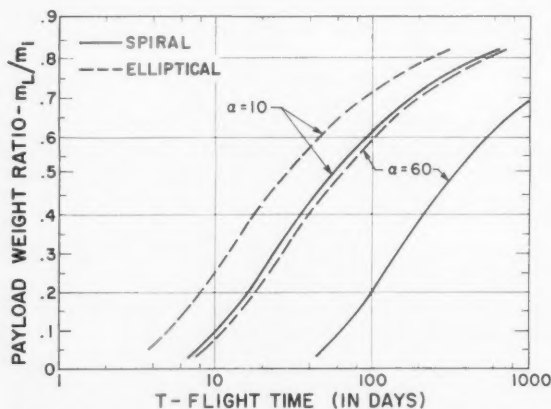


Fig. 14 The payload weight ratio as a function of flight time for a round trip from 100 miles altitude to a lunar orbit. Two values for the propulsion system specific weight are shown: $\alpha = 10$ lb/kw and $\alpha = 60$ lb/kw. The battery specific weight $\alpha_B = 30$ lb/kw

The payload weight ratio as a function of the flight time is shown in Figs. 13 and 14 for two missions: A round trip from a 100-mile circular orbit to the 24-hr orbit (22,000 miles altitude) and lunar orbit. The curves were obtained with the use of Equation [20]. The (Δv) 's are for the spiral and elliptical flight plan from Fig. 7. Note that the payload weight can always be exchanged for flight time.

Limitations on This Simplified Analysis

The analysis presented above to evaluate the usefulness of electrical storage was simplified considerably. The justification was that simple analytical results could be obtained which are in fair agreement with the practical flight situation. However, this analysis for the spiral orbit flight plan becomes very poor when the local gravitational force is equal to or less than the thrust force; the flight changes from a spiral to a straight line (7,8). This occurs at an altitude of approximately 80,000 miles for a thrust acceleration of $10^{-3} g_0$ and at the altitude of the lunar orbit $10^{-4} g_0$. However, even for a $10^{-3} g_0$ acceleration, the Δv required to a lunar orbit is still the Δv shown in Fig. 4, because the change from tightly wound spiral orbit is compensated by the extra thrust required to return to a circular orbit. This compensation does not hold for the return trip, and for $10^{-3} g_0$ the Δv requirement becomes less than the Δv of Fig. 4 for altitudes above 100,000 miles. For $10^{-3} g_0$ our analysis cannot be used for altitudes above about 200,000 miles.

In a practical situation the battery storage capacity is limited, and it is not possible to achieve the ideal flight plan with impulses at perigee and apogee, as shown in Fig. 6. The thrust requirements and the flight time will thus be larger than that given in our simplified analysis. It was shown that in a practical situation about 10 per cent more flight time is needed for trips to a lunar orbit. This would be less for low altitude orbits. On the other hand, the spiral orbit flight times are over a factor of 2 longer than the ideal elliptical case. Thus, our analysis is a valid approximation.

Summary

The usefulness of electrical energy storage for effecting a transfer between two circular orbits has been evaluated. The battery weight penalty required for the electric storage is compensated by the smaller thrust requirements of the elliptical flight plan. In evaluating a particular mission an important parameter is the relative weights of the batteries and the rest of the propulsion system. For batteries that are presently available the electrical storage becomes practical for some missions when the specific weight of the electrical propulsion system is greater than 20 lb/kw. Another advantage of the use of the elliptical orbit flight plan is available for the initial portion of the trip where the perigee altitude remains low. If, for some reason, it becomes necessary to interrupt the trip, a return to a lower orbit or to the Earth can be accomplished quickly. An impulse is made near apogee which lowers the perigee altitude into the atmosphere. The orbit can be circularized quickly with the use of a suitable atmospheric drag system.

Interception and Rendezvous Problems

In this section we will consider missions between orbits in which the total energy of the vehicle does not change appreciably, that is, transfers between orbits at essentially the same altitude above the Earth. These flight plans arise in interception and rendezvous missions. It is convenient to consider separately the motion along three coordinates: 1 A transfer between two orbits that are in the same plane, 2 a mission requiring a change in latitude i of the orbit plane, and 3 a change in the angle Ω , i.e., a rotation of the line of nodes of the orbit plane.

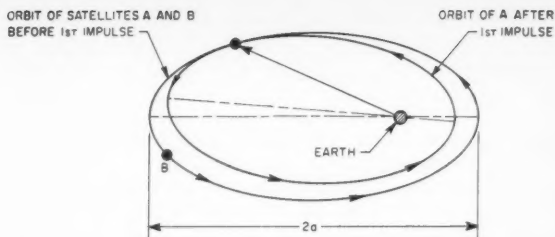


Fig. 15 The flight plan to make a rendezvous between two satellites A and B that are moving on the same orbit but at different positions

Transfer Between Co-Planar Orbits

The problem of determining the best flight plan for making a rendezvous (or a transfer) between two arbitrary orbits at essentially the same altitude is more involved than the Hohmann problem of transfer between two circular orbits. We have only considered the simpler problems of: 1 A rendezvous between two vehicles moving along the same elliptical orbit but at different points on the ellipse; 2 a transfer from a circle to an ellipse. The more general problem of transferring between two arbitrary ellipses has been considered by Lawden (5).

Fig. 15 shows the flight plan for the rendezvous between two vehicles A and B that are in the same elliptical orbit but separate by a fraction N of the orbit period. Suppose that vehicle A can maneuver and wants to make contact with vehicle B. This can be accomplished with two impulses. The first impulse is applied tangentially to the orbit with the exhaust thrust pointed in the direction of B, resulting in a reduction in the flight energy of A. The orbit of A now changes to a smaller ellipse remaining tangent to the original ellipse at the point of impulse, at A. The period of revolution τ for the resulting elliptical orbit is smaller than the original period. Thus, as time progresses for each revolution of satellite A, B will come closer to the tangent position of A. If the change in period $\Delta\tau$, of satellite A, is $1/n$ (where n is an integer) of the original separation time τN , then after n revolutions of A, satellite B will recede to the tangent position of A. When A and B become coincident, then A makes a reverse impulse which gives it the same velocity as A and the rendezvous is completed.

We will now calculate the propellant requirement for such a mission. The velocity of the vehicle at point A is

$$v_A^2 = 2g_0 R_E^2 \left[\frac{1}{R_A} - \frac{1}{2a} \right] \quad [27]$$

where a is the semimajor axis. When an impulse producing the velocity change Δv is applied at A, the semimajor axis changes by Δa , but R_A remains constant. The relation between Δv and Δa is

$$v_A \Delta v = \frac{g_0 R_E^2}{2a^3} \Delta a \quad [28]$$

From Equation [3] the period for the initial orbit is

$$\tau = \frac{2\pi}{\sqrt{g_0 R_E^2}} a^{3/2} \quad [29]$$

After the impulse, the change in period becomes

$$\frac{\Delta\tau}{\tau} = \frac{3}{2} \frac{\Delta a}{a} \quad [30]$$

Inserting Equation [30] into Equation [28] yields

$$v_A \Delta v = \frac{g_0 R_E^2}{3a} \frac{\Delta \tau}{\tau} \quad [31]$$

If the satellites become coincident after n orbit revolutions, the time T necessary for the mission is $T = n(\tau - \Delta \tau)$, and the required period change $\Delta \tau$ is $\Delta \tau = N\tau/n$, where N is the fraction of the period that the satellites are initially separated. Equation [31] becomes

$$\Delta v = \frac{g_0 R_E^2}{3v_A a} \frac{\tau - \Delta \tau}{NT} \quad [32]$$

The total impulse for the mission will be twice the one given by this equation, since a similar impulse has to be applied to return satellite A to its original orbit. It should be noted that the range of T in Equation [32] is not continuous, but can only be integral multiples of the period $(\tau - \Delta \tau)$. The

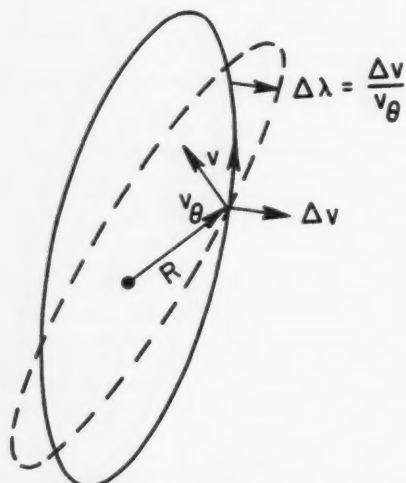


Fig. 16 Rotation of the orbit plane by an impulse Δv applied normal to the plane

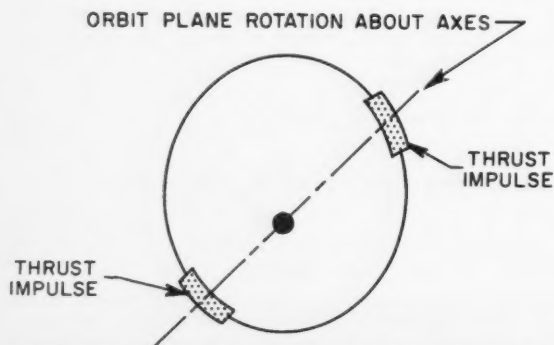


Fig. 17 Thrust program when using electrical energy storage for rotation of the orbit

Δv requirements can be very small by making $\Delta \tau$ small and waiting a long time. This very small Δv is possible because initially the satellites are in the same orbit.

Equation [32] indicates that for a given ellipse the impulse requirement is minimized when v_A is a maximum, since all other quantities remain unchanged. This indicates that satellite A should wait until the perigee is reached and then apply the impulse. This is the most efficient way of applying thrust.

When using electrical propulsion without energy storage it is possible to accomplish the rendezvous if satellite A uses a constant retarding thrust for half the flight time and accelerating thrust the latter half. If the acceleration is small, the orbit will spiral in and then out although the orbit at any time will have the shape of the original ellipse. For this spiral orbit case the analysis has been made only for an initially circular orbit and the necessary impulse is twice that required for the previous case using two short impulses.

Transfer Between Circular and Elliptical Orbits

The more complicated problem of making a rendezvous between a circle and an ellipse can, in general, be separated into parts that have already been treated: 1 Making the first impulse of the Hohmann transfer ellipse; 2 the shifting of angular position along an orbit. This is not the only possible flight plan and there was no attempt to determine the optimum thrust plan.

The use of electric storage has a very large advantage for missions requiring a transfer from a circular to an elliptical orbit. Since impulses are required at only limited portions of the orbit, the flight time would be reduced with the use of storage. Flight plans as described in Figs. 6 and 8 would be used.

Missions Requiring a Rotation of the Orbit Plane

In order to rotate the orbit plane thrust must be applied perpendicular to the orbit plane. An instantaneous velocity increment Δv applied to the satellite normal to the plane of the orbit will rotate the orbit plane about the radius vector to that point of an angle $\Delta \lambda$ where

$$\Delta \lambda = \frac{\Delta v}{v_\theta} = \frac{R}{\sqrt{g_0 R_E^2 a (1 - e^2)}} \Delta v \quad [33]$$

v_θ is the azimuthal component of the satellite velocity. The relation on the right side expresses v_θ in terms of the usual orbit variables. This rotation is indicated in Fig. 16. An impulse applied at another point will cause a rotation about that point.

A small angular rotation $\Delta \lambda$ can be resolved into rotations about the coordinates Ω and i , where Ω is the angle between the vernal equinox and the line of nodes in the equatorial plane, and i is the inclination of the orbit with respect to the Equator

$$\Delta \lambda = \Delta \Omega + \Delta i \quad [34]$$

where

$$\Delta \Omega = \Delta \lambda \frac{\sin u}{\sin i} = \frac{R \sin u}{\sqrt{g_0 R_E^2 a (1 - e^2)} \sin i} \Delta v \quad [35]$$

$$\Delta i = \Delta \lambda \cos u = \frac{R \cos u}{\sqrt{g_0 R_E^2 a (1 - e^2)}} \Delta v \quad [36]$$

The angle between the radius vector to the satellite and the line of nodes in the equatorial plane is designated by u . To produce the largest change in latitude angle i , without any change in Ω , the impulse Δv should be applied when passing through the equatorial plane, i.e., for $u = 0$ and 180 deg. On the other hand, an impulse applied when $u = \pm 90$ deg would produce the largest change in Ω with no change in i .

The best control when changing the direction of the orbit plane is accomplished with short impulses at desired points in the orbit. Such maneuvers which require pulsing are more suited to electrical propulsion having electric storage, since this permits the complete utilization of the available energy. The flight plan is shown in Fig. 17. The batteries would be charged during the free flight periods and discharged, producing relatively large impulses, at the desired points along the orbit. Since the thrust pulses can be used with equal efficiency on opposite sites of the orbit, the storage capacity need be only about $\frac{1}{4}$ of the period. This would correspond to less than a $\frac{1}{2}$ -hr storage capacity for low altitude orbits. Thus, the required specific weight of the batteries would be in the range from 10 to 15 lb/kw. It can be shown that there is an advantage to the use of battery storage, even with this weight penalty, when the specific weight of the propulsion system (excluding the batteries) is greater than 15 lb/kw. The flight time and propellant requirements would be less.

Summary

We have compared the performance of electrical propulsion systems with and without energy storage for several missions in the gravitational field of the Earth. The advantage of electric storage depends upon the relative weights of the electrical propulsion system and of the batteries, and upon the relative decrease in the impulse requirement for the elliptical

orbit compared to the spiral orbit flight plans.

Energy storage is advantageous for rendezvous maneuvers at low altitudes. For most low altitude missions (for example, transfers from circular to elliptical orbits, or between orbits that are not in the same plane), optimum operation is achieved when impulses are applied only over limited portions of the orbit. The use of energy storage in low thrust propulsion systems permits the application of short impulses while still utilizing all available energy. This decreases the flight time for the maneuver, and considerably simplifies the guidance and control problem.

References

- 1 Irving, J. H. and Blum, E. K., "Comparative Performance of Ballistic and Low-Thrust Vehicles for Flight to Mars," Second Annual AFOSR Astronautics Symposium, Denver, Colo., April 1958.
- 2 Hohmann, W., "Die Erreichbarkeit der Himmelskörper," R. Oldenbourg, Munich, 1925.
- 3 Ehricke, K. A., "Comparisons of Propulsion Systems: Solar Heating, Arc-thermodynamics and Arc-magnetohydrodynamic," Paper in Advanced Propulsion Systems Symposium, Dec. 11-13, 1957.
- 4 Stuhlinger, E., "Electrical Propulsion System for Space Ships with Nuclear Power Source," Parts I, II and III, *J. Astronaut.*, Winter 1955, Spring 1956 and Summer 1956.
- 5 Lawden, D. F., "Minimal Rocket Trajectories," *JOURNAL OF THE AMERICAN ROCKET SOCIETY*, Nov.-Dec. 1953, vol. 23, p. 360.
- 6 Moulton, F. R., "An Introduction to Celestial Mechanics," 2nd ed., Macmillan Co., New York, 1914.
- 7 Perkins, F. J., "Flight Mechanics of Low Thrust Spacecraft," Second Annual AFOSR Astronautics Symposium, Denver, Colo., April 1958.
- 8 Tsien, H. S., "Take-off from Satellite Orbit," *JOURNAL OF THE AMERICAN ROCKET SOCIETY*, July-Aug. 1953, vol. 23, p. 233.

Technical Notes

Composition of Reaction Mixture Flowing Through Rocket Nozzle

R. P. RASTOGI¹

Panjab University, Hoshiarpur, India

and

T. P. PANDYA²

Lucknow University, Lucknow, India

A simple procedure is developed which permits the prediction of near-frozen or near-equilibrium flow in rocket nozzles. It is found that the reaction $2\text{NO} \rightleftharpoons \text{N}_2 + \text{O}_2$ in aniline-nitric acid rocket motors is nearly frozen at the chamber exit, in agreement with the earlier finding of Penner. The recent data on the supersonic flow of N_2O_4 in de Laval nozzles are examined. The predicted composition agrees satisfactorily with the experimental value at the nozzle exit.

Received March 18, 1959.

¹ Chemistry Department.

² Physics Department.

CONSIDER the reaction $A \rightarrow B$, the kinetics of which is governed by the equation

$$dx/dt = k(a - x)$$

where

k = rate constant

a = initial composition

x = amount of A decomposed

The rate constant is related to temperature by the relation

$$k = C \cdot e^{-E/RT}$$

where

E = energy of activation

T = temperature

C = certain constant

R = gas constant

The above equation can be integrated under isothermal conditions, and the composition of A can be predicted at any instant provided the rate constant is known. However, in practice, we come across situations where the temperature varies with time, and hence the above equation cannot be

EDITOR'S NOTE: The Technical Notes and Technical Comments sections of ARS JOURNAL are open to short manuscripts describing new developments or offering comments on papers previously published. Such manuscripts are usually published without editorial review within a few months of the date of receipt. Requirements as to style are the same as for regular contributions (see masthead page).

integrated. Problems of this nature are encountered while estimating the composition of the reaction mixture across the rocket nozzle where the temperature suffers a sharp drop of several thousand degrees. The estimation of composition is essential for computing the correct exhaust velocity of rockets, since the velocity v at the nozzle exit is given by

$$(1/2)Mv^2 = H_c - H_e \quad [1]$$

where

M = mass

H = enthalpy of the fluid mixture at constant pressure when one-dimensional adiabatic flow is assumed

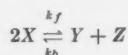
The subscripts c and e denote chamber and nozzle exit, respectively.

The composition of the reaction mixture at the exit is usually determined by assuming the freezing of chemical reaction at the chamber exit or by assuming the establishment of immediate chemical equilibrium at the nozzle exit (1).³ For this purpose, useful criteria have been developed by Penner, but the greatest disadvantage is that in actual application the frozen flow criterion and equilibrium flow criterion have to be applied separately.

The aim of the present paper is to evolve a more straightforward procedure for deciding the nature of the flow in conventional rockets.

Near-Equilibrium and Frozen Flow in Rocket Nozzles

We shall consider, for the sake of simplicity, reactions of the type



k_f is the rate of forward reaction, and k_b is the rate of back reaction. Reactions of the above type occur in aniline-nitric acid and hydrogen-fluorine rocket motors. We assume that at the chamber exit the number of molecules of the species X , Y and Z are a , b and c , respectively. If V is the volume and x is the number of molecules of species X decomposed, the rate of reaction is given by

$$V \cdot \left(\frac{dx}{dt} \right) = k_f \cdot (a - x)^2 - k_b \left(b + \frac{x}{2} \right) \left(c + \frac{x}{2} \right) \quad [2]$$

Since k_f and k_b vary with temperature, the above equation cannot be integrated. However, some approximate conclusions can be reached if it is assumed that the cooling rate is constant. Before doing that we shall discuss the general case.

Since x is a function of temperature T , time t and pressure P , we can write by the methods of partial differentiation

$$\frac{dx}{dt} = \left(\frac{\partial x}{\partial t} \right)_{T,P} + \left[\left(\frac{\partial x}{\partial T} \right)_{t,P} + \left(\frac{\partial x}{\partial P} \right)_{t,t} \cdot \frac{dP}{dt} \right] \cdot \frac{dT}{dt} \quad [3]$$

Here $(-dT/dt)$ is the cooling rate which would depend on the dimensions of the nozzle. It can be seen that the net reaction rate can be determined if the quantities on the right-hand side of Equation [3] can be evaluated. This is done below.

At equilibrium

$$\frac{k_f}{k_b} = \frac{(b + x_e/2)(c + x_e/2)}{(a - x_e)^2} \quad [4]$$

where x_e is the equilibrium value of x . Using this relation we can write Equation [2] in the following form

$$V \cdot \frac{dx}{dt} = \frac{k_f \cdot (x_e - x)}{(b + x_e/2)(c + x_e/2)} \times \left[\frac{a^2(b + c) + 4abc}{2} + \frac{a^2 - 4bc}{4} (x_e + x) - \frac{x \cdot x_e}{2} (a + b + c) \right] \quad [5]$$

³ Numbers in parentheses indicate References at end of paper.

On integration, at constant temperature and pressure, this equation yields

$$\frac{1}{V} \cdot \frac{k_f t}{4(b + x_e/2)(c + x_e/2)} = \frac{1}{A + Bx_e} \ln \frac{A + Bx_e}{x_e - x} + \text{constant} \quad [6]$$

where

$$A = 2a^2(b + c) + 8abc + (a^2 - 4bc)x_e$$

$$B = (a^2 - 4bc) - 2x_e(a + b + c)$$

When $t = 0$, $x = 0$, and hence Equation [6] reduces to

$$\frac{1}{V} \cdot \frac{k_f t}{4(b + x_e/2)(c + x_e/2)} = \frac{1}{A + Bx_e} \ln \frac{(A + Bx_e)x_e}{A(x_e - x)} \quad [7]$$

from which we obtain

$$x = \frac{Ax_e(e^{Lt} - 1)}{Ae^{Lt} + Bx_e} \quad [8]$$

where

$$L = \frac{k_f \cdot (A + Bx_e)}{4(b + x_e/2)(c + x_e/2)} \cdot \frac{1}{V}$$

Differentiating both the right and left sides of Equation [8] with respect to T , keeping time and pressure constant, and eliminating t with the help of Equation [7] we have (2)

$$\left(\frac{dx}{dT} \right)_{t,P} = \left(B \cdot \frac{dA}{dT} - A \cdot \frac{dB}{dT} \right) \cdot \frac{x(x_e - x)}{A(A + Bx_e)} + \frac{x(A + Bx_e)}{x_e(A + Bx_e)} \cdot \frac{dx_e}{dT} + \frac{(A + Bx_e)(x_e - x)}{(A + Bx_e)^2} \times \frac{dL}{dT} \ln \frac{(A + Bx_e)x_e}{A(x_e - x)} \quad [9]$$

Using the relation

$$\frac{d \ln k}{dT} = \frac{\Delta H}{RT^2}$$

we have

$$\left(\frac{dx_e}{dT} \right)_{t,P} = \frac{2(a - x_e)(b + x_e/2)(c + x_e/2)}{x_e(a + b + c) + (ab + ac + 4bc)} \cdot \frac{\Delta H}{RT^2} \quad [10]$$

where

ΔH = heat of reaction

K = equilibrium constant

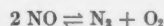
From Equations [9] and [10], the value of $(dx/dT)_{t,P}$ can be readily evaluated. In a similar way, one can evaluate $(dx/dP)_{t,P}$, and hence the net reaction rate can be computed.

We can learn whether near-equilibrium or frozen flow is maintained by using the condition $dx/dt = 0$ at the exit, which would be true for both the cases. Thus, for both cases, we shall have

$$\left(\frac{dx}{dt} \right)_{T,P} + \left[\left(\frac{dx}{dP} \right)_{t,P} \cdot \frac{dP}{dT} + \left(\frac{dx}{dT} \right)_{t,P} \right] \cdot \frac{dT}{dt} = 0 \quad [11]$$

The resulting equation obtained after proper substitution can be solved for x . If x is found to be zero, freezing of chemical reaction would take place. On the other hand, when x is equal to the equilibrium value, one can safely conclude that near-equilibrium flow occurs.

As an illustration, we take the case of aniline-nitric acid rocket motor where the basic reaction involved is



For the sake of simplicity, we shall neglect the intermediate

(Continued on page 113)

